

**SEARCHING FOR MULTIPLE POPULATIONS IN  
MASSIVE YOUNG AND INTERMEDIATE AGE  
CLUSTERS**

**Silvia Martocchia**

A thesis submitted in partial fulfilment of the requirements of  
Liverpool John Moores University  
for the degree of  
Doctor of Philosophy.

June 25, 2020

## Abstract

Among the many mysteries of our Universe, one still unanswered question is how globular clusters form. Globular clusters are very dense agglomerates of hundreds of thousands of stars and they host some of the oldest known stars in our Universe. Since they are luminous, old and found in all massive galaxies, they are a fundamental piece of the puzzle to understand galaxy formation and evolution processes.

Traditionally, globular clusters were thought to be simple stellar systems, in which all stars were born at the same time and have the same chemical composition. However, in the last few decades, it has been shown that stars within a given globular cluster display inhomogeneities in their chemistry. Every massive old globular cluster located in the Milky Way, for which high precision and deep observations were obtained, was found to host several different stellar populations, i.e. multiple populations. Each stellar population is characterized by specific chemical patterns observed in the atmospheres of individual stars. Knowing how such multiple populations form and how they impact the evolution of globular clusters is crucial to understand the formation of stars and clusters themselves and, more broadly, the formation and evolution of galaxies.

Many theoretical scenarios have been proposed to explain the origin of the chemical anomalies in globular clusters. Most models treat the origin of this phenomenon as multiple events of star formation. In such models, a first generation of stars forms from the collapse of a giant molecular cloud which is homogeneous in its chemical composition. The winds of the massive stars from this first generation sink in the centre of the cluster to collapse and provide material for a second generation of stars, which then forms with a different chemical composition. While theoretically straightforward, such scenarios (which involve many types of massive stars) fail in reproducing many of the observed properties of multiple populations in globular clusters. Hence, the formation mechanism for the origin of multiple populations remains an open question.

Most studies of multiple populations focused only on ancient globular clusters, aged up to  $\sim$ 13 Gyr. However, many dense and massive younger star clusters are observed in nearby galaxies. Is the multiple populations phenomenon limited to the ancient globular clusters, i.e. could this be a cosmological effect?

The goal of this thesis has been expanding the search for multiple populations to star clusters that are significantly younger than the old globular clusters, i.e. up to 10 times younger. The first major result presented in this work is that multiple populations are found also in the young clusters, down to  $\sim$ 2 Gyr old objects, showing that the phenomenon of multiple populations is not only restricted to the early Universe.

Another interesting result I report is that the extent of the multiple populations (in chemical abundance spread) is a strong function of age, with older clusters having larger chemical variations. Additionally, I show that there is no difference in age between the populations in a young star cluster. Such results represent fundamental constraints for the origin of multiple populations and might point towards a new and fresh direction into the onset of this complex phenomenon.

An important and related question is whether the young massive star clusters are the same type of stellar systems as the ancient globular clusters, just observed at a different stage of their lifetimes. If confirmed, this could provide important constraints on star cluster formation studies. Therefore, in this thesis I explored clusters at younger ages in order to address the fundamental question whether the star (and cluster) formation conditions were different in the early Universe.

The results presented here represent an important hint that ancient and young clusters share the same origin and are only separated in age. I show that star clusters do not require special conditions in which to form, so that they can be used as tracers for the formation and evolution of galaxies.

# Publications

Within this thesis, the work within Chapters has been presented in the following jointly authored publications:

- (2020) - **Martocchia, S.**, Dalessandro, E., Salaris, M., Larsen, S., Rejkuba, M., 2020. *Is Fornax 4 the nuclear star cluster of the Fornax dwarf spheroidal galaxy?*. MNRAS, 495, 4518M (link: [ads](#))
- (2019) - **Martocchia, S.**, Dalessandro, E., Lardo, C., Cabrera-Ziri, I., Bastian, N., Kozhurina-Platais, V., Salaris, M., Chantereau, W., Geisler, D., Hilker, M., et al. , 2019, *The search for multiple populations in Magellanic Clouds clusters - V. Correlation between cluster age and abundance spreads.* MNRAS, 487, 5324-5334 (link: [ads](#))
- (2018) - **Martocchia, S.**, Niederhofer, F., Dalessandro, E., Bastian, N., Kacharov, N., Usher, C., Cabrera-Ziri, I., Lardo, C., Cassisi, S., Geisler, D., et al. , 2018, *The search for multiple populations in Magellanic Cloud clusters - IV. Coeval multiple stellar populations in the young star cluster NGC 1978*, MNRAS, 477, 4696-4705. (link: [ads](#))
- (2018) - **Martocchia, S.**, Cabrera-Ziri, I., Lardo, C., Dalessandro, E., Bastian, N., Kozhurina-Platais, V., Usher, C., Niederhofer, F., Cordero, M., Geisler, D., et al., 2018, *Age as a major factor in the onset of multiple populations in stellar clusters*, MNRAS, 473, 2688-2700. (link: [ads](#))
- (2017) - **Martocchia, S.**, Bastian, N., Usher, C., Kozhurina-Platais, V., Niederhofer, F., Cabrera-Ziri, I., Dalessandro, E., Hollyhead, K., Kacharov, N., Lardo,

C., et al., 2017, *The search for multiple populations in Magellanic Cloud Clusters - III. No evidence for multiple populations in the SMC cluster NGC 419*, MNRAS, 468, 3150-3158 (link: [ads](#))

Whilst writing this thesis, S. Martocchia has also contributed to the following publications, which are focused on topics correlated to the thesis work:

- (2020) - Bastian, N., Lardo, C., Usher, C., Kamann, S., Larsen, S. S., Cabrera-Ziri, I., Chantereau, W., **Martocchia, S.**, et al. 2020. *Searching for Multiple Populations in the Integrated Light of the Young and Extremely Massive Clusters in the Merger Remnant NGC 7252*, MNRAS in press. (link: [ads](#))
- (2020) - Saracino, S., **Martocchia, S.**, Bastian, N., et al. 2020. *Chromosome maps of young LMC clusters: An additional case of coeval multiple populations*, MNRAS in press. (link: [ads](#))
- (2020) - Salaris, M.; Usher, C.; **Martocchia, S.**; Dalessandro, E.; Bastian, N.; Saracino, S.; Cassisi, S.; Cabrera-Ziri, I.; Lardo, C. *Photometric characterization of multiple populations in star clusters: the impact of the first dredge-up*. MNRAS, 492, 3459S. (link: [ads](#))
- (2020) - Dagleish, H.; Kamann, S.; Usher, C.; Baumgardt, H.; Bastian, N.; Veitch-Michaelis, J.; Bellini, A.; **Martocchia, S.**; Da Costa, G. S.; Mackey, D.; Bellstedt, S.; Pastorello, N.; Cerulo, P. *The WAGGS project - III. Discrepant mass-to-light ratios of Galactic globular clusters at high metallicity*, MNRAS in press. (link: [ads](#))
- (2020) - Kamann, S.; Bastian, N.; Gossage, S.; Baade, D.; Cabrera-Ziri, I.; Da Costa, G.; de Mink, S. E.; Georgy, C.; Giesers, B.; Gttgens, F.; Hilker, M.; Husser, T. -O.; Lardo, C.; Larsen, S. S.; Mackey, D.; **Martocchia, S.**; Mucciarelli, A.; Platais, I.; Roth, M. M.; Salaris, M. *How stellar rotation shapes the colour-magnitude diagram of the massive intermediate-age star cluster NGC 1846*. MNRAS, 492, 2177. ([ads](#))

- (2019) - Dalessandro E., Cadelano M., Vesperini E., **Martocchia S.**, Ferraro F., Lanzoni B., Bastian N., Hong J., Sanna N. *A Family picture: tracing the dynamical path of the structural properties of multiple populations in globular clusters*, ApJ, 884L, 24D. (link: [ads](#))
- (2019) - Bastian, N., Usher, C., Kamann, S., Lardo, C., Larsen, S. S., Cabrera-Ziri, I., Chantereau, W., **Martocchia, S.**, Salaris, M., Schiavon, R. P., et al. , 2019, *Multiple populations in integrated light spectroscopy of intermediate-age clusters*, MNRAS, 489, L80-L85. (link: [ads](#))
- (2019) - Chantereau, W., Salaris, M., Bastian, N., & **Martocchia, S.** , 2019, *Helium enrichment in intermediate-age Magellanic Clouds clusters: towards an ubiquity of multiple stellar populations?*, MNRAS, 484, 5236-5244. (link: [ads](#))
- (2019) - Hollyhead, K., **Martocchia, S.**, Lardo, C., Bastian, N., Kacharov, N., Niederhofer, F., Cabrera-Ziri, I., Dalessandro, E., Mucciarelli, A., Salaris, M., et al. , 2019, *Spectroscopic detection of multiple populations in the  $\sim 2$  Gyr old cluster Hodge 6 in the LMC*. MNRAS, 484, 4718-4725 (link: [ads](#))
- (2018) - Kamann, S., Bastian, N., Husser, T.-O., **Martocchia, S.**, Usher, C., den Brok, M., Dreizler, S., Kelz, A., Krajnović, D., Richard, J., et al. , 2018, *Cluster kinematics and stellar rotation in NGC 419 with MUSE and adaptive optics*. MNRAS, 480, 1689-1695 (link: [ads](#))

And the following conference proceedings:

- (2019) - **Martocchia S.**, *The role of cluster age on the onset of multiple populations in stellar clusters*, arXiv:1907.12440 to appear in Proceedings IAU Symposium n. 351, "Star Clusters: From the Milky Way to the Early Universe", 2019. (link: [ads](#))
- (2017) - I. Cabrera-Ziri, **S. Martocchia**, K. Hollyhead, N. Bastian, *Interpreting the complex CMDs of the Magellanic Clouds clusters*. Mem. S.A.It. 2018, 89, 24C. (link: [ads](#))

# Acknowledgements

A huge thanks to all the people that stood beside me during this time of my life. The PhD was an incredible journey, that made me grow and learn so much. I truly believe your help was fundamental to achieve this goal.

First of all, I would like to thank my supervisors, as they were always present and supportive. I thank Nate because he always pushed me and inspired me with motivation. The same applies to Maurizio. È stato un piacere discutere di “scienza” (e anche calcio, cinema, chi più ne ha più ne metta) ogni mattina a Liverpool. Daje!

Ringrazio tanto Emanuele, per la pazienza che ha avuto con me dopo le centinaia di domande di fotometria (e non solo). I would really like to thank Marina, for warmly welcoming me at ESO and making me feel part of a great community. Grazie per il tuo continuo supporto e la tua gentilezza. Vorrei anche ringraziare Carmela, per l’aiuto prezioso che mi hai dato all’inizio, sempre disponibile ad aiutarmi, durante tutto il dottorato. Soprattutto ricordo con piacere le belle serate passate a Sesto, insieme ad Ema e Maurizio, tra gossip e grappa barricata!

Thanks also to all the collaborators that showed me support, Sebastian, Chris, Ivan, Soeren, Nikolay, William, Joel, Alessio. I would like to specially thank Sara, anche se ci conosciamo da poco, sei sempre stata molto gentile con me e spero che riusciremo a frequentarci di più in futuro. Grazie anche a Giacomo per il supporto e la disponibilità.

I finally thank all of you for insightful discussions and precious advice that allowed me to never give up.

I thank Marie and Angela, for having a very constructive viva. Marie, you have always

been supportive with me, keep being so lovely.

I really thank you Kirsty for your kindness and for our amazing chats over coffees, that I miss so much. I also thank all the students from LJMU and remember our trips to the pub on Fridays with cheer. Special thanks to Jon, Hannah, Egidjus, Seb, Alberto, Maisie. I also thank Meghan, with which I started a new period of my life, when I moved to Garching, it was nice to support each other.

My second part of the PhD was spent in Garching, and I must admit it was not easy at all to change. But there I experienced the one I call the “Garching effect”. I met some fantastic people that supported me all the way through the end.

Vorrei ringraziarti tantissimo Taï, per la tua energia e la continua voglia di fare cose, che mi ha spinto a non abbandonare mai la motivazione. Grazie per il tuo supporto giornaliero, molto spesso a base di musica, pizza e cibo fatto in casa. Ora però tocca a me fare la pizza! Occhio a non perdere il primato a Garching ... ;) Alla mia sorella mancata Sara, grazie per la tua dolcezza, anche tu non hai mai smesso di motivarmi, grazie per la tua complicità e il supporto in ogni situazione...non ce l'avrei mai fatta senza i nostri spritz after-pale...and...thanks for all the fish! :)

Non ringrazierò mai abbastanza Carlo, per avermi fatto scoprire le bellezze delle montagne (eccetto quelle austriache) e per avermi dato l'affascinante opportunità di spingermi oltre i miei limiti, insieme con Tereza, who I also thank for our incredible chats in the office (sometimes we also used to talk about work). Really, thanks Tereza for your energy, and for being an amazing source of inspiration and motivation.

Grazie alle mie “stars”: Chiara, Giuls, non scorderò mai le risate (e pause) infinite nell’ufficio E.5.25! Grazie per il vostro grande supporto. Grazie ad Ele, la mia (quasi) coinquilina, è stato buffo ritrovarsi dopo anni in un altro istituto, grazie per le chiacchierate spesso davanti ad un tè caldo nei nostri mini-appartamenti. Grazie anche ad Edo per il supporto, la tua solarità sempre e comunque. E speriamo di poter ballare presto, poporopò! Thank you Jens for always being there, Stella’s pictures were so welcome, and sooner or later I will beat you at Splendor ;)

Efcharisto Tatiana! We just met lately, but you're always been so nice with me! and grazie for making me passionate about drawing again, sharing your great tips. I can't wait to spend more time together.

Thank you Aish for your sweetness! I really miss our chats in the office, can't wait to go back. I would also like to thank a lot: Pablo, Nelly, the super cute Gastón, keep always being so friendly and cheerful. Thanks Byron for your "Magic"-ness ;), and thank you Marco, Mayte, Alex, Laura and Stephen for always being so nice with me. Prashant, thanks for making me try some special food from India during the quarantine. Grazie a Serban! compagno di mille (dis)avventure all'SLC, è veramente divertente andare a scattare foto alla natura insieme, e parlare di fotografia. Kateryna, thank you so much for being so nice and to keep motivating me, I can't wait to spend more time together, possibly in a beer garden with the dirndl. I also thank Adriano, I'm sorry we did not play football in the end! It was fun to mess up the english phrasal verbs with you ;) Grazie a Claudia, sei stata una fantastica fellow mentor, ci sei sempre stata, grazie per i tuoi ottimi consigli di vita. Grazie anche ad Anna, sei una forza della natura. Thanks Avinash for being so nice with me from the very start, it was great to be officemates for some time.

I finally thank everyone at LJMU and ESO for being always kind with me and for the stimulating research environment where I always found inspiration. I also would like to thank any astronomer, admin officer, etc.. that helped me and showed support.

Un ringraziamento speciale ai miei amici romani! :) Ci siamo sparpagliati in giro per il mondo ma non per questo il nostro rapporto è cambiato. Non potrò mai ringraziare abbastanza le mie Silvie, il vostro supporto giornaliero, nonostante la distanza, siete sempre state qui con me. Grazie per la vostra dolcezza, per i nostri viaggi alla scoperta dell'Italia!

Grazie a Ciro e Fede; a Dinho e Manu, il vostro alpaca è sempre stato con me! È sempre fantastico tornare a Roma e incontrarci e chiacchierare al nostro Nino davanti ad un cornetto & cappuccino.

Grazie del supporto Fede e Franci, alle nostre chiacchieratone infinite su ogni divano

d'Europa ;) la vostra solarità mi ha sempre motivata. Ringrazio anche Alessandra per il tuo supporto, bellissime le nostre serate alla scoperta dei ristoranti a Muenchen, è stato bello vedersi spesso come un tempo e anche qui, chiacchiere infinite.

Un grazie speciale anche a Claudia e Alice e famiglia; grazie agli “astrofighi” e le nostre riunioni annuali a San Lorenzo, passate a condividere le tipiche lamentele da dottorandi ;)

Grazie a Francia perchè non ha mai smesso di esserci. Grazie anche ad Ilaria, Valentina, Ele ed Ele.

Un grande ringraziamento a Gabriele, per tutto quello che mi ha dato e per quello che abbiamo condiviso, e per essere cresciuti insieme in questi anni.

Ringrazio tantissimo la mia famiglia, gli zii Patrizia, Rosario, Gianfranco e Luciana e i miei cugini Alessia, Francesco e Andrea. Infine, ringrazio i miei Nonni, Mamma, Papà e Ludo, grazie per il vostro continuo incoraggiamento. Separarsi è stata la cosa più difficile, quindi vi ringrazio per aver compreso le mie scelte. Non avete mai smesso di supportarmi in ogni modo, grazie per la vostra dolcezza (ogni tanto ;)), per avermi portato in giro per il mondo e per tutto quello che abbiamo condiviso.

# Contents

<b>Contents</b>	<b>VIII</b>
<b>List of Tables</b>	<b>XI</b>
<b>List of Figures</b>	<b>XII</b>
<b>1 Introduction</b>	<b>2</b>
1.1 Globular clusters . . . . .	2
1.2 Young Massive Clusters . . . . .	4
1.3 Chemical abundance variations in GCs . . . . .	7
1.3.1 Multiple populations from photometry . . . . .	11
1.4 The main sequence and turnoff of YMCs . . . . .	14
1.5 Models for the origin of multiple populations . . . . .	17
1.6 What controls the origin of multiple populations? . . . . .	20
1.7 Summary . . . . .	23
<b>2 No evidence for multiple populations in the SMC cluster NGC 419</b>	<b>25</b>
2.1 The HST survey . . . . .	25

2.2	Observational techniques and models . . . . .	30
2.2.1	Observations and Data Reduction . . . . .	30
2.2.2	Field stars subtraction . . . . .	31
2.2.3	Differential reddening correction . . . . .	32
2.2.4	Models for the chemical anomalies . . . . .	32
2.3	Results . . . . .	35
2.3.1	Comparison with stellar models . . . . .	40
2.4	Discussion . . . . .	42
<b>3</b>	<b>Age as a major factor in the onset of multiple populations</b>	<b>46</b>
3.1	Analysis . . . . .	46
3.1.1	The CMD in UV colours . . . . .	48
3.1.2	The Red Giant Branch . . . . .	50
3.2	Results . . . . .	55
3.2.1	Comparison with stellar models . . . . .	60
3.3	Discussion . . . . .	63
<b>4</b>	<b>Coeval multiple stellar populations in the young star clusters NGC 1978</b>	<b>68</b>
4.1	Observations and Adopted isochrones . . . . .	69
4.1.1	Artificial stars test . . . . .	70
4.2	SGB stars selection . . . . .	72
4.3	SGB Analysis . . . . .	77
4.4	The Main Sequence Turnoff . . . . .	80

4.5	Discussion . . . . .	83
<b>5</b>	<b>Correlation between cluster age and abundance spreads</b>	<b>86</b>
5.1	Analysis . . . . .	87
5.1.1	Age Determination . . . . .	95
5.2	Results . . . . .	99
5.3	Discussion . . . . .	102
<b>6</b>	<b>Is Fornax 4 the nuclear star cluster of the Fornax dwarf spheroidal galaxy?</b>	<b>105</b>
6.1	Introduction . . . . .	106
6.2	Observations and data reduction . . . . .	108
6.2.1	Artificial Stars Test . . . . .	108
6.3	Structural Parameters . . . . .	109
6.3.1	Differential extinction . . . . .	113
6.4	Age and metallicity of Fornax 4 . . . . .	114
6.5	Stellar population characterization . . . . .	116
6.5.1	The RGB width analysis . . . . .	117
6.5.2	The Horizontal Branch analysis . . . . .	120
6.6	Discussion . . . . .	125
<b>7</b>	<b>Conclusions and Future Work</b>	<b>128</b>
7.1	Conclusions . . . . .	128
7.2	Avenues for Future Study . . . . .	132
<b>Bibliography</b>		<b>136</b>

# List of Tables

2.1	Log of the HST observations (part 1). . . . .	28
2.2	Log of the HST observations (part 2). . . . .	29
2.3	List of clusters in the HST survey with information on the galaxy, age and mass and respective references. . . . .	29
3.1	Information on the age of the clusters in the HST survey and probabil- ity that their red giant branch distribution is bimodal. . . . .	60
5.1	Parameters of the clusters analysed in this Chapter. . . . .	98
6.1	Properties of Fornax 4 derived in this work. . . . .	116

# List of Figures

1.1	HST images of massive star clusters of different ages in the Magellanic Clouds. . . . .	6
1.2	Colour-magnitude diagram of NGC 2808 and schematic colour-magnitude diagram of a GC. . . . .	9
1.3	Colour-magnitude diagrams of NGC 2808 and NGC 6752. . . . .	11
1.4	Synthetic spectra for red giant branch stars with different chemical compositions. . . . .	13
1.5	Colour-magnitude diagram of NGC 6752 and (anti-)correlations for light element abundances. . . . .	13
1.6	Colour-magnitude diagram of NGC 1846. . . . .	14
1.7	Inferred age spreads versus age of the cluster. . . . .	15
1.8	Correlations between abundance spreads and cluster mass. . . . .	22
2.1	Synthetic spectra of red giant branch stars with different chemical compositions. . . . .	26
2.2	Colour-magnitude diagram of NGC 419 before and after the field star subtraction. . . . .	31
2.3	Optical colour-magnitude diagrams of NGC 419 with selected red giant branch stars. . . . .	35

2.4	UV colour-magnitude diagrams of NGC 419 with selected red giant branch stars. . . . .	37
2.5	CUBI vs. B colour magnitude diagram of NGC 419 and histogram of selected red giant branch stars. . . . .	38
2.6	CUnBI vs. B colour magnitude diagram of NGC 419 and histogram of selected red giant branch stars. . . . .	39
2.7	CUBI and CUnBI vs B colour-magnitude diagrams of NGC 419 with theoretical models superimposed. . . . .	41
3.1	Colour-magnitude diagram of NGC 1978 before and after the field star subtraction. . . . .	47
3.2	UV colour magnitude diagram of NGC 1978. . . . .	47
3.3	UV colour magnitude diagram of NGC 1978 and histogram of the distribution of red giant branch stars in UV colours. . . . .	48
3.4	UV and optical colour magnitude diagrams of NGC 1978. . . . .	49
3.5	Optical colour-magnitude diagram of NGC 1978. . . . .	51
3.6	Cumulative distribution of first and second population stars as a function of distance from the centre of NGC 1978. . . . .	53
3.7	Optical colour-magnitude diagrams of all the clusters in the HST survey with selected red giant branch stars superimposed. . . . .	53
3.8	CUnBI vs. B colour-magnitude diagram of NGC 1978 and NGC 1783 and histograms of the distribution of the first and second populations in CUnBI colours. . . . .	56
3.9	Histograms of the distribution of red giant branch stars in CUnBI colour for all the clusters in the HST survey. . . . .	57

3.10	Correlation between N abundance spread (proxy from UV photometry) and age of the clusters. . . . .	59
3.11	CUnBI vs B colour-magnitude diagram of NGC 1978 with theoretical models superimposed. . . . .	62
3.12	Cluster mass versus cluster age diagram. . . . .	63
4.1	Colour magnitude diagram of NGC 1978 with BASTI isochrone superimposed. . . . .	70
4.2	Photometric errors of NGC 1978 red giant branch and sub-giant branch stars as a function of distance from the cluster centre and for different HST filters. . . . .	72
4.3	Optical colour-magnitude diagram of NGC 1978 with selected sub-giant branch stars. . . . .	73
4.4	UV colour-magnitude diagram of NGC 1978 with selected sub-giant branch stars. . . . .	74
4.5	Histogram of the distribution of selected sub-giant branch stars in NGC 1978. . . . .	75
4.6	UV colour-magnitude diagram of NGC 1978 with selected sub-giant branch stars and theoretical models superimposed. Gaussian models reproducing the histograms of the distribution of red giant branch and sub-giant branch stars of NGC 1978 in UV colours. . . . .	76
4.7	Optical colour-magnitude diagram of observed (left) and simulated (right) sub-giant branch stars. . . . .	78
4.8	Isochrones of different ages, spaced by 20 Myr (left). Relation between $\Delta\text{Mag}$ and $\Delta\text{Age}$ for the sub-giant branch part of the isochrones (right). . . . .	79

4.9	Optical colour-magnitude diagram of NGC 1978 with selected main sequence turnoff stars. . . . .	81
4.10	Histogram of the distribution of selected main sequence stars in optical colours (left). Simulation of main-sequence turnoff widths in comparison with the width from the data as a function of $\Delta\text{Age}$ . . . . .	82
5.1	Colour-magnitude diagram of NGC 2121 before and after the field star subtraction. . . . .	87
5.2	ACS and WFC3 map for Lindsay 38 (top) and Lindsay 113 (bottom) .	88
5.3	Colour-magnitude diagrams of NGC 2121 (left) and NGC 2155 (right) before and after the field star subtraction. . . . .	89
5.4	Colour magnitude diagrams of NGC 2121, Lindsay 113, Lindsay 38 with selected red giant branch stars. . . . .	91
5.5	CUBUn vs B colour-magnitude diagrams of the clusters analysed in this Chapter with selected red giant branch stars. . . . .	92
5.6	Histograms of the distributions of observed and simulated red giant branch stars in UV colours for the clusters analysed in this Chapter. . . . .	94
5.7	Colour-magnitude diagrams of NGC 2121, NGC 2155 and Lindsay 38 with isochrones superimposed. . . . .	97
5.8	Colour magnitude diagrams of Lindsay 113 with isochrones superimposed. . . . .	98
5.9	Correlation between N abundance spread (proxy from UV photometry) and age of the cluster. . . . .	101
6.1	Stellar density of Fornax 4 as a function of radius. . . . .	109
6.2	WFC3 map of Fornax 4 with the area used for the background highlighted. . . . .	110

6.3	Colour-magnitude diagram of Fornax 4 before and after the field star subtraction.	111
6.4	Differential reddening map for Fornax 4.	113
6.5	Colour-magnitude diagram of Fornax 4 before and after the differential reddening correction.	114
6.6	Colour magnitude diagrams of Fornax 4 with isochrones superimposed.	115
6.7	Histograms of the distribution of observed and simulated red giant branch stars in Fornax 4.	118
6.8	Colour-magnitude diagram of Fornax 4 with variable stars superimposed.	121
6.9	Colour-magnitude diagram of observed and simulated horizontal branch stars in Fornax 4.	122
6.10	Colour-magnitude diagram of observed and simulated horizontal branch stars in Fornax 4 with a spread in iron of +0.4 dex.	124
6.11	Colour-magnitude diagram of observed and simulated horizontal branch stars in Fornax 4 with a spread in He of 0.03.	125
7.1	Final cluster age versus cluster mass diagram.	130

# Chapter 1

## Introduction

In this chapter I discuss the main open questions and motivation that led to my thesis work. I describe the main observational properties of globular clusters and their importance in a scientific context in Section §1.1. In Section §1.2 I report on the fairly recent discovery of young massive clusters in the local Universe and how this remarkably impacted our approach to cluster formation theories. Section §1.3 describes the main observational evidence of multiple stellar populations in globular clusters. In Section §1.4 I outline the phenomena of the extended main sequence turnoff and split main sequence in young massive clusters. In Section §1.5 I report on a few models proposed to explain the origin of multiple populations, while Section §1.6 describes which properties are keys for the onset of such a phenomenon. I finally summarise the introduction in Section §1.7.

### 1.1 Globular clusters

Globular clusters (GCs) are agglomerates of hundreds of thousands of stars that are gravitationally bound. They show a roughly spherical shape and are extremely dense objects. Indeed, their typical half-light radius, i.e. the radius at which half the total light of the cluster is enclosed, is of the order of a few parsecs ([McLaughlin & van der Marel, 2005](#)) and their densities in the core reach about  $10^4 \text{M}_\odot \text{pc}^{-3}$ , with cluster

masses spanning  $\sim 10^4 - 10^6 M_{\odot}$ .

GCs are among the oldest objects with ages similar to that of the Universe itself (VandenBerg et al., 2013). Before the precise age dating of the Universe through Planck (Planck Collaboration et al., 2018), the GCs used to provide a quite strong lower bound to the age of the Universe. Besides being among the oldest stellar systems, GCs are also found to host stars with a chemical composition that has a much lower heavy element content than that of our Sun. Indeed, their metallicity spans values of  $-2.5 \lesssim [\text{Fe}/\text{H}] \lesssim 0$ , i.e. up to solar (Gratton, Carretta & Bragaglia, 2012).

It is well established that almost all galaxies have a GC system, if they are massive enough (Brodie & Strader, 2006b). The MW hosts around 150 GCs (Harris, 1996), which are mainly distributed within the inner halo, while M87 contains several thousands of GCs (McLaughlin, Harris & Hanes, 1994). More generally, the more luminous the galaxy, the more GCs this hosts (Harris, 1991). However, a useful quantity is the GC specific frequency,  $S_N$ , i.e. the number of GCs present within a galaxy per unit mass/luminosity (Harris & van den Bergh, 1981). This has been used to connect GCs populations with galaxy formation mechanisms. Indeed, while early type massive galaxies have numerous GC populations, dwarf galaxies can have comparable or higher GC number per unit luminosity/mass, i.e. higher values of  $S_N$  (one example is the Fornax dwarf spheroidal galaxy, Chapter 6).

The old ages and metal-poor chemical composition hint that GCs were born during the early stages of the Galaxy's formation. Additionally, the brightness and compactness of GCs allow to trace galaxy structures up to very far galactocentric distances. GCs can then be used to understand the build-up of our own and other galaxies (Brodie & Strader, 2006b). This is being fostered by the discovery of scaling relations between GC and the properties of their host galaxies. One of the most interesting has been the observation of a bimodal colour distribution (i.e. metallicity distribution) of GC systems within galaxies (e.g. Gebhardt & Kissler-Patig 1999; Forbes & Forte 2001), which provides fundamental clues to understand how galaxies formed and assembled.

GCs are considered essential testbeds for a wide variety of astronomical problems. As

they host stars in almost all stellar evolutionary stages, studying the properties of their stellar populations is also crucial to validate stellar evolution theories (e.g. [Ferraro et al. 2000](#); [Salaris et al. 2014](#)). GCs are also systems where an important variety of stellar exotica (e.g. white dwarfs, X-ray binaries, black holes, blue stragglers) is present and this allows to investigate such fascinating objects in great details (e.g. [Göttgens et al. 2019](#)). Moreover, their internal star motion is a benchmark for studies of stellar dynamics, body encounters and mutual stellar interactions.

While significant progress has been recently made, still little is known about the formation and evolution of GCs. Modern theories for GC formation ([Forbes et al., 2018](#); [Kruijssen et al., 2019](#)) envision that the process at the basis of the formation of clusters is simply a star formation process occurring at extreme densities, i.e. they are the extreme end of a continuous density distribution of star-formation in galaxies. Hence, forming star clusters might provide major insights into open questions regarding the formation of stars.

In the next Sections, I report on how traditional views of GCs have been completely revolutionised in the past few decades as a result of new observational advances. The latter have led many authors to thoroughly re-think globular clusters formation theories and has opened up new intriguing avenues for the origin of GCs.

## 1.2 Young Massive Clusters

In the MW, another type of clusters is found preferentially in the disk of the Galaxy. These are called open clusters (OCs) and are low mass ( $\lesssim 10^3 M_\odot$ ), low densities ( $\lesssim 10^3 M_\odot pc^{-3}$ ) aggregates of stars spanning a wider range of ages than GCs ([Mermilliod, 1995](#); [Salaris, Weiss & Percival, 2004](#)). Since their properties and location are very different from GCs with little overlap between the two populations, it was thought originally that OCs and GCs are simply different systems, implying that their formation must also have undergone through separate channels. Due to their old age, it was proposed that special conditions only present in the early Universe must be responsible

for the formation of GCs (e.g. [Peebles & Dicke 1968](#); [Fall & Rees 1985](#)).

Such a view was revolutionised with the discovery of many young massive clusters (YMCs) in the local Universe, that was enabled by the high resolution and sensitivity offered by the Hubble Space Telescope (HST). [Holtzman et al. \(1992\)](#) found that several compact “bright blue clusters” are forming in the starburst NGC 1275. Their magnitudes and colours pointed towards young ( $<100$  Myr) and massive ( $> 10^6 M_{\odot}$ ) sources. Indeed, YMCs have very similar properties than that of GCs, e.g. high masses and densities, which in a few cases exceed those of GCs (e.g. [Portegies Zwart, McMillan & Gieles 2010](#)). This study was the first of many works that found YMCs in any local galaxy. For instance, YMCs were found in other starbursts (e.g. the Antennae colliding galaxies, [Whitmore & Schweizer 1995](#)), in nearby spirals (e.g. [Larsen & Richtler 2000](#)) as well as in dwarf galaxies (e.g. [Billett, Hunter & Elmegreen 2002](#)).

Additionally, without going too far away, our nearest galaxy companions, the Large and Small Magellanic Clouds (LMC/SMC) host a large number of such YMCs, which also span a wide range of ages. Among these (see Fig. 1.1), we find the  $\sim 2$  Myr old R136 ([Crowther et al., 2016](#)), the  $\sim 100$  Myr old NGC 1850 ([Niederhofer et al., 2015](#)), NGC 1856 ( $\sim 300$  Myr, [Milone et al. 2015](#)), NGC 1806 ( $\sim 1.5$  Gyr, [Goudfrooij et al. 2014](#)) all belonging to the LMC and finally NGC 416 in the SMC ( $\sim 6$  Gyr, [Glatt et al. 2008b](#)). Such clusters are all more massive than  $10^5 M_{\odot}$ , which is comparable to the mass of the ancient GCs in the MW. Although less massive ( $\sim 10^4 M_{\odot}$ ), a few young star clusters are also observed in the MW, narrowing the gap between OCs and GCs (e.g. Trumpler 14 and Westerlund 2, [Portegies Zwart, McMillan & Gieles 2010](#)).

Since YMCs are ubiquitous in nearby galaxies and have very similar properties to those of GCs, it became quite natural to think that YMCs are just young counterparts of GCs, i.e. they are the same objects but seen at different stages of their lifetimes (e.g. [Adamo & Bastian 2015](#)). This bolsters the idea that GCs formation is viewed as a star formation process at the extremes of the density distribution, rather than a special mechanism that only occurred in the early Universe. Current models for GC formation are indeed based on a more global massive cluster formation approach, where the formation and co-evolution of the GCs population and its host galaxy is built on ob-

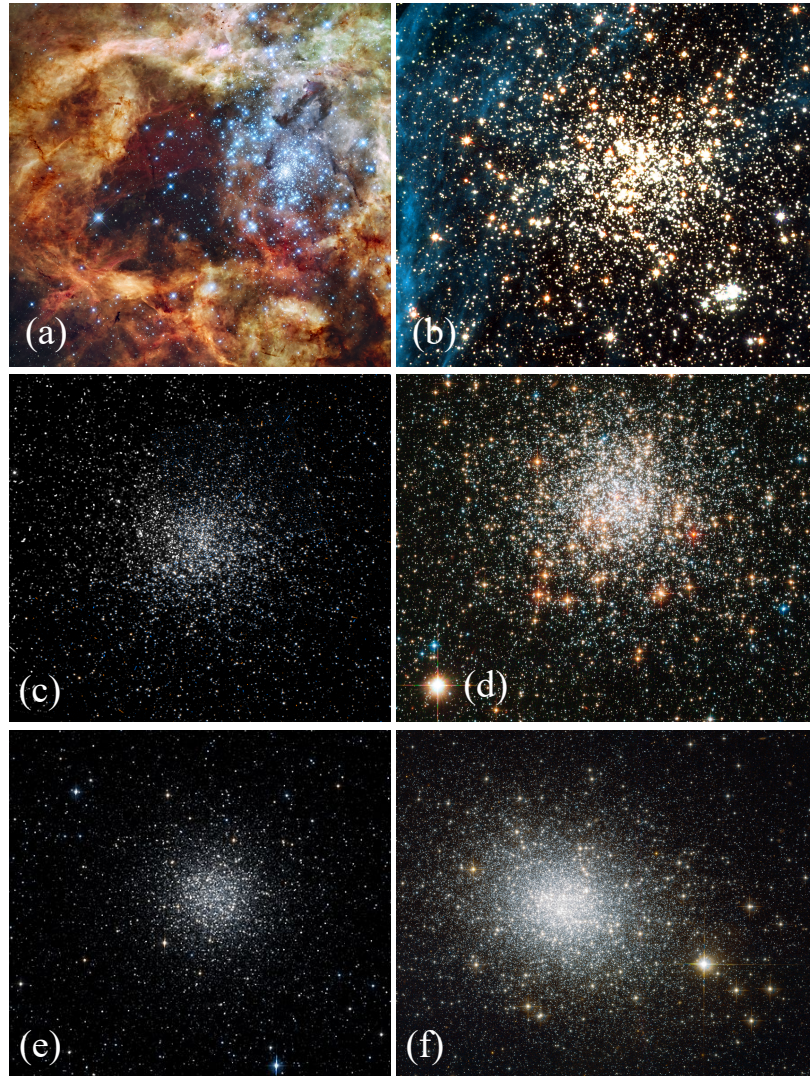


Figure 1.1: HST images of massive ( $> 10^5 M_{\odot}$ ) star clusters in the Magellanic Clouds. Panel (a) R136,  $\sim 2$  Myr old, (b) NGC 1850,  $\sim 100$  Myr old, (c) NGC 1856 ( $\sim 300$  Myr), (d) NGC 1806 ( $\sim 1.5$  Gyr), (e) NGC 416 ( $\sim 6$  Gyr), (f) NGC 121 ( $\sim 11$  Gyr). References in the text. Credits: HST/NASA/ESA.

servations of YMCs properties in the local Universe ([Kruijssen, 2015](#); [Li et al., 2017](#); [Pfeffer et al., 2018](#)). In support of this, recent works on star cluster populations found that the efficiency of cluster formation is closely linked to the gas pressure in galaxies, highlighting that the properties of clusters appear tightly correlated to those of the host galaxy (e.g. [Adamo et al. 2015](#); [Messa et al. 2018](#)).

By using gravitational lensing techniques, [Vanzella et al. \(2017, 2019\)](#) have discovered compact objects (radii of 20-40 pc) at redshifts  $z = 2 - 6$ , which most likely represent forming proto-GCs. They also estimate their ages and masses and these are very similar to those of YMCs observed in the local Universe. However, resolving individual stars and stellar populations of such distant objects will not be possible in the near future. Hence, if YMCs are indeed young globular clusters, their characterisation would provide unprecedented insights into GC formation theories as we would be able to take advantage of local observations to study physical processes that also occurred at high redshifts.

The work of my thesis is focused around this first open question in GCs studies: are young star clusters precursors to the ancient globular clusters? In order to reply to this question, it is crucial to establish whether these two classes of objects have also similar stellar populations. I discuss stellar populations in GCs in the next Section §[1.3](#).

## 1.3 Chemical abundance variations in GCs

Traditionally, GCs were thought to be a good example of simple stellar populations (SSPs), where all the stars within a given cluster have the same age and chemical composition. Stars belonging to a SSP have then initial constant chemical abundances (from He up to the heaviest metals) and masses distributed according to an initial stellar mass function (IMF). In the colour-magnitude diagram (CMD), this translates into a single isochrone (see the top panel of Fig. [1.2](#), where the CMD of the MW GC NGC 2808 is shown), which corresponds to the locus of stars with the same age and chemical composition, but different masses. Each area of the CMD is then a different stage of

the evolution of a star. This is shown in the bottom panel of Fig. 1.2, where a schematic representation of a GC CMD highlights the different branches of stellar evolution.

The lifetime and evolution of the star depends on the initial mass, here we report the typical evolution of a low mass star, i.e.  $0.8\text{--}1 M_{\odot}$ , which also represents the typical mass range of stars in an old GC. Very briefly, in the Main Sequence (MS), stars are burning hydrogen in their core, converting it into helium through nuclear fusion. When the hydrogen in the core is exhausted, the core begins to contract while the outer envelope expands and cools down. The star then leaves the MS moving through the subgiant branch (SGB) to the red giant branch (RGB) phase, where H is burning in a shell around the core, which is inert at this stage, as the central temperature is still not high enough to reach He fusion. This is reached at the tip of the RGB with the He-flash, after which the core of the star (after becoming electron degenerate) starts converting He into carbon and oxygen. The so-called Horizontal Branch (HB) phase starts, whose morphology depends on the initial He composition, which is exploited later in Chapter 6. It also strongly depends on the metallicity of the population (more metal rich stars show redder HBs than metal-poor ones) as well as the amount of mass lost during the RGB phase. When also He is exhausted in the core, again the core contracts and He starts burning in a shell. The envelope expands and the star, now in its Asymptotic Giant Branch (AGB) phase, experiences heavy mass loss in the form of stellar winds. This terminates in the star losing all its envelope and becoming a white dwarf, ending up in the lower left corner of the CMD.

However, already in the late '70s, it was clear that GCs are not SSPs (e.g. Kraft 1979). Star-to-star variations in cyanogen (CN, mainly a proxy for the N abundance) and in the CH molecule (proxy for the C abundance) were commonly observed in red giants and main sequence stars belonging to Galactic GCs (e.g. Hesser & Bell 1980; Norris et al. 1981), additionally finding that CN and CH are anti-correlated. This means that stars which show an enhanced N abundance also have a depleted C abundance, recalling the by-products of stellar nucleosynthesis processes (i.e. hot H-burning through the CNO cycle). For this reason, originally it was proposed that such chemical “anomalies” were generated by evolutionary mixing in the interiors of stars. However, it was later

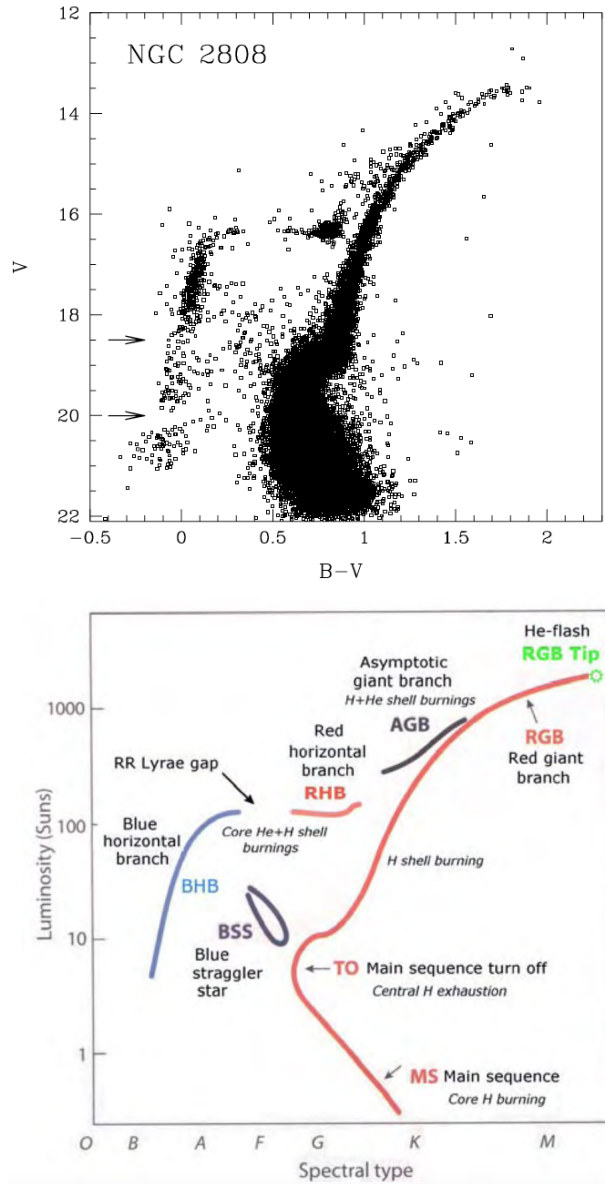


Figure 1.2: Top Panel: HST WFPC2 Colour-magnitude diagram of NGC 2808, ancient GC in the MW (Bedin et al., 2000). Bottom Panel: Schematic representation of a GC colour-magnitude diagram with evolutionary stages highlighted, from <http://www.astro.caltech.edu/~george/ay20/eaa-globcl.pdf>.

recognised that such C and N variations were instead due to stars born with different initial chemical compositions (e.g. [Cannon et al. 1998](#)), as mixing could not explain the presence of abundance anomalies in unevolved stars, such as main sequence turnoff stars.

It is with the advent of the exquisite photometric accuracy provided by the HST that a major breakthrough was made in this field. The chemical anomalies observed in GCs with lower resolution spectroscopy in the '80s were recognised as multiple stellar populations (MPs), thanks to the CMDs of GCs showing multiple discrete sequences in different evolutionary stages (e.g. [Bedin et al. 2004](#); [Piotto et al. 2007](#), see next Section, §1.3.1 for a description of MPs from photometric signatures). At the same time, in the late '90s/early 2000s, the multi-object high resolution spectrographs on the large ground based telescopes (such as VLT, Keck) enabled a massive spectroscopic follow-up and characterisation of the discrete sequences that were mapped into MPs with their respective chemical signatures.

Hence, GCs host subpopulations of stars with distinctive light element abundance pattern ([Gratton, Carretta & Bragaglia 2012](#)). MPs manifest in the form of (anti-) correlated light element variations. While some GC stars have the same C, N, O, Na abundances as field stars with the same metallicity (first population, FP), a significant fraction of cluster members systematically display enhanced N, Na (and in a few cases Al), along with depleted C and O (and sometimes Mg; [Cannon et al. 1998](#); [Carretta et al. 2009b,a](#), second population, SP).

Helium is also observed to vary while, generally, the iron content (i.e. [Fe/H]) and Fe-peak elements remain constant as well as the C+N+O sum, except for a few clusters. Interestingly, it seems like such chemical anomalies are unique to GC systems, i.e. dense stellar systems, since they are rarely found in the field ( $\sim 3\%$  in the MW halo, [Martell et al. 2011](#)) and not found in OCs (e.g. [MacLean, De Silva & Lattanzio 2015](#)).

It is beyond of the scope of this thesis to report a complete summary of all the observational evidence and theoretical efforts made so far, thus we refer the interested reader to the most recent reviews on MPs for more details, e.g. [Gratton, Carretta & Bragaglia](#)

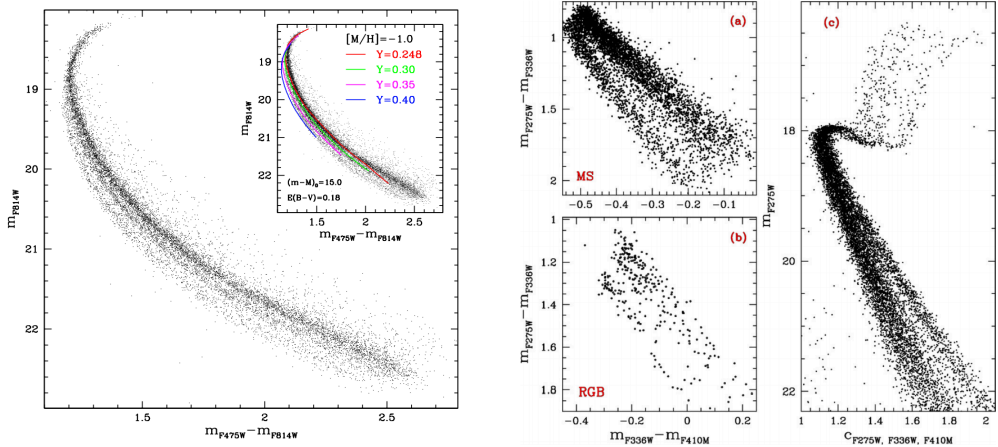


Figure 1.3: Left panel:  $m_{F475W} - m_{F814W}$  vs.  $m_{F814W}$  CMD of NGC 2808 from [Piotto et al. \(2007\)](#). Middle panels:  $m_{F336W} - m_{F410M}$  vs.  $m_{F275W} - m_{F336W}$  plots for MS (a) and RGB (b) stars in NGC 6752 from [Milone et al. \(2013\)](#). Right panel:  $C_{F275W,F336W,F410M} \equiv (F275W-F336W)-(F336W-F410M)$  vs.  $m_{F814W}$  CMD of NGC 6752 from [Milone et al. \(2013\)](#).

[\(2012\)](#); [Bastian & Lardo \(2018\)](#); [Gratton et al. \(2019\)](#).

### 1.3.1 Multiple populations from photometry

While spectroscopic techniques are fundamental to directly estimate the chemical abundance spreads in GCs, it is only thanks to precision photometry that it was possible to access the most crowded regions in the center of clusters, allowing to study the radial distributions of the different populations and estimate the fractions of the anomalous stars. Additionally, photometric techniques allow to study 100s–1000s of stars per cluster instead of just a few through traditional spectroscopy. One of the best picture of MPs has indeed been provided by the HST UV Legacy Survey of Galactic Globular Clusters (PI G. Piotto), where almost 60 Galactic globular clusters were imaged in HST filters, allowing to analyse MPs features and correlations with global properties of the clusters (e.g. [Piotto et al. 2015](#); [Milone et al. 2017](#); [Nardiello et al. 2018](#)).

Compared to Fig. 1.2, the CMDs of GCs are actually much more complex when accurate photometry is employed. Two examples are reported in Fig. 1.3: the left panel shows the HST Advanced Camera for Surveys (ACS) optical CMD of NGC

2808 zoomed in the MS ([Piotto et al. 2007](#)). Note that this is the same cluster imaged in Fig. 1.2 that instead was based on HST WFPC2 data. A first look already reveals that there are at least three distinct sequences. The middle and right panels are from [Milone et al. \(2013\)](#) and show colour-colour plots as well as the CMD of NGC 6752 in UV colour combinations. As before, the CMD is not composed of a single sequence as expected from an SSP, but multiple and discrete sequences are observed throughout all the evolutionary stages (from MS up to the RGB, see panel c). Depending on the photometric filters used (and the evolutionary stage of stars), the CMDs are sensitive to different chemical elements.

Optical colours (like  $B,V,I$ ) trace structural changes in the stars (i.e. luminosity and effective temperature), thus are sensitive to He variations ([Salaris et al. 2006](#), see left panel of Fig. 1.3). Filters in bandpasses with wavelengths  $<4500\text{\AA}$  (i.e. UV) primarily trace C, N, O variations in stars with cool atmospheres, as they encompass molecular features sensitive to such elements (NH, CH, CN, see middle and right panels of Fig. 1.3, [Sbordone et al. 2011](#); [Piotto et al. 2015](#)). This is shown in Figure 1.4, where [Sbordone et al. \(2011\)](#) report the comparison between two synthetic spectra, one with field-like (black curve) and one with anomalous (red curve) composition, i.e. enhanced N, depleted C and O. Superimposed are the transmission curves of several photometric filters (more details in the caption). As a consequence, field-like and anomalous stars follow distinct sequences when UV filters are used, i.e. colour spreads and splits observed in UV CMDs clearly correlate with N variations (e.g., [Marino et al. 2008](#)).

Figure 1.5 (left panel) shows the CMD of the MW GC NGC 6752 in the  $C_{U,B,I} \equiv (U-B)-(B-I)$  vs. B space.  $C_{U,B,I}$  is a combination of colours which have been shown to be very effective at separating MPs in the CMD ([Monelli et al. 2013](#), see §1.3.1 and Chapter 2, §2.2.4). Indeed, a typical GC optical and near-ultraviolet (UV) CMD shows discrete multiple sequences at almost every evolutionary stage, which indicate the presence of MPs. RGB stars highlighted with different colours correspond to different chemical compositions. The right panels of Fig. 1.5 show the (anti-)correlations among the stars for several light-elements.

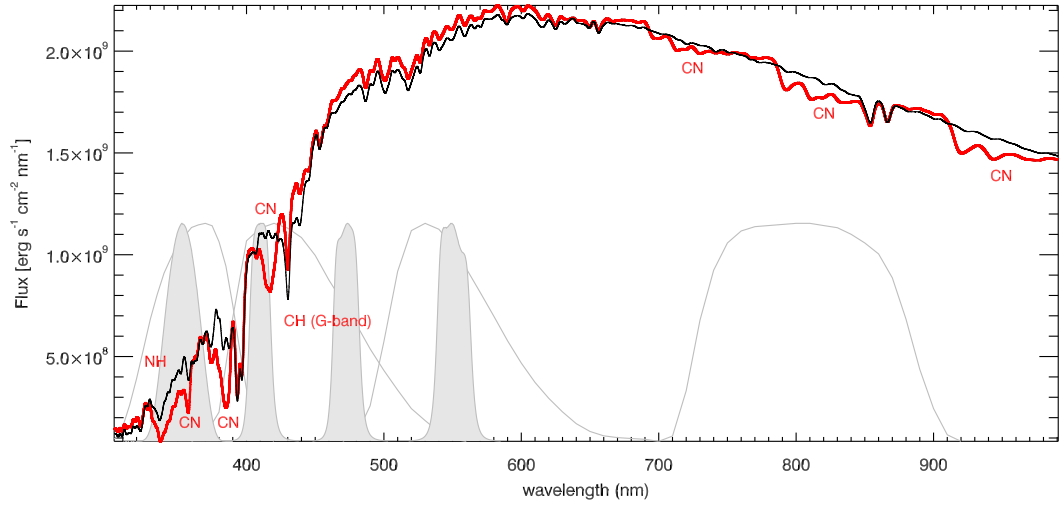


Figure 1.4: RGB UV/optical synthetic spectra with field-like (black) and anomalous (red) composition from Sbordone et al. (2011). Superimposed are the transmission curves of Johnson-Cousins filters U, B, V, and I (thin grey lines from left to right) and for the Strömgren uvby filters (grey-shaded areas).

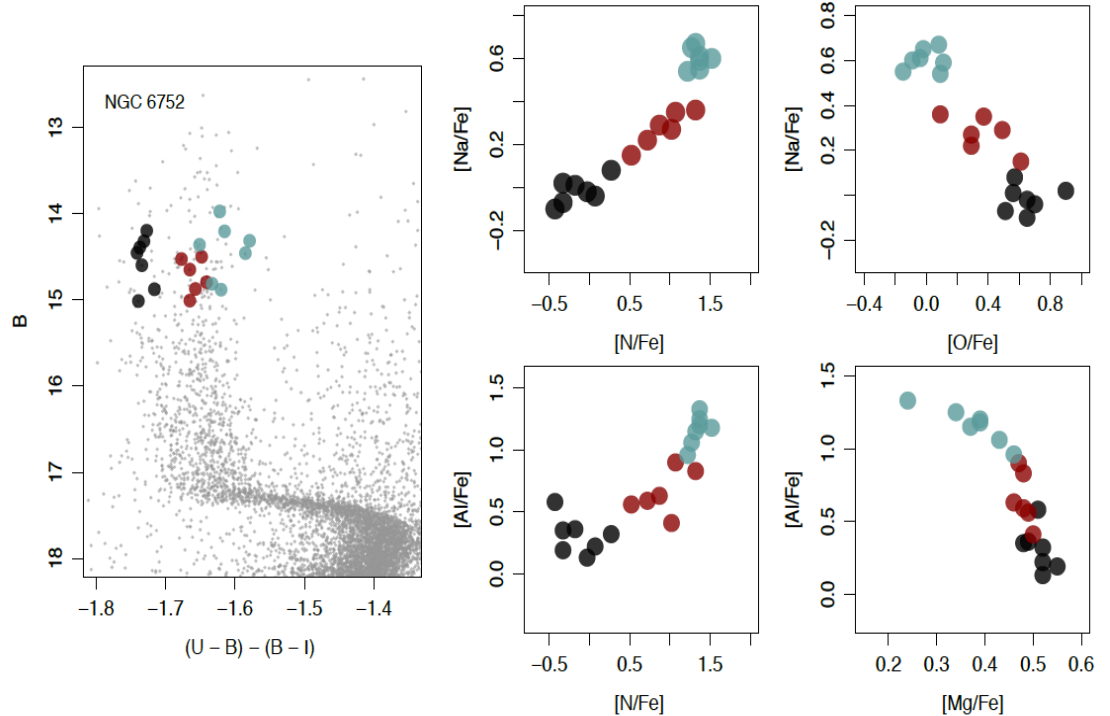


Figure 1.5: Left panel: CMD of NGC 6752 in  $C_{U,B,I}$  vs. B space from Bastian & Lardo (2018). RGB stars highlighted with different colours (black, red, green) correspond to different chemical compositions: pristine, moderate and enhanced Na content. Right panels: (anti-)correlations for light element abundances.

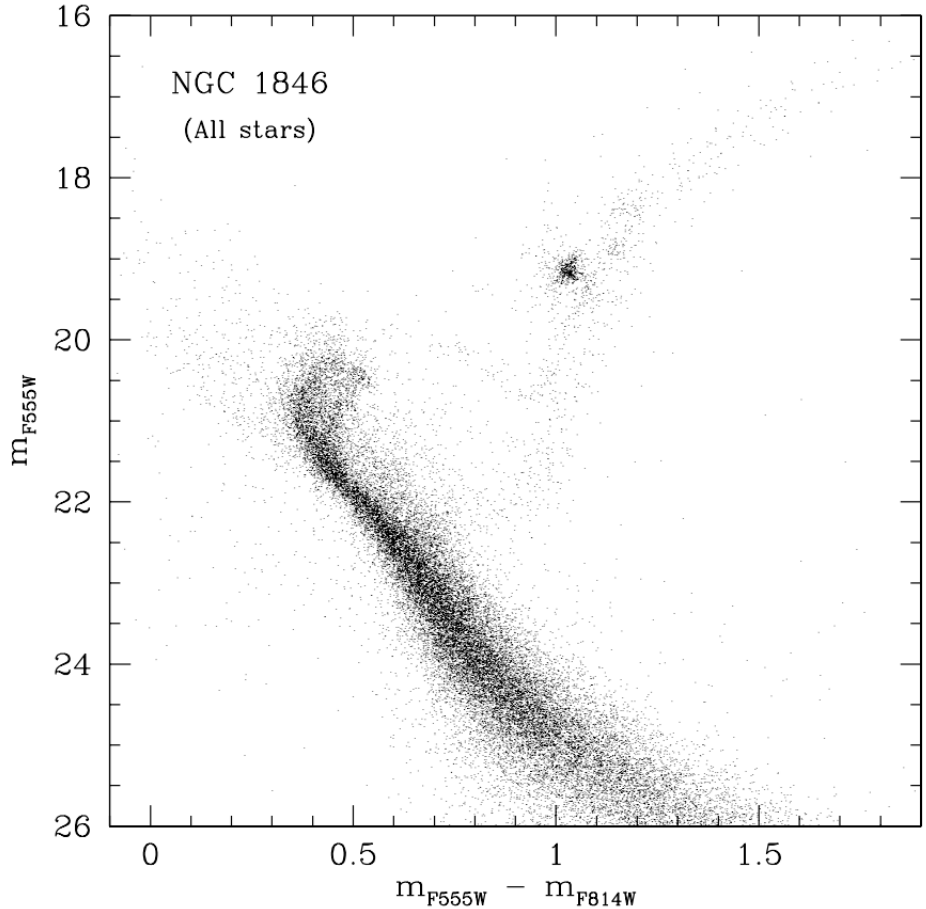


Figure 1.6:  $m_{\text{F}555\text{W}} - m_{\text{F}814\text{W}}$  vs.  $m_{\text{F}555\text{W}}$  CMD of NGC 1846 from [Mackey & Broby Nielsen \(2007\)](#).

## 1.4 The main sequence and turnoff of YMCs

Two other features detected in all CMDs of young star clusters which are not consistent with the original view of clusters, i.e. SSPs, are the extended main sequence turnoff (eMSTO) and split main sequences (MSs). The eMSTO feature was observed for the first time by [Bertelli et al. \(2003\)](#) and [Mackey & Broby Nielsen \(2007\)](#) (see Fig. 1.6) and it consists of a broadening in the turnoff (TO) region in the CMDs of young massive clusters. Such a feature is not consistent with a single isochrone and cannot be explained either by photometric errors or stellar binarity. So far, it is detected in all young ( $> 20$  Myr, e.g. [Milone et al. 2015](#); [Bastian et al. 2016](#)) and intermediate-age ( $< 2$  Gyr, e.g. [Mackey et al. 2008](#); [Milone et al. 2009](#)) massive clusters, as well as in many less massive open clusters ([Bastian et al., 2018](#); [Cordoni et al., 2019](#)).

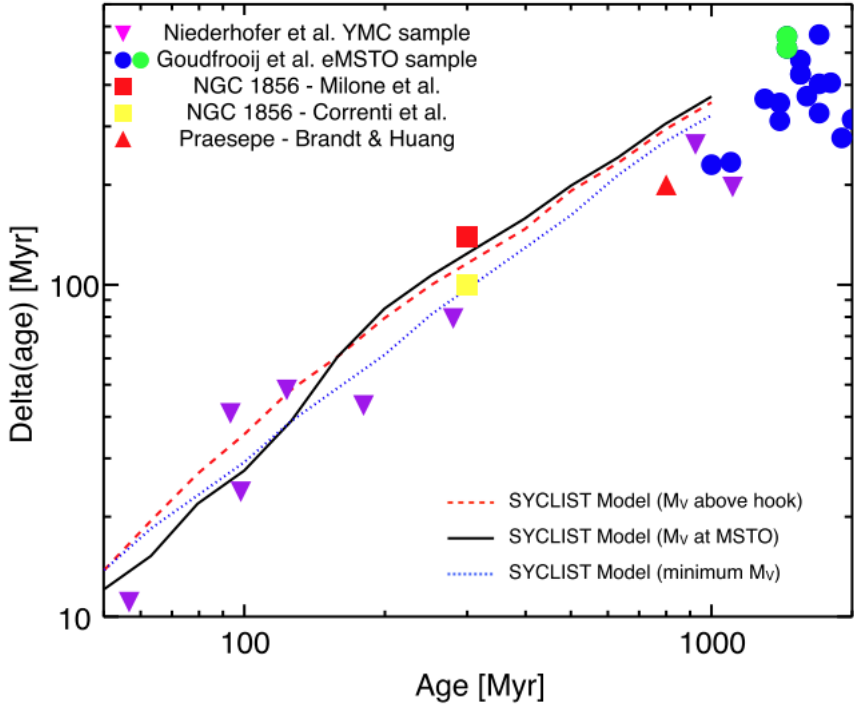


Figure 1.7: Inferred age spreads (in eMSTO) versus age of the cluster from [Niederhofer et al. \(2015\)](#). Symbols indicate values from different observational studies. The lines represent the prediction of the SYCLIST models if rotation-induced MSTO spreads are assumed to be age spreads.

It was originally thought that the eMSTO was due to age spreads of up to 700 Myr caused by multiple star forming events (e.g. [Milone et al. 2009](#); [Goudfrooij et al. 2014](#)). Such a scenario has been demonstrated to have several caveats. Among these, massive clusters should be forming stars for the first 10s to 100s Myr of their lives, while no clusters with ages of  $\sim 10$  Myr or older have been found to host current star formation events ([Bastian et al., 2013a](#); [Cabrer-Ziri et al., 2016a](#)). Additionally, a clear correlation between the inferred age spread and the age of the cluster is observed, thus suggesting a stellar evolutionary effect is the cause (Fig. 1.7, [Niederhofer et al. 2015](#)).

Indeed, recent works have shown that the eMSTO is likely due to a single age population with a range of stellar rotation rates ([Bastian & de Mink, 2009](#); [Niederhofer et al., 2015](#); [Brandt & Huang, 2015](#); [Kamann et al., 2018](#); [Gossage et al., 2019](#); [Kamann et al., 2020](#)). The relation from [Niederhofer et al. \(2015\)](#) shown in Fig. 1.7 is consistent with predictions from such a scenario. Additionally, [Brandt & Huang \(2015\)](#) and

[Georgy et al. \(2019\)](#) predict that by an age of  $\sim 2$  Gyr the eMSTO should disappear according to the rotation scenario. In the stellar rotation paradigm, clusters older than 2 Gyr would not be expected to host eMSTOs, since stars on the TO in 2 Gyr old clusters are able to develop convective envelopes, and subsequently host magnetic fields which can brake the star, i.e. no rapid rotators would be expected. I report in Chapter 4 how the work presented in this thesis placed constraints on the origin of the eMSTO phenomenon in young massive clusters.

Another feature observed in YMCs (in the MCs, where it is possible to resolve CMDs down to the MS) is the presence of a split MS when these are imaged in UV or blue filters ([Milone et al., 2015, 2018](#)). This is different from what is seen in optical CMD in ancient GCs (Fig. 1.3), as stellar isochrones including chemical abundance spreads are not able to reproduce the observed bi-modal MSs in YMCs ([Milone et al., 2015](#)).

Theoretical works have shown that stellar rotation could explain the split MSs if one of the populations rotates at very slow velocities ( $\omega < 0.3$ ) while the other rotates at critical break-up speed ( $\omega \sim 0.9$ , e.g. [D'Antona et al. 2015](#)). The presence of stars rotating at break-up velocities in YMCs has been demonstrated in [Bastian et al. \(2017\)](#), [Milone et al. \(2018\)](#) where a large number of Be stars<sup>1</sup> have been discovered. Additionally, in quite a number of recent works, the projected rotational velocities of stars belonging to different branches of the MS and eMSTO was measured and a significant difference in rotation rate has been reported ([Dupree et al., 2017](#); [Kamann et al., 2018](#); [Bastian et al., 2018](#); [Marino et al., 2018](#); [Kamann et al., 2020](#)). These studies further support a scenario where the split MSs and eMSTO features are caused by a bi-modal distribution of rotational velocities. How these populations are formed is still an open question.

Unfortunately, many authors also refer to the term “multiple populations” as the presence of broadenings and/or splittings in the TO and MS regions in CMDs of young/intermediate-age clusters. This has caused a lot of confusion in the field as it equates what we see in the young clusters with the abundance spreads observed in

---

<sup>1</sup>Be stars rotate very rapidly and show decretion discs that emit in H $\alpha$  due to the ionisation of the disc by the star itself.

the ancient clusters. However, no star-to-star chemical abundance variations appear to be associated with this phenomenon ([Mucciarelli et al. 2008, 2012, 2014](#), see also Chapter 2, where no MPs are observed in the RGB of such young clusters). Thus, we will use the term MPs to only refer to the features correlated to chemical abundance spreads.

## 1.5 Models for the origin of multiple populations

Due to the type of elements involved in the variations, chemical anomalies were thought to be caused by self-enrichment (i.e. the globular cluster enriches itself) in elements that originate from high temperature H burning in the interiors of stars, i.e. the CNO cycle, which modifies the abundances of C, N, O to convert H into He at a temperature of 20 MK. Additionally, the observations of the discreteness between two or more subpopulations ([§1.3.1](#)) brought models to require the presence of multiple epochs of star formation within the same cluster.

The general picture is that a first population of stars (FP) forms and the gas not used in star formation is expelled. This includes all the gas enriched by high mass stars and Supernovae, which needs to be cleared out to avoid the presence of iron spreads within the cluster, which are generally not observed. Next, massive stars from the FP generate stellar winds which collect in the centre of the cluster and mix up with material with “pristine” composition, i.e. the giant molecular cloud material from which the cluster originally formed. Such pristine material needs to be re-accreted from the outskirts of the cluster. This mixing is called “dilution” and currently it is one of the major problems of such scenarios. A second population (SP, i.e. the anomalous population) is eventually formed by a second burst of star formation from the mix of pristine and processed material from massive stars. Several types of massive stars have been proposed as “polluters”, i.e. the stars whose stellar ejecta contribute to generate a second star formation event within the cluster. These are: AGB stars ( $\sim 3 - 8 M_{\odot}$ , e.g. [Cottrell & Da Costa 1981](#); [D’Ercole et al. 2008](#); [D’Antona et al. 2016](#)), fast rotating massive stars (FRMS,  $\sim 15 M_{\odot}$ , [Decressin et al. 2007](#)), interacting massive binaries

( $20M_{\odot}$ , [de Mink et al. 2009](#)), very massive stars ( $>5000M_{\odot}$ , [Denissenkov & Hartwick 2014](#); [Gieles et al. 2018](#)). Depending on which polluter is advocated, such multiple generational theories predict age spreads between FP and SP from a few Myr (massive and super-massive stars) to  $\sim 30$ -200 Myr (AGB stars).

The self-enrichment models are based on the fact that the fundamental property regulating the existence of MPs in GCs is the mass of the cluster. Indeed, only clusters that are massive enough have been able to retain the stellar ejecta (i.e. stellar winds) from massive stars in order to generate a second burst of star formation. This was built on the observation that basically all massive GCs show MPs while less massive, less dense OCs do not (see §1.6).

However, multiple generations models suffer from many drawbacks. It is observed that the fraction of SP stars outnumber that of FP stars (typical fractions of SP/FP are of the order of  $\sim 60 - 80\%$ , e.g. [Milone et al. 2017](#)). Because only a small fraction of the FP mass would be processed through massive stars, the FP would not be able to provide enough mass to form the SP. For example, considering AGB stars as polluters, these can only form 4–5% of the SP stars if one assumes a standard IMF and that 100% of the mass of the AGB stars is used to form SP stars ([Bastian & Lardo, 2018](#)). This is the so-called “mass-budget” problem.

To solve the mass-budget problem, a large amount of mass loss (from the FP) has been invoked. The cluster, after forming the SP, needs to lose a very large fraction of FP stars ( $\sim 90$ -95%), meaning that the FP has to be at least  $\sim 10$ –30 times (the exact factor depends on the employed polluter) more massive at birth ([D’Ercole et al., 2008](#); [Conroy, 2012](#); [Cabrera-Ziri et al., 2015](#)). This concept is not only in contradiction with mass loss estimations from simulations ([Kruijssen, 2015](#); [Baumgardt et al., 2019](#)), but also observationally. [Larsen, Strader & Brodie \(2012a\)](#) and [Larsen et al. \(2014a\)](#) put an upper limit of  $\sim 5$  to the factor of mass lost by a GC by counting how many field stars and GCs are observed in the Fornax, WLM and IKN galaxies, assuming that all the stars in the field came from disrupted GCs. In the next Section §1.6, I also report other key observations that are in disagreement with high mass loss considerations.

Additionally, in the AGB and fast rotating massive stars scenarios, it is not clear how the cluster is able to re-accrete the pristine material from the surroundings. The need for dilution is invoked to explain some chemical patterns and especially the chemical trend with lithium. Lithium is destroyed in p-capture processes, hence stars that are enhanced in N through H burning should be depleted in Li. Some GCs do not show Li variations between FP and SP stars (e.g. [Mucciarelli et al. 2011](#)). The explanation of the Li trend is often result of ad-hoc assumptions and extreme fine tuning of the scenarios.

If the polluters are FRMSs ([Decressin et al., 2007](#)), the rotationally induced mixing of massive MS stars ( $\sim 15 M_{\odot}$ ) is used as enrichment mechanism, bringing up the material from the core of the star, i.e. where hot hydrogen burning occurs, to the stellar surface. This scenario still suffers from the dilution problem mentioned above. However, a more recent version of the model, developed by [Krause et al. \(2013\)](#), envisions a case where the GC does not have time to expel the original gas (including SNe) before  $\sim 20$  Myr, thus reducing the dilution issue. Another way of bringing up material from the core is via binary interactions. The interacting massive binaries (IBs) model ([de Mink et al., 2009](#)) is very similar to the FRMS, except that the sources of enrichment are massive binaries, of 20 and  $15 M_{\odot}$ . Nevertheless, both these scenarios, i.e. FRMSs and IBs, still suffer from the mass budget problem as the other self-enrichment models.

An alternative scenario for the origin of MPs that is not based on multiple generations is the one put forward by [Bastian et al. \(2013b\)](#). Interacting massive binaries and FRMSs shed processed material onto low mass pre-main sequence stars generating an accretion disc. Such low-mass stars then sweep up the processed material through their accretion disc onto the young stars as they pass through the cluster core. This model does not require clusters to be more massive at birth and it is consistent with observations of YMCs being gas-free after the first few Myrs (i.e. no age spreads, [Cabrera-Ziri et al. 2015; Hollyhead et al. 2015](#)). However, it has been shown that the main drawback is that the process of sweeping up material with no angular momentum causes the disc to rapidly dissolve and become accreted by the host star. Without an accretion disc, the star is not able to accrete (or sweep up) the processed material as

Bondi-Hoyle accretion is much too inefficient ([Wijnen et al., 2016](#)).

A recent scenario that is able to reproduce many MPs observational evidence is the one that envisions super massive stars (SMSs,  $M > 10^3 M_{\odot}$ ) as the polluter source for the enrichment ([Gieles et al., 2018](#)). The authors show that, through adiabatic contraction, the newly formed proto-cluster can undergo intense gas accretion to increase the stellar collision rate and form a SMS. After less than  $\sim 3$  Myr, a new generation of stars forms, polluted from a mix of the SMS stellar wind and gas with pristine composition, i.e. the same abundance as the initial stars that formed in the clusters. This is consistent with observations from YMCs and it does not suffer from the mass budget problem. Additionally, it predicts a linear relation between the mass of the SMS and the mass of the cluster such that scaling relations among chemical spreads and cluster mass are naturally reproduced (see next Section for more details on this §1.6). One of the main drawbacks of such scenario is that the existence of such super massive stars is still just speculation, and it is not clear if the model can reproduce the observed discrete abundance patterns in GCs.

Many other different models have been proposed for the origin of MPs, thus we refer the interested reader to e.g. [Bastian & Lardo \(2018\)](#) for more details. However, the cause for their origin is still under debate (e.g., [D'Antona et al. 2014](#); [Bastian, Cabrera-Ziri & Salaris 2015](#)). This represents the second open question my thesis work focused upon: how do chemical anomalies in GCs form? And how can we use young massive clusters to place constraints on MPs scenarios?

## 1.6 What controls the origin of multiple populations?

A promising line of investigation so far has been to determine whether MPs are found according to certain properties of the cluster.

The presence of MPs in GCs appears to be nearly ubiquitous in the most nearby galaxies in ancient and massive GCs (e.g. [Renzini et al. 2015](#)). Large numbers of MW GCs have been studied (e.g. [Gratton, Carretta & Bragaglia 2012](#)) and basically all old

( $> 10$  Gyr) clusters surveyed so far have been found to host MPs. The absence of light-element variations was suggested in a handful of massive and old Galactic GCs (e.g., [Walker et al. 2011](#); [Villanova et al. 2013](#)). However, recent detailed studies have demonstrated that MPs are indeed present also in these systems (see for example the cases of IC 4499 and Rup 106; [Dalessandro et al. 2018](#); [Dotter et al. 2018](#)).

Chemical anomalies are also found in ancient and massive clusters in the Fornax dwarf galaxy ([Larsen et al., 2014a](#)), the Sagittarius dwarf galaxy ([Carretta et al., 2014](#)), the WLM dwarf galaxy ([Larsen et al., 2014b](#)), M31 (e.g. [Schiavon et al. 2013](#)), and in the Magellanic Clouds (MCs, e.g. [Mucciarelli et al. 2009](#); [Dalessandro et al. 2016](#); [Niederhofer et al. 2017b](#); [Gilligan et al. 2019](#)). Until recently, MPs were believed to be found only in massive, old clusters, while none were present neither in clusters of comparable age and lower masses (e.g., E3, [Salinas & Strader 2015](#)), nor in OCs (e.g., [Bragaglia et al. 2012](#)). Such evidence led many to consider cluster mass as the key cluster property controlling the presence of MPs. Cluster mass is indeed a fundamental parameter in the onset of MPs: [Carretta et al. \(2010\)](#) found that the extent of the Na spread in a GC correlates positively with the present-day mass of the cluster, i.e. more massive clusters exhibit larger Na spreads. Strong positive correlations are also observed between cluster mass and N spreads ([Schiavon et al., 2013](#)), He spreads ([Milone et al., 2018](#)) and fraction of anomalous stars ([Milone et al., 2017](#)). These are shown in Fig. 1.8. Such correlations are also another argument against high GC mass loss, as more massive clusters, i.e. able to retain more stars, should have lost less FP stars and showed lower fractions of anomalous SP stars (see §1.5).

The discovery of relatively young ( $\sim 1 - 2$  Gyr old), but still massive ( $\sim 2 \times 10^5$   $M_\odot$ ) clusters with no abundance spreads within them ([Mucciarelli et al. 2008, 2014](#), [Colucci et al. 2012](#)) challenged the idea that cluster mass was the key factor regulating the appearance of MPs. In addition to this, [Mucciarelli et al. \(2011\)](#) analysed the spectra of RGB stars in NGC 1866, a very young ( $\sim 200$  Myr) and massive ( $\sim 1 \times 10^5$   $M_\odot$ ) cluster, finding no evidence for MPs. These were complemented with integrated light studies of YMCs younger than 100 Myr but very massive ( $\sim 10^6 M_\odot$ ), where no chemical anomalies were found ([Cabrera-Ziri et al., 2016b](#); [Lardo et al., 2017](#)). Such

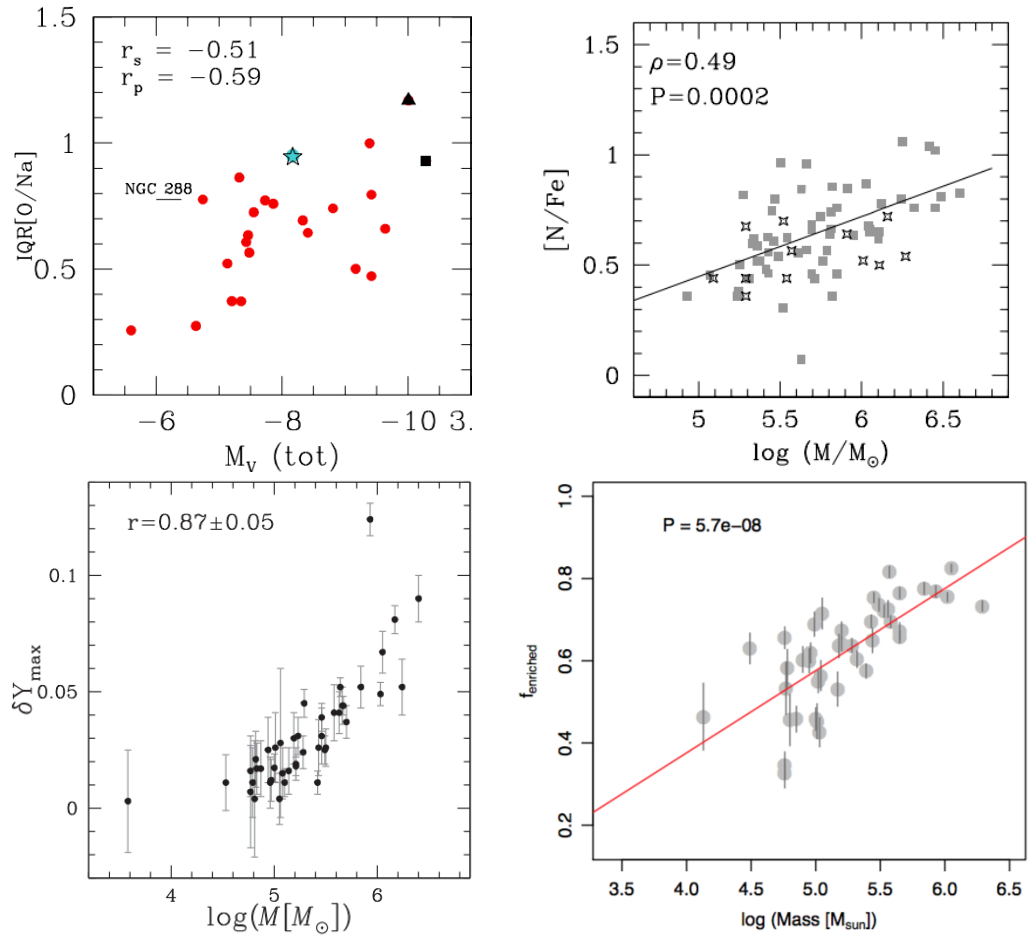


Figure 1.8: Correlation between cluster mass and Na spreads (top left, from Carretta et al. 2014), N spreads (top right, from Schiavon et al. 2013), He spreads (bottom left, Milone et al. 2018), fraction of SP stars over the total (bottom right, Bastian & Lardo 2018, after Milone et al. 2017) for various samples of Galactic GCs.

findings have opened a new question about whether cluster age could be considered as a relevant factor for the existence of MPs, in addition to mass. It has even been proposed that the ancient GCs are intrinsically different to the young clusters with similar masses, as only ancient GCs had been found to host MPs ([Carretta et al., 2010](#)).

Studying MPs in young star clusters is fundamental to put fresh constraints on any scenario proposed for the origin of MPs. Understanding whether these types of objects share the same stellar populations is also crucial to establish whether we can consider young star clusters as the same objects as ancient GCs. Without a working theory for how MPs are created, GC formation theory is still incomplete, which also has consequences for galactic formation theory as populations of stars with similar abundance patterns have also been identified in the bulge of the Milky Way ([Schiavon et al., 2017](#)).

Throughout this thesis, I present the global results from our HST photometric survey, which consists in HST UV observations of 13 star clusters in the Magellanic Clouds (Chaper §2). All clusters have masses comparable to those of the old GCs where MPs have been identified, but with significantly younger ages (spanning from  $\sim 1.5$  up to  $\sim 11$  Gyr). The main goal of the survey is to test whether MPs are exclusively found in ancient GCs, and hence, to shed light on the physical property that controls the onset of MPs. It is crucial to understand whether YMCs are the same type of stellar systems as the ancient GCs, just observed at a different stage of their lifetimes. If confirmed, this could provide important constraints on star cluster and MP formation studies. Furthermore, exploring clusters at younger ages is useful to address the fundamental question whether the star (and cluster) formation conditions were different in the early Universe.

## 1.7 Summary

In this introductory chapter I reported the background and motivation that led to my thesis work. One of the main open problem in astronomy is understanding how globular clusters form. Globular clusters are fascinating objects for many reasons (§1.1) and uncovering clues on their formation and evolution is fundamental, especially as they

represent a bridge connecting the small scale of star formation to the larger scale of galaxy formation.

It is now well known that we do not observe only globular clusters (ancient, massive, §1.1) in the local Universe. Young, massive clusters are found forming in every local environment (§1.2), where the star formation rate is high enough. Such a discovery led many to question whether such two classes of objects, that share similar properties, are the same, only observed at different times of their lives. However, globular clusters also show very specific stellar populations, i.e. chemical abundance variations, that are not observed in field stars at the same metallicity (§1.3) nor in the open clusters, less massive and less dense star clusters typically observed in the disk of the Milky Way. The origin of such multiple stellar populations is still debated in the literature (§1.5). The main open questions my thesis work focused upon are: (i) how do multiple populations form? what is the origin of multiple populations based on? and (ii) are young massive clusters the same as ancient globular clusters? can we use young massive clusters to set new constraints on the multiple populations phenomenon?

To attempt to answer to such questions, we searched for multiple populations in massive young and intermediate age clusters, through a joint photometric HST and spectroscopic ESO VLT/FORS2 survey. This allowed to explore and characterise the stellar populations of star clusters that are significantly younger than the ancient globular clusters. It also allowed us to investigate the role of cluster age in the onset of multiple populations for the first time (Chapters 3, 5). Additionally, thanks to the youth of the clusters in our sample, it was possible to put the tightest constraints on multiple populations models to date (see Chapter 4,5).

# Chapter 2

## No evidence for multiple populations in the SMC cluster NGC 419

In this chapter I present the first results obtained on the massive star cluster NGC 419, aged  $\sim 1.5$  Gyr old and located in the SMC. First, I outline the HST photometric survey in §2.1. Then, in §2.2, I report the details of the photometric data reduction and observational techniques, as well as models for the chemical abundances that will be used for comparison with the observations (§2.2.4). I present the results in §2.3 and discuss in §2.4. This Chapter is based on the work published in [Martocchia et al. \(2017\)](#).

### 2.1 The HST survey

The photometric data presented in this thesis are from the *Hubble Space Telescope* survey GO-14069 and GO-15062 (P.I. N. Bastian, [Niederhofer et al. 2017b](#); [Martocchia et al. 2019](#)). The sample is composed by 13 star clusters both in the LMC and SMC. The imaged clusters have masses greater than a few times  $10^4 M_\odot$ , such that they are comparable to the masses of Galactic GCs that show MPs. Additionally, the clusters in our sample span a wide range of ages, from  $\sim 1.5$  Gyr up to  $\sim 11$  Gyr. Indeed, the goal of the survey is to answer the question whether there is an age limit on the presence of

chemical variations in GCs. In Table 2.3 we list the name of the clusters, along with their literature ages and masses.

New observations were provided in the narrow band UV filter  $F343N$  of the WFC3/UVIS instrument, and in some cases the wide band UV and optical filters  $F336W$  and  $F438W$  were added. We always complemented our analysis with archival observations in the optical  $F555W$  and  $F814W$  filters of the ACS/WFC or WFPC2/HST, while in a few cases the  $F336W$  and  $F438W$  images were also already available in the archive. Tables 2.1 and 2.2 reports the log of the HST observations used throughout this thesis.

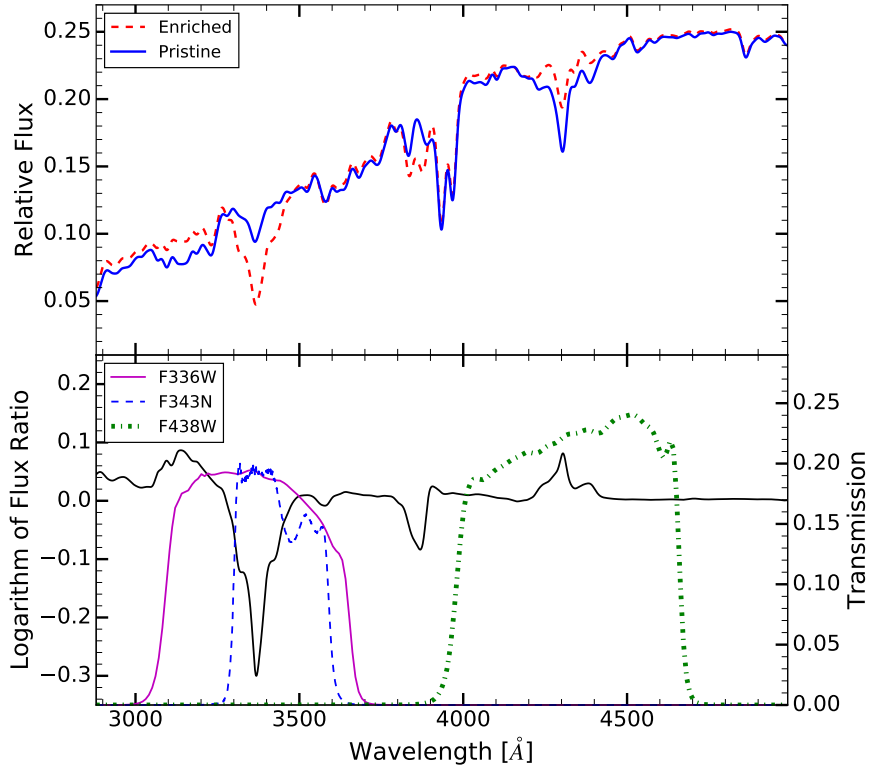


Figure 2.1: *Upper Panel:* Model spectra of a typical RGB star in a 10 Gyr old population, with an effective temperature  $T_{\text{eff}} = 5220$  K, surface gravity  $\log(g) = 2.71$  dex, and metallicity  $[\text{Fe}/\text{H}] = -1.5$  dex. The blue solid curve represents a star with primordial composition; the red dashed line indicates the spectrum of an anomalous star, enriched in N. *Lower Panel:* Logarithmic ratio of the fluxes of the enriched and the primordial star (black solid line) along with the transmission curves of the  $F336W$  (purple solid line),  $F343N$  (blue dashed line) and  $F438W$  (green dash-dotted line) filters. Figure from Niederhofer et al. (2017b).

As discussed in §1.3.1, the UV/optical filters are extremely useful when searching for MPs. The upper panel of Figure 2.1 shows model spectra of a typical RGB star

in a 10 Gyr old population with a metallicity [Fe/H] of  $-1.5$  dex from Niederhofer et al. (2017b). The blue spectrum represents a FP star, i.e. with primordial abundance composition. The red dashed curve indicates the spectrum of a SP star, i.e. enriched in N and Na and depleted in C and O. The model spectra were obtained by using the ATLAS12 and SYNTHE model atmosphere and spectral synthesis codes (Sbordone et al., 2004; Kurucz, 2005).

The enriched model is enhanced in N by 1.8 dex and in Na by 0.8 dex and depleted in O by 0.8 dex and in C by 0.6 dex, with respect to the primordial composition. This is a typical enrichment found for Galactic GCs. The lower panel of Fig. 2.1 shows the flux ratio of the second and first population star as a black line, along with the transmission curves<sup>1</sup> of the  $F336W$ ,  $F343N$ , and  $F438W$  filters. Strong NH absorption lines, namely at  $\sim 3370\text{\AA}$  are present inside the  $F336W$  and  $F343N$  filter bands, while the  $F438W$  passband includes CH absorption features at  $\sim 4300\text{\AA}$ . This will result in a drop and an increase of the flux ratio at these wavelengths, respectively. Therefore, combinations of such filters will mark a clear distinction between FP stars (primordial) and SP stars (N rich, C poor) in the CMD.

Niederhofer et al. (2017b,a) analysed the clusters in the age range 6–10 Gyr, namely NGC 121, NGC 416, NGC 339, Lindsay 1. They found MPs in such clusters, by looking at the width of the RGB in UV colours combination, which is a signature of N enhancement. For the first time, MPs were found in massive star clusters down to an age of  $\sim 6$  Gyr (which corresponds to a redshift of formation  $z = 0.75$ ).

In the next Sections and Chapters, I report on the data reduction, analysis of the younger clusters in the sample as well as results from the whole survey.

---

<sup>1</sup>[http://www.stsci.edu/hst/wfc3/ins\\_performance/throughputs/Throughput\\_Tables](http://www.stsci.edu/hst/wfc3/ins_performance/throughputs/Throughput_Tables)

Table 2.1: Log of the HST observations (part 1).

Cluster Name	GO	Camera	Filter	N × exp. time	P.I.
NGC 121	13435	WFC3/UVIS	F336W	4×1061 s	M. Monelli
	13435	WFC3/UVIS	F438W	4×200 s	M. Monelli
	13435	WFC3/UVIS	F814W	2×100 s	M. Monelli
	14069	WFC3/UVIS	F343N	1650, 800, 600 s	N. Bastian
	10396	ACS/WFC	F555W	4×496 s, 2×20 s	J. Gallagher
	10396	ACS/WFC	F814W	4×474 s, 2×10 s	J. Gallagher
	14069	WFC3/UVIS	F336W	3×967 s	N. Bastian
	14069	WFC3/UVIS	F343N	4×1200 s	N. Bastian
	14069	WFC3/UVIS	F438W	3×347 s	N. Bastian
	10396	ACS/WFC	F555W	4×496 s, 2×20 s	J. Gallagher
Lindsay 1	10396	ACS/WFC	F814W	4×474 s, 2×10 s	J. Gallagher
	14069	WFC3/UVIS	F336W	3×1020 s	N. Bastian
	14069	WFC3/UVIS	F343N	3×1535 s	N. Bastian
	14069	WFC3/UVIS	F438W	3×375 s	N. Bastian
	10396	ACS/WFC	F555W	4×1200 s, 2×70 s	J. Gallagher
NGC 416	10396	ACS/WFC	F814W	4×1036 s, 2×40 s	J. Gallagher
	14069	WFC3/UVIS	F336W	3×1020 s	N. Bastian
	14069	WFC3/UVIS	F343N	3×1535 s	N. Bastian
	14069	WFC3/UVIS	F438W	3×375 s	N. Bastian
	10396	ACS/WFC	F555W	4×1200 s, 2×70 s	J. Gallagher
NGC 339	10396	ACS/WFC	F814W	4×1036 s, 2×40 s	J. Gallagher
	14069	WFC3/UVIS	F336W	3×1020 s	N. Bastian
	14069	WFC3/UVIS	F343N	4×1055 s	N. Bastian
	14069	WFC3/UVIS	F438W	4×380 s	N. Bastian
	10396	ACS/WFC	F555W	4×1984 s, 2×40 s	J. Gallagher
NGC 1978	10396	ACS/WFC	F814W	4×1896 s, 2×20 s	J. Gallagher
	14069	WFC3/UVIS	F336W	3×1580 s	N. Bastian
	14069	WFC3/UVIS	F343N	6×3975 s	N. Bastian
	14069	WFC3/UVIS	F438W	6×2475 s	N. Bastian
	9891	ACS/WFC	F555W	300 s	G. Gilmore
NGC 419	9891	ACS/WFC	F814W	200 s	G. Gilmore
	12257	WFC3/UVIS	F336W	5×3230	L. Girardi
	14069	WFC3/UVIS	F343N	4×4575 s	N. Bastian
	14069	WFC3/UVIS	F438W	4×1120 s	N. Bastian
	10396	ACS/WFC	F555W	4×1200 s, 2×70 s	J. Gallagher
NGC 1806	10396	ACS/WFC	F814W	4×1036 s, 2×40 s	J. Gallagher
	12257	WFC3/UVIS	F336W	5×3580	L. Girardi
	14069	WFC3/UVIS	F343N	3×2945 s	N. Bastian
	10595	ACS/WFC	F435W	2×680 s, 1×90 s	P. Goudfrooij
	10595	ACS/WFC	F555W	2×680 s, 1×40 s	P. Goudfrooij
NGC 1846	10595	ACS/WFC	F814W	2×680 s, 1×8 s	P. Goudfrooij
	12219	WFC3/UVIS	F336W	9×1017 s	A. Milone
	14069	WFC3/UVIS	F343N	3×2945 s	N. Bastian
	10595	ACS/WFC	F435W	2×680 s, 1×90 s	P. Goudfrooij
	10595	ACS/WFC	F555W	2×680 s, 1×40 s	P. Goudfrooij
NGC 1783	10595	ACS/WFC	F814W	2×680 s, 1×8 s	P. Goudfrooij
	12257	WFC3/UVIS	F336W	5×3580	L. Girardi
	14069	WFC3/UVIS	F343N	3×2945 s	N. Bastian
	10595	ACS/WFC	F435W	2×680 s, 1×90 s	P. Goudfrooij
	10595	ACS/WFC	F555W	2×680 s, 1×40 s	P. Goudfrooij
	10595	ACS/WFC	F814W	2×680 s, 1×8 s	P. Goudfrooij

Table 2.2: Log of the HST observations (part 2).

Cluster Name	GO	Camera	Filter	N × exp. time	P.I.
NGC 2121	15062	WFC3/UVIS	F336W	2×715 s, 270 s	N. Bastian
	15062	WFC3/UVIS	F343N	2×1060 s, 540 s	N. Bastian
	15062	WFC3/UVIS	F438W	2×550 s, 120 s	N. Bastian
	8141	WFPC2	F555W	4×400 s	R. Rich
	8141	WFPC2	F814W	4×400 s	R. Rich
NGC 2155	15062	WFC3/UVIS	F336W	2×705 s, 250 s	N. Bastian
	15062	WFC3/UVIS	F343N	2×1060 s, 530 s	N. Bastian
	15062	WFC3/UVIS	F438W	2×545 s, 120 s	N. Bastian
	5475	WFPC2	F450W	230 s	M. Shara
	5475	WFPC2	F555W	120 s	M. Shara
Lindsay 38	15062	WFC3/UVIS	F336W	2×710 s, 268 s	N. Bastian
	15062	WFC3/UVIS	F343N	2×1057 s, 515 s	N. Bastian
	15062	WFC3/UVIS	F438W	2×538 s, 123 s	N. Bastian
	10396	ACS/WFC	F555W	4×485 s, 2×20 s	J. Gallagher
	10396	ACS/WFC	F814W	4×463 s, 2×10 s	J. Gallagher
Lindsay 113	15062	WFC3/UVIS	F336W	2×720 s, 274 s	N. Bastian
	15062	WFC3/UVIS	F343N	2×1065 s, 530 s	N. Bastian
	15062	WFC3/UVIS	F438W	2×545 s, 128 s	N. Bastian
	9891	ACS/WFC	F555W	480 s	G. Gilmore
	9891	ACS/WFC	F814W	290 s	G. Gilmore

Table 2.3: List of clusters in the HST survey with information on the galaxy, age and mass and respective references.

Cluster Name	Galaxy	Age (Gyr)	Ref.	Mass ( $\times 10^5 M_\odot$ )	Ref.
NGC 419	SMC	1.2-1.6	(1)	2.4	(2)
NGC 1783	LMC	1.75	(2)	2.6	(2)
NGC 1806	LMC	1.70	(2)	1.3	(2)
NGC 1846	LMC	1.75	(2)	1.7	(2)
NGC 1978	LMC	2	(3)	2-4	(6)
NGC 2121	LMC	2.5	(4)	1	(7)
NGC 2155	LMC	2.5	(4)	0.36	(7)
Lindsay 113	SMC	4.5	(4)	0.23	(8)
Lindsay 38	SMC	6.5	(4)	0.15	(9)
NGC 416	SMC	6.0	(1)	1.6	(7)
NGC 339	SMC	6.0	(1)	0.8	(7)
Lindsay 1	SMC	7.5	(1)	2.0	(9)
NGC 121	SMC	10.5	(5)	3.7	(7)

(1) Glatt et al. (2008b); (2) Goudfrooij et al. (2014); (3) Mucciarelli et al. (2007);

(4) Martocchia et al. (2019); (5) Glatt et al. (2008a); (6) Krause et al. (2016);

(7) McLaughlin &amp; van der Marel (2005); (8) Chantereau et al. (2019); (9) Glatt et al. (2011);

## 2.2 Observational techniques and models

### 2.2.1 Observations and Data Reduction

The photometric analysis has been performed following the same strategy as in [Dalessandro et al. \(2014, 2018\)](#). Briefly, we used DAOPHOTIV ([Stetson, 1987](#)) independently on each camera and each chip. We selected several hundreds of bright and isolated stars in order to model the point-spread function (PSF). All available analytic functions were considered for the PSF fitting (Gauss, Moffat, Lorentz and Penny functions), leaving the PSF free to spatially vary to the first-order. In each image, we then fit all the star-like sources detected at  $3\sigma$  from the local background with the best-fit PSF model by using ALLSTAR. We then created a master catalogue composed of stars detected in  $(n/2 + 1)$  images for each cluster<sup>2</sup>. At the corresponding positions of stars in this final master-list, a fit was forced with DAOPHOT/ALLFRAME ([Stetson, 1994](#)) in each frame. For each star thus recovered, multiple magnitude estimates obtained in each chip were homogenised by using DAOMATCH and DAOMASTER, and their weighted mean and standard deviation were finally adopted as star magnitude and photometric error. The final result consists in a catalogue for each camera<sup>3</sup>.

Instrumental magnitudes have been converted to the VEGAMAG photometric system by using the prescriptions and zero-points reported on the dedicated HST web-pages<sup>4</sup>. Instrumental coordinates were reported on the absolute image World Coordinate System by using CataXcorr<sup>5</sup>. The WFC3 catalogue was combined with the ACS (or WFPC2) by using the same CataXcorr and CataComb.

Each catalogue was field-star subtracted and corrected for differential reddening. I will

---

<sup>2</sup>Where the number of exposures in the same filter is equal to three, we used stars detected in 2 images to create the catalogues.

<sup>3</sup>As an additional check we repeated the photometric analysis by using a third-order spatial variation for the PSF. However, we decided to perform the analysis on the catalogues where the PSF was left free to spatially vary to the first-order. No significant changes were detected between the two catalogues.

<sup>4</sup>see [http://www.stsci.edu/hst/wfc3/phot\\_zp\\_lbn](http://www.stsci.edu/hst/wfc3/phot_zp_lbn) and <http://www.stsci.edu/hst/acs/analysis/zeropoints>

<sup>5</sup>Part of a package of astronomical softwares (CataPack) developed by P. Montegriffo at INAF-OABo.

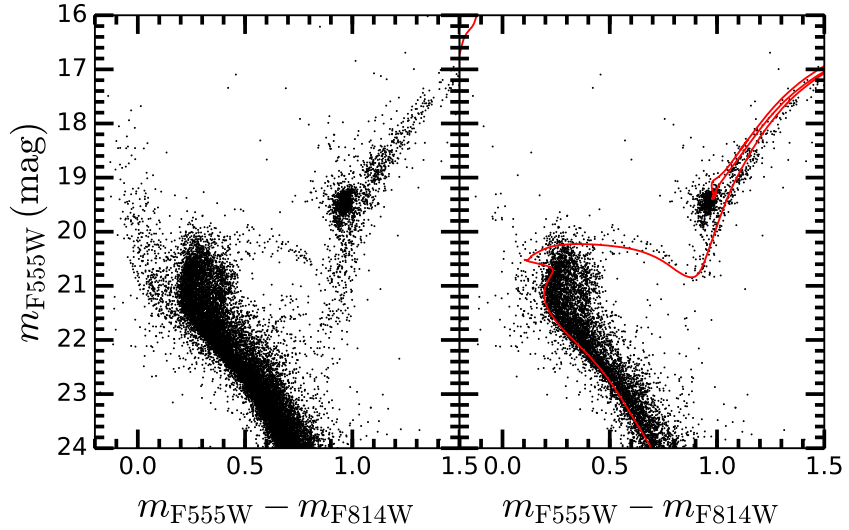


Figure 2.2:  $m_{\text{F}555\text{W}} - m_{\text{F}814\text{W}}$  vs.  $m_{\text{F}555\text{W}}$  CMD of NGC 419 before (left) and after (right) the field star subtraction. The red curve in the right panel indicates the MIST isochrone we adopted for values of age (1.4 Gyr), metallicity  $[\text{Fe}/\text{H}] = -0.7$ ; distance modulus  $M - m = 18.85$ ; extinction value  $E(B - V) = 0.05$ .

generally report the methods used in §2.2.2 and §2.2.3, respectively. Particular cases will be discussed throughout the manuscript.

### 2.2.2 Field stars subtraction

Member stars are selected according to a statistical method of field star subtraction. First, a cluster region is defined. Then, we defined a background reference region having the same area as the cluster region in order to statistically subtract field stars from the cluster CMD in  $m_{\text{F}336\text{W}} - m_{\text{F}438\text{W}}$  vs.  $m_{\text{F}438\text{W}}$  space. We removed the closest star in colour-magnitude space in the cluster region, for each star in the background region.

Fig. 2.2 shows the  $m_{\text{F}555\text{W}} - m_{\text{F}814\text{W}}$  vs.  $m_{\text{F}555\text{W}}$  CMDs of NGC 419, before (left panel) and after (right panel) the field star subtraction.

### 2.2.3 Differential reddening correction

We also investigated possible effects of differential reddening (DR) on the CMDs. We corrected the photometry of all the clusters for DR following the method described in Milone et al. (2012) and using the extinction coefficients reported in Milone et al. (2015). The DR method looks for systematic scatter of stars along the MS, i.e. if neighbours stars in the Ra-Dec plane are systematically scattered along the extinction vector in the CMD. A part of the MS, below the turn-off, is selected and the CMD ( $m_{F555W} - m_{F814W}$  vs  $m_{F814W}$  CMD in this case) is rotated along the extinction vector, such that the final CMD is parallel to the extinction vector. Then, the selected part of the MS is verticalised with a fiducial line and the horizontal displacement from this line is computed for each star. For every star on the verticalised MS, the median horizontal displacement of a certain number of its closest neighbours is calculated. The Ra-Dec plane is divided into grid cells and the median displacement in the grid cells is computed. Finally all the stars are corrected for the reddening value in their respective grid cell.

The average change in colour due to differential extinction in both  $m_{F336W} - m_{F438W}$  and  $m_{F343N} - m_{F438W}$  colours results to be very low for all clusters, i.e.  $< 0.01$ , with a mean maximum  $A_{F336W} \sim 0.02$ . We conclude that reddening effects are negligible and do not affect our results.

### 2.2.4 Models for the chemical anomalies

In this Section, I report on how stellar evolution models with different chemical compositions were calculated, in order to compare them with our observations. Models were developed by C. Usher.

We compared MIST isochrones (Dotter, 2016; Choi et al., 2016) to our data to obtain an estimate of age, metallicity, distance modulus ( $M - m$ ) and extinction values and thus to provide input parameters for the model atmospheres. We assumed a distance modulus of  $M - m = 18.85$  for NGC 419. Extinction values were computed via the

following:  $A_{\text{F}336\text{W}} = 1.64 A_V$ ,  $A_{\text{F}343\text{N}} = 1.64 A_V$ ,  $A_{\text{F}438\text{W}} = 1.35 A_V$ ,  $A_{\text{F}555\text{W}} = 1.055 A_V$ ,  $A_{\text{F}814\text{W}} = 0.586 A_V$  ([Milone et al. 2015](#); [Goudfrooij et al. 2009](#)).

We calculated synthetic photometry from model atmospheres with different abundance patterns. The 1-D MIST models include a range of physics including diffusion on the MS, rotation in stars more massive than  $1.2 M_\odot$  convection including thermohaline and rotational mixing. We used ATLAS12 ([Kurucz, 1970, 2005](#)) to calculate model atmospheres and SYNTHE ([Kurucz & Furenlid 1979](#); [Kurucz & Avrett 1981](#)) to synthesize spectra. These models are one-dimensional, static and plane parallel and assume local thermodynamic equilibrium. We used the same versions of the models used by [Sbordone et al. \(2004\)](#) and line lists for the atomic data as [Larsen, Strader & Brodie \(2012a\)](#) and [Larsen et al. \(2014a\)](#) who we refer to for further details of our stellar atmosphere calculations. We also used the same PYTHON wrappers to ATLAS12 and SYNTHE as used by [Larsen, Strader & Brodie \(2012a\)](#). For our stellar atmosphere calculations we adopted the [Asplund et al. \(2009\)](#) solar abundances which are the same as adopted by the MIST models. For each set of models, we calculated 57 model spectra between  $0.7 M_\odot$  on the MS and the tip of the RGB. We selected the input masses to calculate model atmospheres by eye in log  $L$ -log  $T_{\text{eff}}$  space with denser sampling during stellar evolutionary phases such as the MSTO and the base of the RGB where the isochrone displays greater curvature.

We calculated the models using several chemical mixtures. First, we calculated a set of scaled solar models ( $[\text{C}/\text{Fe}] = [\text{N}/\text{Fe}] = [\text{O}/\text{Fe}] = 0$ ). Next, we calculated a set of intermediate N-enhancement models with  $[\text{C}/\text{Fe}] = [\text{O}/\text{Fe}] = -0.1$  and  $[\text{N}/\text{Fe}] = +0.5$ . Additionally, we calculated a set of enriched N-enhancement models with  $[\text{C}/\text{Fe}] = [\text{O}/\text{Fe}] = -0.6$  and  $[\text{N}/\text{Fe}] = +1.0$ . Lastly, we calculated a set of models with slightly less degree of N-enhancement but with solar C and O abundances ( $[\text{C}/\text{Fe}] = [\text{O}/\text{Fe}] = 0$  and  $[\text{N}/\text{Fe}] = +0.3$  dex), in order to check degeneracies between C depletion and N enhancement. For the enhanced models, the C and O abundances were chosen to keep the  $[(\text{C}+\text{N}+\text{O})/\text{Fe}]$  the same between the models, according to what we observe in standard GCs ([Brown, Wallerstein & Oke 1991](#); [Cohen & Meléndez 2005](#); [Yong, Grundahl & Norris 2015](#); [Marino et al. 2016](#)). For each of these chemical mixtures we

kept the helium abundance (surface  $Y = 0.248$ ) constant and all other abundances fixed at solar. We assumed that the model atmospheres had the same chemical abundances at all stellar evolutionary stages.

To produce synthetic magnitudes, we integrated our model spectra over the filter transmission curves for WFC3<sup>6</sup> and ACS/WFC<sup>7</sup>. We then used the zeropoints provided on each instrument’s website to calculate Vega magnitudes. We find very good agreement ( $< 0.01$  mag difference) between our scaled solar models and the photometry calculated by Choi et al. (2016).

We then used the synthetic magnitudes to find a suitable combination of colours for revealing the presence of chemical enhancement on the RGB of NGC 419 (and the younger clusters). After trying several filters, we found out that using a filter combination of the form  $(F336W - F438W) - (F438W - F814W) = C_{F336W,F438W,F814W}$   $\equiv$  CUBI for the wide band F336W and  $(F343N - F438W) - (F438W - F814W) = C_{F343N,F438W,F814W}$   $\equiv$  CUnBI for the narrow band F343N, appeared to be the most effective way to prove whether NGC 419 showed MPs. Monelli et al. (2013) used a similar filter combination in order to detect the presence of MPs in a number of Galactic GCs, the  $C_{U,B,I} = (U - B) - (B - I)$  combination. They point out that this pseudo-colour is effective at unveiling multiple sequences and spreads in the RGB. The same colour (CUBI) has also recently been used by Dalessandro et al. (2016) to efficiently detect MPs in NGC 121. Accordingly, when comparing the expected spread in the RGB between the solar and intermediate models, as well as between the solar and enriched models, we obtained that  $\Delta(\text{CUnBI}) \simeq 2 \times \Delta(\text{CUBI})$ . This result is directly comparable with the data.

We also investigated possible effects of an enhanced He abundance on the RGB. Since the MIST isochrones are only available for one He abundance at a given metallicity, we used Padova isochrones (Bertelli et al., 2008) to perform our stellar atmosphere calculations. We assumed the same age and metallicity as obtained from MIST

---

<sup>6</sup>[http://www.stsci.edu/hst/wfc3/ins\\_performance/throughputs/Throughput\\_Tables](http://www.stsci.edu/hst/wfc3/ins_performance/throughputs/Throughput_Tables)

<sup>7</sup><http://www.stsci.edu/hst/acs/analysis/throughputs>

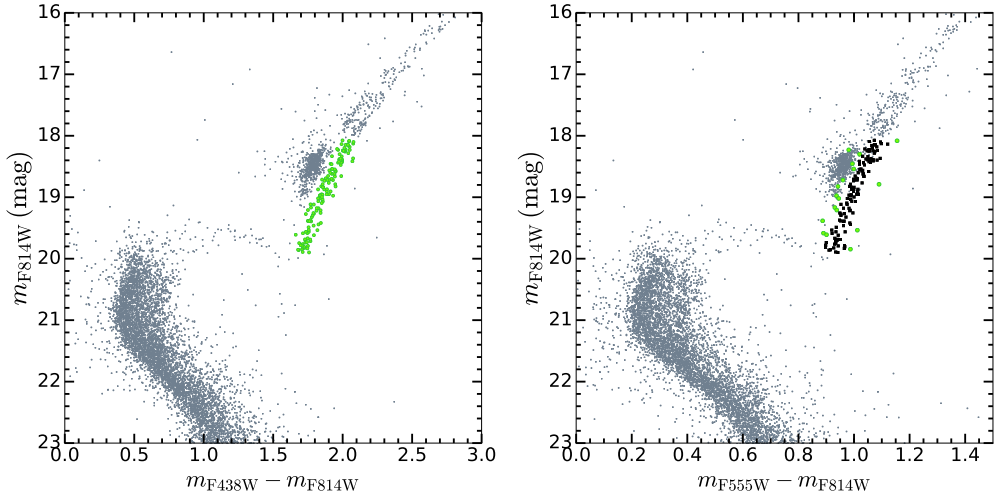


Figure 2.3: *Left panel:* CMD of NGC 419 using  $m_{\text{F}438\text{W}} - m_{\text{F}814\text{W}}$  vs. 1. Green filled circles mark the RGB stars selected in this colour and magnitude combination. *Right Panel:*  $m_{\text{F}555\text{W}} - m_{\text{F}814\text{W}}$  CMD of NGC 419. Black filled squares indicate the second selection of RGB stars in this colour-magnitude space, while green filled circles represent the stars passing the initial selection but not the second.

isochrones and two different He abundances, one with  $\text{Y} = 0.25$  and one with an enhanced  $\text{Y} = 0.30$ . Synthetic photometry was calculated as above, adopting the same solar and enriched chemical mixtures.

We obtained that the difference between the standard and enhanced He models in CUBI and CUnBI colours resulted to be  $\sim 0.01$ , in the same direction for both solar and enriched mixtures. Hence, these colours are not sensitive to He variations in the RGB and we did not account for enhanced He in our analysis.

## 2.3 Results

In order to search for the presence of multiple populations, we need to select a clean sample of RGB cluster members. To be as conservative as possible, we selected RGB stars in three different colour-magnitude spaces. This reduces the contamination by SMC field stars with ages  $\sim 1$  Gyr, comparable to the age of NGC 419. The first selection was made in  $m_{\text{F}438\text{W}} - m_{\text{F}814\text{W}}$  colours. Indeed, these colours are the best at separating the RGB from the AGB and the HB. Optical colours are much less affected

by sensitive star-to-star N variations than other colour combinations with a passband encompassing the NH and CN molecular features, i.e. the  $F336W$  and  $F343N$  filters (Sbordone et al. 2011). The left panel of Figure 2.3 shows the  $m_{F438W} - m_{F814W}$  vs.  $m_{F814W}$  CMD of NGC 419. Green filled circles mark the RGB stars selected in this filter combination. To avoid contamination by AGB stars, a brightness cut was applied ( $m_{F814W} > 18$ ). We then plotted these RGB stars on the  $m_{F555W} - m_{F814W}$  vs.  $m_{F814W}$  CMD of NGC 419. We noticed that several objects were scattered off the RGB or found to belong to the red clump, hence we made a second selection in  $m_{F555W} - m_{F814W}$  colours. The right panel of Fig. 2.3 shows the  $m_{F555W} - m_{F814W}$  vs.  $m_{F814W}$  CMD of NGC 419 with black filled squares indicating the second selection of RGB stars. Green filled circles mark the stars passing the first selection criterion but not the second.

We then plotted the second selection of RGB stars on the  $m_{F336W} - m_{F438W}$  vs.  $m_{F438W}$  CMD. Again, we found a very few objects which scattered off the RGB or on the tip of the MS (5 out of  $> 100$  stars). We made the final selection in  $m_{F336W} - m_{F438W}$  colours and this is shown in the left panel of Fig. 2.4, where the  $m_{F336W} - m_{F438W}$  vs.  $m_{F438W}$  CMD of NGC 419 is displayed. The right panel of Fig. 2.4 shows the CMD of NGC 419 using the narrow band filter F343N, in the  $m_{F343N} - m_{F438W}$  vs.  $m_{F438W}$  space. Red filled circles mark the final selected RGB stars in both panels of Fig. 2.4. Black filled squares represent the stars that did not pass the third selection. Interestingly, the RGB stars superimpose on the main sequence (MS) in these filters, emphasizing the importance of a selection in other colours such as  $m_{F438W} - m_{F814W}$  and  $m_{F555W} - m_{F814W}$ .

A first look at the  $m_{F336W} - m_{F438W}$  and  $m_{F343N} - m_{F438W}$  vs.  $m_{F438W}$  diagrams reveals that no splitting is detected in the RGB. The presence of multiple sequences and/or broadening in the RGB is a clear indication of the existence of two or more populations of stars, one with a primordial chemical composition, the others with a certain level of chemical enrichment (depleted in C and O and enhanced in N). Accordingly, we performed an analysis in order to quantify the observed spread in the UV/optical CMDs of NGC 419. More specifically, we analysed the differences between the spreads in the

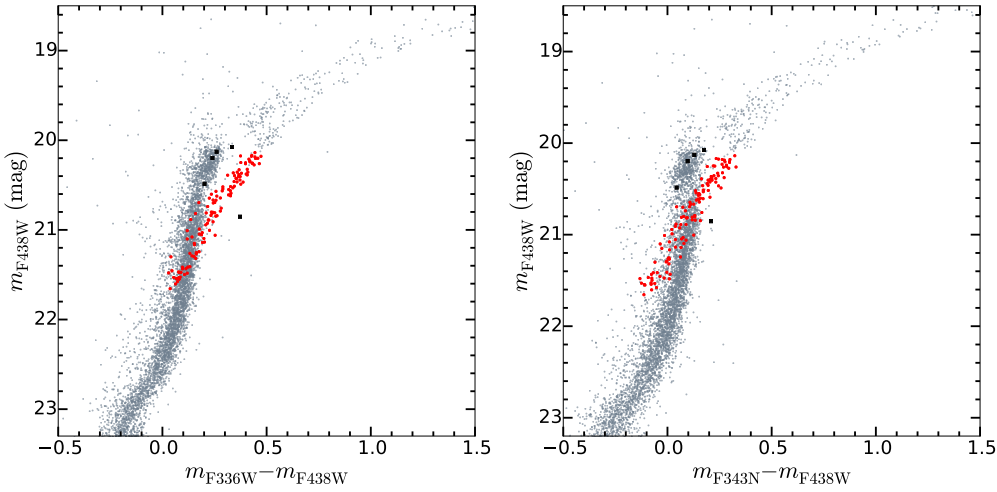


Figure 2.4:  $m_{F336W} - m_{F438W}$  vs.  $m_{F438W}$  CMD (left panel) and  $m_{F343N} - m_{F438W}$  vs.  $m_{F438W}$  CMD (right panel) of NGC 419. Red filled circles indicate the final RGB selected stars, while black filled squares represent the stars which did not pass the final selection.

two filters,  $F336W$  and  $F343N$ .

Then, we used CUBI and CUUnBI to effectively unveil multiple sequences and spreads in the RGB. The left panels of Figures 2.5 and 2.6 show the CMDs of NGC 419 using  $C_{F336W,F438W,F814W}$  vs.  $m_{F438W}$  and  $C_{F343N,F438W,F814W}$  vs.  $m_{F438W}$ , respectively. Orange and green circles indicate the selected RGB stars in the two different CMDs. No evidence of multiple sequences is seen in such filter combinations either. The right panels of Figures 2.5 and 2.6 show the histograms of the distributions in CUBI and CUUnBI colours of the RGB stars in NGC 419, respectively.

We calculated the mean and standard deviation ( $\sigma$ ) on unbinned colours (i.e.,  $C_{F336W,F438W,F814W}$  and  $C_{F343N,F438W,F814W}$ ) and derived a Gaussian PDF, indicated as a grey curve in the bottom panels of Fig. 2.5 and 2.6. The obtained  $\sigma$  values are  $\simeq 0.04$  for both filter combinations, with a difference of only  $\sim 2 \times 10^{-4}$ . We calculated the statistical error on  $\sigma$ . Using a bootstrap technique based on 10000 realisations, we found that  $\sigma_{\text{CUBI}} = 0.043 \pm 0.004$  and  $\sigma_{\text{CUUnBI}} = 0.043 \pm 0.003$ . As far as photometric errors are concerned, these are essentially the same in  $F336W$  and  $F343N$  filters in this bright regime. Therefore, we can say that errors are the same for both  $C_{F336W,F438W,F814W}$  and  $C_{F343N,F438W,F814W}$ . Hence, the observed RGB widths in  $C_{F336W,F438W,F814W}$  and  $C_{F343N,F438W,F814W}$  colours are directly com-

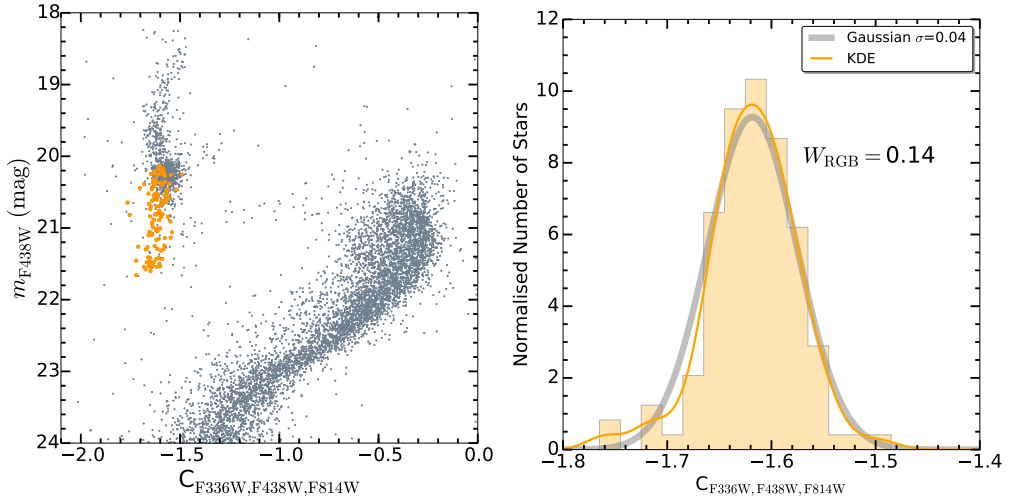


Figure 2.5: *Left Panel:*  $C_{F336W,F438W,F814W}$  vs.  $m_{F438W}$  CMD of NGC 419. Orange filled circles mark the selected RGB stars. *Right Panel:* histogram of the distribution of RGB stars in NGC 419, in  $C_{F336W,F438W,F814W}$  colours. The grey solid curve represents the Gaussian probability density function (PDF) with mean and standard deviation ( $\sigma$ ) calculated on unbinned data, while the orange solid curve indicates the KDE. Superimposed on the plot is the  $W_{\text{RGB}}$  index, see text for more details.

parable. In addition to this, the photometric errors in  $C_{F336W,F438W,F814W}$  and  $C_{F343N,F438W,F814W}$  colours are comparable to the observed spreads.

We derived the kernel density distribution (KDE) from a Gaussian kernel for both  $C_{F336W,F438W,F814W}$  and  $C_{F343N,F438W,F814W}$  colours. The results are superimposed on the histograms of data in the bottom panels of Fig. 2.5 and 2.6, as orange and green solid curves respectively. By visual inspection, we were unable to detect any significant difference between the gaussian and KDE distributions. The KDE did not reveal any bimodality or peaks that the gaussian could have smoothed out. Indeed, the dip test for unimodality (Hartigan & Hartigan 1985) confirms that there is no statistically significant bimodality in either the  $C_{F336W,F438W,F814W}$  or  $C_{F343N,F438W,F814W}$  distribution.

We also provided a different estimate for the RGB width. We defined the  $W_{\text{RGB}}$  index as the colour extension of the KDE at 20% of the distribution maximum. The values of  $W_{\text{RGB}}$  for  $C_{F336W,F438W,F814W}$  and  $C_{F343N,F438W,F814W}$  are given in the bottom panels of Figs. 2.5 and 2.6, respectively. We estimated the error on the  $W_{\text{RGB}}$  index using a Monte Carlo simulator technique. We obtained  $W_{\text{RGB}} = 0.139 \pm 0.013$  for  $C_{F336W,F438W,F814W}$  and  $W_{\text{RGB}} = 0.157 \pm 0.013$  for  $C_{F343N,F438W,F814W}$ . This con-

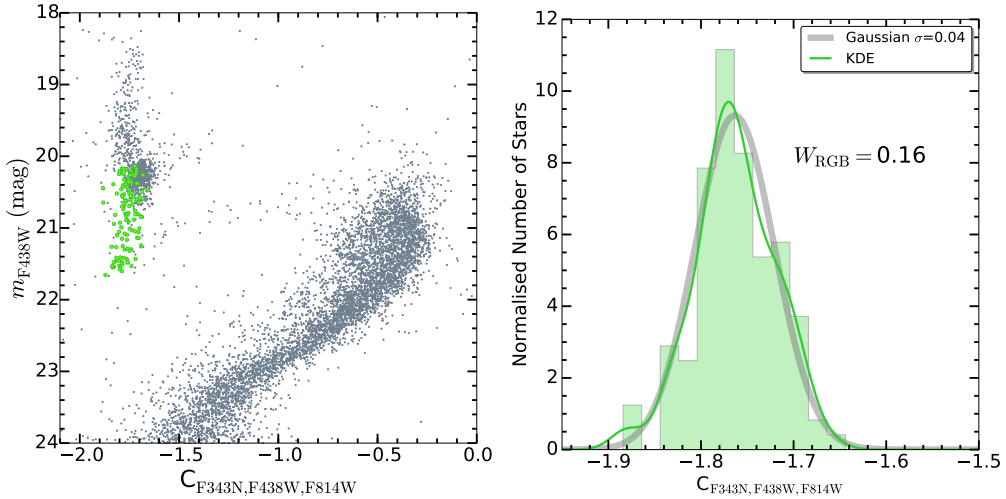


Figure 2.6: *Left Panel:*  $C_{F343N,F438W,F814W}$  vs.  $m_{F438W}$  CMD of NGC 419. Green filled circles mark the selected RGB stars. *Right Panel:* histogram of the distribution of RGB stars in NGC 419, in  $C_{F343N,F438W,F814W}$  colours. The grey solid curve represents the Gaussian probability density function (PDF) with mean and standard deviation ( $\sigma$ ) calculated on unbinned data, while the green solid curve indicates the KDE. Superimposed on the plot is the  $W_{\text{RGB}}$  index, see text for more details.

firms that the two widths are comparable, at  $\sim 1\sigma$  confidence level.

Synthetic spectra which take into account the presence of multiple population, i.e. the presence of enriched stars with respect to the primordial ones, predict a significant difference in the observed RGB spread when using the wide-band  $F336W$  filter with respect to the narrow-band  $F343N$  filter (see §2.2.4). More specifically, we observe that  $\sigma_{\text{CU}_{\text{nBI}}} \simeq \sigma_{\text{CUBI}} \simeq 0.04$  but we would have expected  $\sigma_{\text{CU}_{\text{nBI}}} \gtrsim 0.1$  if MPs were present. If the spreads are caused only by photometric errors, then we would expect  $\sigma_{\text{CUBI}} \simeq \sigma_{\text{CU}_{\text{nBI}}}$ , which is what we observe. No clear difference is detected in the observed spreads and  $W_{\text{RGB}}$  indices between  $C_{F336W,F438W,F814W}$  and  $C_{F343N,F438W,F814W}$  colours, hence we do not detect multiple populations in the RGB of NGC 419. We will discuss in detail these outcomes in the next Section, §2.3.1.

Finally, we also looked at observed spreads in the Red Clump (RC) and upper RGB (URGB). We performed the same analysis as for the RGB. We obtained that the widths are the same for  $C_{F336W,F438W,F814W}$  and  $C_{F343N,F438W,F814W}$  in the RC ( $W_{\text{RC}} \simeq 0.12$ ). We observe a slightly larger spread for  $C_{F343N,F438W,F814W}$  with respect to  $C_{F336W,F438W,F814W}$  in the URGB ( $W_{\text{URGB}}(\text{CUBI}) = 0.105 \pm 0.012$ ,  $W_{\text{URGB}}(\text{CU}_{\text{nBI}}) =$

$0.129 \pm 0.016$ ), although these are comparable at  $\sim 1\sigma$  level when taking the error into account.

### 2.3.1 Comparison with stellar models

We then compared our model colours (§2.2.4) to the data. Figures 2.7 shows the  $C_{F336W,F438W,F814W}$  vs.  $m_{F438W}$  and  $C_{F343N,F438W,F814W}$  vs.  $m_{F438W}$  CMDs of NGC 419, respectively, with three different models superimposed. The blue, green and red curves indicate isochrones for solar, intermediate and enriched abundance variations, respectively (see §2.2.4). Black circles indicate the selected RGB stars in both figures.

According to the models, a first look at Fig. 2.7 reveals that a difference in the spreads is expected if a chemical variation is present, either intermediate or enriched, between  $C_{F336W,F438W,F814W}$  and  $C_{F343N,F438W,F814W}$  colours. More specifically, we calculated the average spread between the solar and the enriched models in  $C_{F336W,F438W,F814W}$  colours and this results to be  $\simeq 0.079$ , while the average spread between these two models in  $C_{F343N,F438W,F814W}$  colours is  $\simeq 0.156^8$ . We then calculated the predicted spread in the RGB from the intermediate enrichment model. While the average spread in the RGB between the solar and the intermediate models in  $C_{F336W,F438W,F814W}$  colours results to be  $\simeq 0.033$ , the average one in  $C_{F343N,F438W,F814W}$  colours is about  $\simeq 0.064$ . Thus, according to the models, the colour spread of stars in the RGB in  $C_{F343N,F438W,F814W}$  colours is expected to be twice as broad as the spread in  $C_{F336W,F438W,F814W}$  colours, if an abundance pattern depleted in C and O and enhanced in N is present (either intermediate or enriched).

We compare here our predictions to the data. We have seen that the observed spread of RGB stars in both  $C_{F336W,F438W,F814W}$  and  $C_{F343N,F438W,F814W}$  colours results in  $\sigma_{\text{data}} \sim 0.04$  ( $\sigma_{\text{CUBI}} = 0.043 \pm 0.004$  and  $\sigma_{\text{CU}n\text{BI}} = 0.043 \pm 0.003$ ). Indeed, these spreads are consistent with that expected from the photometric errors alone. We also provided another estimation for the RGB width,  $W_{\text{RGB}}$ , and this results

---

<sup>8</sup> $C_{F336W,F438W,F814W}$  and  $C_{F343N,F438W,F814W}$  spreads between the solar and enriched model and between solar and intermediate models were calculated in the RGB in a magnitude range  $20.2 \leq m_{F438W} \leq 21.2$ .

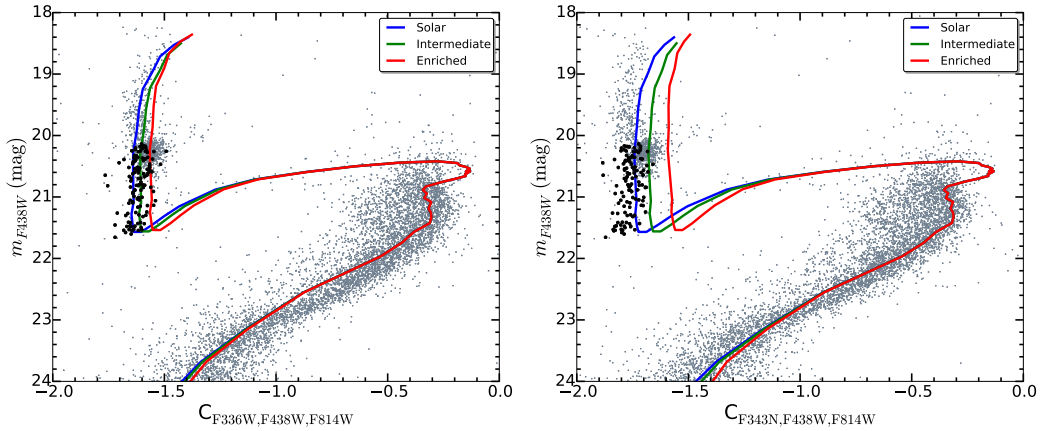


Figure 2.7:  $C_{F336W,F438W,F814W}$  (left) and  $C_{F343N,F438W,F814W}$  (right) vs.  $m_{F438W}$  CMD of NGC 419. Black circles indicate the selected RGB stars. The blue, green and red solid curves represent stellar evolution models ( $\log[\text{age}/\text{Gyr}] = 9.15$ ,  $[\text{Fe}/\text{H}] = -0.7$ ) for solar ( $[\text{C}/\text{Fe}] = [\text{N}/\text{Fe}] = [\text{O}/\text{Fe}] = 0$ ), intermediate ( $[\text{C}/\text{Fe}] = [\text{O}/\text{Fe}] = -0.1$ ,  $[\text{N}/\text{Fe}] = +0.5$ ) and enriched ( $[\text{C}/\text{Fe}] = [\text{O}/\text{Fe}] = -0.6$ ,  $[\text{N}/\text{Fe}] = +1.0$ ) abundance variations, respectively.

in  $W_{\text{RGB}} = 0.139 \pm 0.013$  for  $C_{F336W,F438W,F814W}$  and  $W_{\text{RGB}} = 0.157 \pm 0.013$  for  $C_{F343N,F438W,F814W}$ , Figures 2.5 and 2.6. This proves that we do not observe any significant difference in the RGB spreads between the two colours. Hence, we do not detect the presence of multiple populations either in the form of an enriched ( $[\text{C}/\text{Fe}] = [\text{O}/\text{Fe}] = -0.6$ ,  $[\text{N}/\text{Fe}] = +1.0$ ) or intermediate ( $[\text{C}/\text{Fe}] = [\text{O}/\text{Fe}] = -0.1$ ,  $[\text{N}/\text{Fe}] = +0.5$ ) chemical anomaly in NGC 419. If MPs were present in this cluster, a detection would have been expected by simply comparing the observed width of the RGB in these two colours and by finding a significantly broader  $\sigma$  and  $W_{\text{RGB}}$  (about twice as much) in the narrow-band F343N filter colour combination. We can then conclude that no MPs are detected on the RGB of NGC 419. If MPs were present in the way they have been detected in GCs or intermediate-age clusters, we would have been able to observe them in NGC 419 as well. Our analysis can set a limit on  $[\text{N}/\text{Fe}]$  enhancement for NGC 419 to be  $<+0.5$  dex, according to what we derive from the intermediate models. However, it is crucial here to state that N enhancements previously observed in intermediate age clusters showing MPs are far higher, e.g.  $[\text{N}/\text{Fe}] > +1.0$  dex for Lindsay 1 (Hollyhead et al., 2017).

Lastly, we compared the expected spreads from the models with the observed spreads in the RC and URGB. The observed RC width in  $C_{F336W,F438W,F814W}$  is as

large as the one in  $C_{F343N,F438W,F814W}$ . From the models we would expect the  $C_{F336W,F438W,F814W}$  spread to be as twice as much as the  $C_{F343N,F438W,F814W}$  one, if a intermediate or enriched chemical variation was present. Concerning the URGB, despite the fact that the predicted spreads in the URGB are slightly smaller than in the RGB, we still obtain a ratio between expected  $C_{F336W,F438W,F814W}$  and  $C_{F343N,F438W,F814W}$  colour spreads of  $\sim 2$ . We do observe a slightly larger  $W_{\text{URGB}}$  in  $C_{F343N,F438W,F814W}$  than in  $C_{F336W,F438W,F814W}$ , however they are comparable within the errors, at  $\sim 1\sigma$  confidence level ( $W_{\text{URGB}}(\text{CUBI}) = 0.105 \pm 0.012$ ,  $W_{\text{URGB}}(\text{CUnBI}) = 0.129 \pm 0.016$ ).

## 2.4 Discussion

In this Chapter, we analysed new and archival HST images of the SMC cluster NGC 419. We selected RGB stars by using three different CMDs and colour combinations ( $m_{\text{F438W}} - m_{\text{F814W}}$ ,  $m_{\text{F555W}} - m_{\text{F814W}}$ ,  $m_{\text{F336W}} - m_{\text{F438W}}$ ). We used the pseudo-colour indices  $C_{F336W,F438W,F814W}$  and  $C_{F343N,F438W,F814W}$  in order to maximise the effects of multiple populations on the CMDs along the RGB. No splittings were detected, specifically in the lower RGB. Hence, we quantified the spreads in  $C_{F336W,F438W,F814W}$  and  $C_{F343N,F438W,F814W}$  colours of RGB stars and compared them: these have resulted to be almost equal for both filters ( $\sigma_{\text{data}} = 0.043$ ,  $W_{\text{RGB}}(\text{CUBI}) = 0.139 \pm 0.013$ ,  $W_{\text{RGB}}(\text{CUnBI}) = 0.157 \pm 0.013$ ).

We generated MIST isochrones to have an estimate of the age and metallicity of NGC 419 and used these to develop models with different chemical anomalies. A solar, intermediate and enriched levels of enhancement have been adopted for a comparison with data. The predicted spread in  $C_{F336W,F438W,F814W}$  between solar and enriched isochrones was found to be half as broad as the  $C_{F343N,F438W,F814W}$  spread. The same outcome is seen in the spreads between solar and intermediate isochrones.

We would have expected a significant variation in the observed spreads between  $C_{F336W,F438W,F814W}$  and  $C_{F343N,F438W,F814W}$  colours if MPs were present in NGC 419.

We can firmly conclude that no MPs are detected in the RGB of this young ( $\sim 1.4$  Gyr) and massive ( $\gtrsim 2 \times 10^5 M_{\odot}$ ) star cluster. According to our analysis, we can put a limit on [N/Fe] enhancement for NGC 419 to be  $<+0.5$  dex, which is much lower compared to spreads observed in intermediate age clusters showing the presence of MPs (e.g., [N/Fe] $>+1.0$  dex, Lindsay 1, [Hollyhead et al. 2017](#)).

This is not the first work to find a lack of evidence for MPs in clusters younger than  $\sim 6$  Gyr. [Mucciarelli et al. \(2008\), \(2011\), \(2014\)](#) studied six intermediate/young age clusters (namely: NGC 1651, 1783, 1978 and 2173; NGC 1866; NGC 1806) in the LMC and found no significant abundance spreads within them, although for each cluster this result is affected by the low number statistics of stars with spectroscopically determined abundances.

However, it is worth stressing that NGC 419 is the first cluster in our HST photometric survey which does not show evidence for MPs. [Niederhofer et al. \(2017b\)](#) detected MPs in the SMC cluster NGC 121, while [Niederhofer et al. \(2017a\)](#) detected MPs in 3 additional SMC clusters, namely Lindsay 1, NGC 339, NGC 416. This has been spectroscopically corroborated by the work by [Hollyhead et al. \(2017\)](#), which found abundance variations in Lindsay 1, as well. All the GCs studied so far in our survey reside in the SMC and they are massive, ranging between  $\sim 1 - 2 \times 10^5 M_{\odot}$ . Nonetheless, they span a wide range in ages from 1.5 to 10 Gyr. NGC 419 is the youngest, while NGC 121 is the oldest one ( $\sim 10$  Gyr). Lindsay 1, NGC 339, NGC 416 have intermediate ages (from  $\sim 6$  up to  $\sim 8$  Gyr).

This result showed that GC mass can no longer be considered as the only key physical property in order to regulate the presence of MPs (see also [Cabrera-Ziri et al. 2016a](#)). Other factors might contribute, such as age, which could play a major role in the development of MPs. Indeed, no massive GCs aged less than  $\sim 6$  Gyr have been found with chemical spreads so far. However, this would not be universal, since many less massive, Galactic open clusters older than 6 Gyr also do not host MPs (see the recent compilation by [Krause et al. 2016](#)).

We can estimate the amount of mass loss that NGC 419 will undergo over the next

4.5 Gyr (i.e. from its current age of  $\sim 1.5$  Gyr to an age of 6 Gyr, where clusters are observed to host MPs - [Hollyhead et al. 2017](#); [Niederhofer et al. 2017a](#)). In order to estimate this we use the rotation curve of the SMC measured by [Stanimirović, Staveley-Smith & Jones \(2004\)](#) and extrapolate the observations to the galactocentric distance of NGC 419, namely  $\sim 10$  kpc ([Glatt et al., 2008b](#)), obtaining an estimate of  $60 - 70$  km/s. We also assume that the cluster is tidally filling (in order to maximise the stellar mass loss). We apply equation 7 of [Kruijssen & Mieske \(2009\)](#) (see also [Baumgardt & Makino 2003](#), equation 10 and [Lamers et al. 2005](#)) to find the dissolution timescale normalisation,  $t_0$ . Applying this normalisation to the mass of NGC 419 ( $\sim 2 \times 10^5 M_\odot$ ) to find the dissolution timescale,  $t_{\text{dis}} = t_0 * M^\gamma$  (adopting  $\gamma = 0.62$  - e.g., [Kruijssen & Mieske 2009](#)), we find a  $t_{\text{dis,NGC419}} = 152$  Gyr. If we assume that the cluster loses mass linearly (see the discussion in [Lamers et al. 2005](#)) we find that over the next 4.5 Gyr the cluster will lose  $\sim 3\%$  of its mass<sup>9</sup>. Additionally, the cluster is expected to lose of order 9% of its mass due to stellar evolution. NGC 419 is expected to lose, in total, roughly  $\sim 12\%$  of its current mass over the next 4.5 Gyr (this is an upper limit as we assumed it was tidally limited). Hence, we conclude that NGC 419 (similarly to the other clusters in our sample in the SMC/LMC, with  $M \gtrsim 10^5 M_\odot$ ) is not expected to undergo significant mass loss over the next few Gyr (see also [Cabrera-Ziri et al. 2016b](#)).

In addition to this, in the same galaxy (i.e., the SMC), we have found both the presence and absence of the MPs phenomenon. [Glatt et al. \(2008b\)](#) reported the distribution of star clusters in the SMC, by using distances derived from isochrones fitting. We noticed that our sample of clusters appears to be distributed over a large range of distances with respect to the galaxy centroid. NGC 339 results to be the closest to the SMC centre ( $\sim 0.7 \pm 2.0$  kpc), although with a relatively large uncertainty. This is followed by NGC 416 with a distance of  $\sim 4$  kpc, Kron 3 ( $\sim 7$  kpc) and NGC 121 ( $\sim 9$  kpc). The furthest cluster is Lindsay 1 (more than 13 kpc away), while our cluster, NGC 419, is  $\sim 10$  kpc away from the SMC centre. Accordingly, it appears that the mechanism responsible for enrichment does not depend strongly on the current environment which

---

<sup>9</sup>For this, we assumed a circular orbit around the SMC for NGC 419. If we assume a high eccentricity orbit, the mass loss rate due to dissolution could be up to a factor of  $\sim 2$  higher.

surrounds the cluster.

When this work was first published, the youngest GCs which show MPs are NGC 416 (Niederhofer et al., 2017a) and Kron 3 (Hollyhead et al., 2018). At this age ( $\sim 6$  Gyr) and metallicity ( $[\text{Fe}/\text{H}] \simeq -1$ ) we are sampling RGB stars with masses of  $\sim 1 M_{\odot}$ , while at the age of NGC 419 ( $\sim 1.5$  Gyr) we search for MPs at stellar masses of  $1.6 M_{\odot}$ , in the RGB. Hence, our results might also imply that the MPs phenomenon could manifest only below  $\sim 1 M_{\odot}$  and be also due to a stellar evolutionary effect.

NGC 419 shows one of the largest eMSTO, well noticeable in the  $m_{\text{F}438\text{W}} - m_{\text{814W}}$  and  $m_{\text{F}555\text{W}} - m_{\text{814W}}$  vs.  $m_{\text{814W}}$  CMDs in Fig. 2.3 and also in  $C_{\text{F}336\text{W},\text{F}438\text{W},\text{F}814\text{W}}$  and  $C_{\text{F}343\text{N},\text{F}438\text{W},\text{F}814\text{W}}$  colours (Fig. 2.5 and Fig. 2.6). Our results place limits on the explanation of the eMSTO feature as an age spread (Goudfrooij et al., 2014). Indeed, if multiple SF episodes due to gas processed by a first generation of stars occurred within the cluster, this would lead to self-enrichment. We did not observe any chemical spread in NGC 419, hence our data might lend support to alternative interpretations, e.g. that the MS spread is caused by a distribution of rotational velocities (e.g., Bastian & de Mink 2009; Brandt & Huang 2015; Niederhofer et al. 2015; Wu et al. 2016).

The results presented in this Chapter highlight that age could play a decisive role in determining the presence of MPs. On the contrary, mass or environment can be excluded as the only key factors in this scenario. However, a larger sample is needed in order to confirm such trends. We continue our analysis of Magellanic Cloud clusters aged  $\lesssim 1 - 2$  Gyr whose data are already in hand and present the results in the forthcoming Chapter (§3).

# Chapter 3

## Age as a major factor in the onset of multiple populations

In this Chapter I present the analysis of the LMC cluster NGC 1978, aged  $\sim 2$  Gyr old, one of the youngest clusters showing MPs to date (§3.1). In §3.2 I report on the first global results from the HST survey and I discuss about them in §3.3. This Chapter is based on the work published in [Martocchia et al. \(2018a\)](#).

### 3.1 Analysis

In order to select cluster members, we defined an ellipse region centred in the centre of the cluster with semimajor axis of 1200 pixels and ellipticity  $\epsilon = 0.25^1$ . It is indeed well-known from previous studies ([Geisler & Hodge, 1980](#); [Mucciarelli et al., 2007](#)) that NGC 1978 shows a non-negligible ellipticity. 3.1 shows the  $m_{\text{F555W}} - m_{\text{F814W}}$  vs.  $m_{\text{F555W}}$  CMD of NGC 1978 before (left panel) and after (right panel) the field star subtraction.

---

<sup>1</sup>We define the ellipticity as  $\epsilon = \sqrt{(a^2 - b^2)/a^2}$ , where  $a$  and  $b$  represent the semimajor and semiminor axes, respectively.

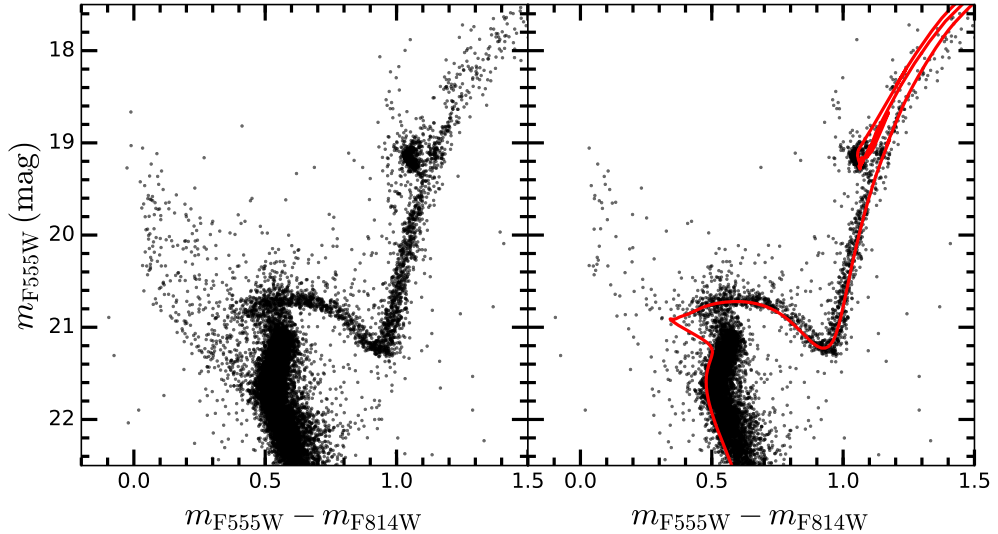


Figure 3.1:  $m_{F555W} - m_{F814W}$  vs.  $m_{F555W}$  CMD of NGC 1978 before (left panel) and after (right panel) the field star subtraction. The red curve in the right panel represents the MIST isochrone we adopted for NGC 1978. The parameters used to derive it are:  $\log(t/\text{yr}) = 9.35$  (corresponding to  $\sim 2.2$  Gyr); distance modulus  $M - m = 18.5$ ;  $E(B - V) = 0.07$ ; metallicity  $[\text{Fe}/\text{H}] = -0.5$ .

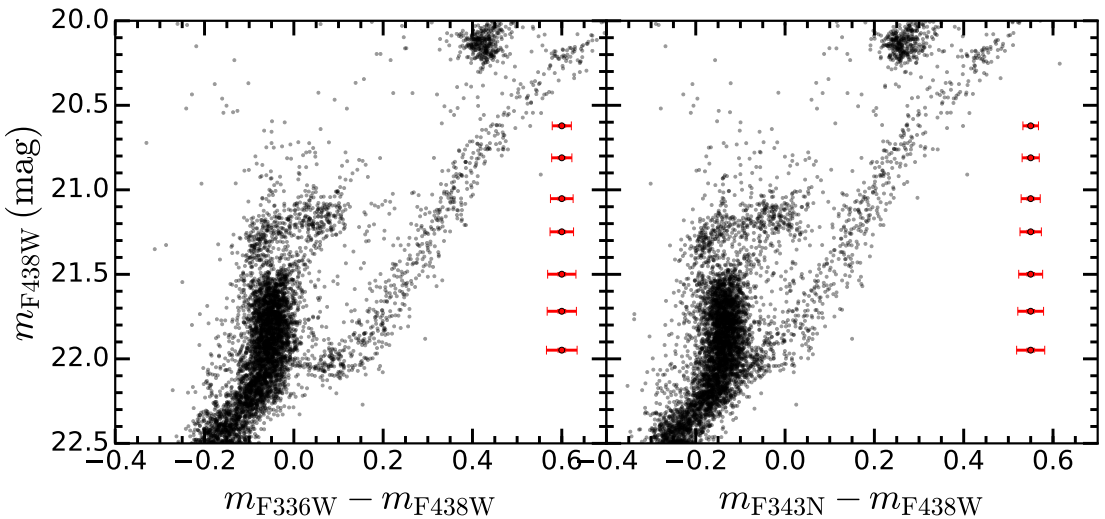


Figure 3.2:  $m_{F336W} - m_{F438W}$  vs.  $m_{F438W}$  (left panel) and  $m_{F343N} - m_{F438W}$  vs.  $m_{F438W}$  (right panel) CMD of NGC 1978. On the right side, the median of photometric errors in colour and magnitude is reported as red filled circles in bins of  $\sim 0.2$  mag.

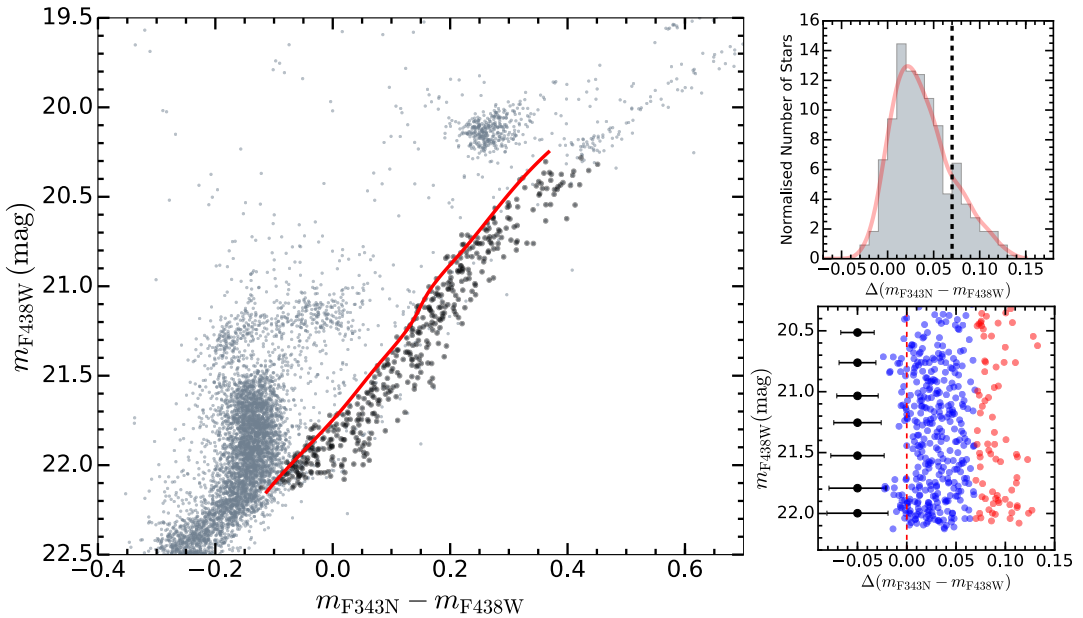


Figure 3.3: *Left Panel:* CMD of NGC 1978 in  $m_{\text{F}343\text{N}} - m_{\text{F}438\text{W}}$  vs.  $m_{\text{F}438\text{W}}$  space. Black filled circles indicate the final selected RGB stars. The red solid line marks the fiducial line defined on the blue edge of the RGB. *Right Panel:* Histogram of the distribution of RGB stars in NGC 1978 (top), in  $\Delta(m_{\text{F}343\text{N}} - m_{\text{F}438\text{W}})$  colours. The red thick curve represents the KDE. The black vertical dashed line marks the adopted separation for FP and SP stars.  $\Delta(m_{\text{F}343\text{N}} - m_{\text{F}438\text{W}})$  vs.  $m_{\text{F}438\text{W}}$  is shown on the right bottom panel, where blue (red) filled circles denotes FP (SP) stars and the red dashed line marks the verticalised fiducial line. On the left side, the median of photometric errors in colour is reported as black filled circles in bins of 0.25 mag. The errors on  $m_{\text{F}438\text{W}}$  magnitudes are smaller than the marker size.

### 3.1.1 The CMD in UV colours

Fig. 3.2 shows the CMD of NGC 1978 in  $m_{\text{F}336\text{W}} - m_{\text{F}438\text{W}}$  vs.  $m_{\text{F}438\text{W}}$  (left panel) and  $m_{\text{F}343\text{N}} - m_{\text{F}438\text{W}}$  vs.  $m_{\text{F}438\text{W}}$  space (right panel). From a first inspection, the CMDs show a visible splitting in the lower RGB, plus a broadened width of the RGB when compared to the observational errors. The median of errors in colour and magnitude is reported on the right side of both figures as red filled circles in bins of  $\sim 0.2$  mag. We will discuss in the next Section (§3.1.2) how we carried out the analysis in order to explain these features as chemical variations of C and N, i.e. as the presence of a second stellar population in the young cluster NGC 1978. We stress here that the observed red sequence in the RGB survived after decontamination from field stars.

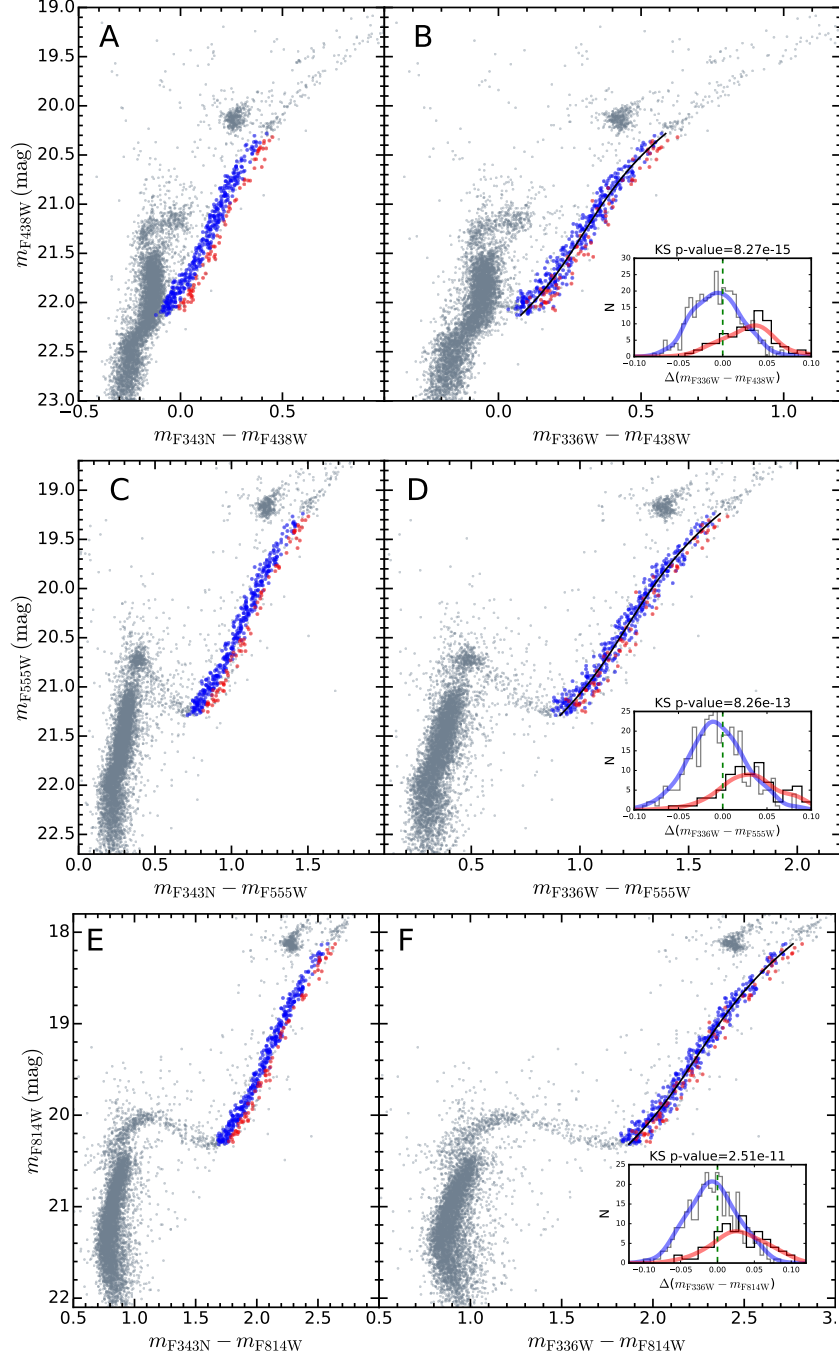


Figure 3.4: CMDs of NGC 1978 in  $m_{F343N} - m_{F438W}$  vs.  $m_{F438W}$  (panel A),  $m_{F336W} - m_{F438W}$  vs.  $m_{F438W}$  (panel B),  $m_{F343N} - m_{F555W}$  vs.  $m_{F555W}$  (panel C),  $m_{F336W} - m_{F555W}$  vs.  $m_{F555W}$  (panel D),  $m_{F343N} - m_{F814W}$  vs.  $m_{F814W}$  (panel E),  $m_{F336W} - m_{F814W}$  vs.  $m_{F814W}$  (panel F). Blue (red) filled circles mark the selected FP (SP). The black solid lines mark the defined fiducial lines. In the insets of the right panels, the histograms of the distribution of the RGB FP (gray) and SP (black) stars is shown, in  $\Delta(m_{F336W} - m_{F438W})$  (panel B),  $\Delta(m_{F336W} - m_{F555W})$  (panel D), and  $\Delta(m_{F336W} - m_{F814W})$  (panel F) colours. The blue (red) thick curve represents the KDE for the FP (SP) stars. The dashed green line represents the verticalised fiducial line.

### 3.1.2 The Red Giant Branch

Our goal is to conservatively select RGB cluster members, in order to search for evidence of MPs. While optical colours are not sensitive to star-to-star C, N, O abundance variations, they can be extremely useful for selecting a clean sample of RGB stars. We thus made the first selection in  $m_{\text{F}438\text{W}} - m_{\text{F}814\text{W}}$  vs.  $m_{\text{F}814\text{W}}$  CMD and a second one in  $m_{\text{F}555\text{W}} - m_{\text{F}814\text{W}}$  vs.  $m_{\text{F}814\text{W}}$  CMD. Finally, we made a last selection in the  $m_{\text{F}343\text{N}} - m_{\text{F}438\text{W}}$  vs.  $m_{\text{F}438\text{W}}$  CMD, as a few objects were scattered far off the RGB. Fig. 3.3 shows the  $m_{\text{F}343\text{N}} - m_{\text{F}438\text{W}}$  vs.  $m_{\text{F}438\text{W}}$  CMD of NGC 1978 with the final selected RGB stars marked as black filled circles.

We defined a fiducial line on the blue edge of the RGB in the  $m_{\text{F}343\text{N}} - m_{\text{F}438\text{W}}$  vs  $m_{\text{F}438\text{W}}$  CMD and this is displayed in the left panel of Fig. 3.3 as a solid red line. Next, we calculated the distance in  $m_{\text{F}343\text{N}} - m_{\text{F}438\text{W}}$  colours of each RGB star from the fiducial line,  $\Delta(m_{\text{F}343\text{N}} - m_{\text{F}438\text{W}})$ . We show the histogram of the distribution in  $\Delta(m_{\text{F}343\text{N}} - m_{\text{F}438\text{W}})$  colours in the top right panel of Fig. 3.3. We also derived the kernel density distribution (KDE) from a Gaussian kernel. This is shown in the top right panel of Fig. 3.3 as a thick red curve. The KDE reveals both broadening and asymmetry in the distribution, along with the presence of a bump for  $\Delta(m_{\text{F}343\text{N}} - m_{\text{F}438\text{W}}) \gtrsim 0.06$ . Hence, we adopted  $\Delta(m_{\text{F}343\text{N}} - m_{\text{F}438\text{W}}) = 0.07$  as the verticalised colour to separate the first population of stars (FP) from the second population (SP). This separation is represented with a black vertical dashed line in the top right panel of Fig. 3.3. The bottom right panel of Fig. 3.3 shows the  $\Delta(m_{\text{F}343\text{N}} - m_{\text{F}438\text{W}})$  colours vs.  $m_{\text{F}438\text{W}}$ , where FP are represented with blue filled circles while SP are represented in red. The red dashed vertical line marks the adopted fiducial line. We find that the SP represents 18% of the total selected RGB stars.

In order to verify that this broadening is due to the presence of multiple populations and not to photometric errors or field stars, we performed several tests.

We derived our final photometric catalogue by selecting stars based on photometric quality indicators (chi and sharpness). We additionally checked the quality of our

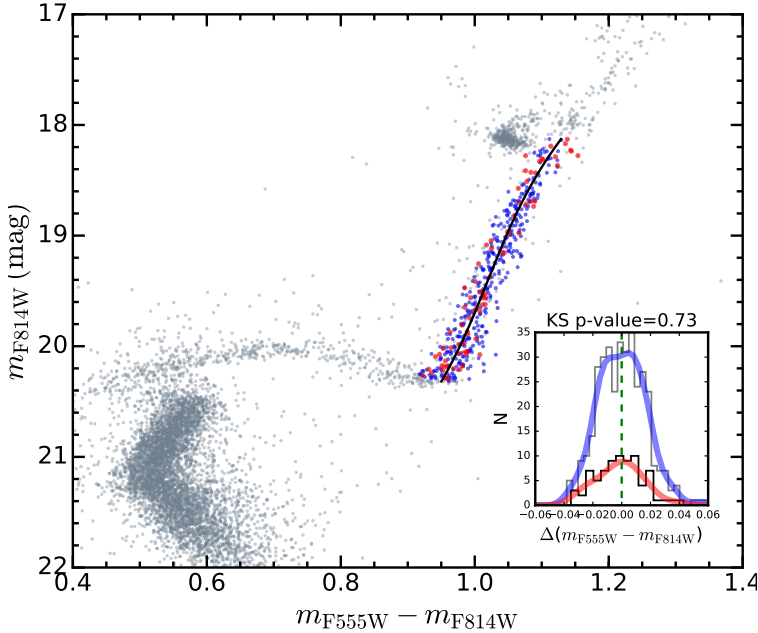


Figure 3.5: CMD of NGC 1978 in  $m_{\text{F}555\text{W}} - m_{\text{F}814\text{W}}$  vs.  $m_{\text{F}814\text{W}}$  space. Symbols as in Fig. 3.4. The black solid line marks the defined fiducial line. In the insets of the right panels, the histogram of the distribution of the RGB FP (gray) and SP (black) stars is shown, in  $\Delta(m_{\text{F}555\text{W}} - m_{\text{F}814\text{W}})$  colours. The blue (red) thick curve represents the KDE for the FP (SP) stars. The dashed green line represents the verticalised fiducial line.

photometry by comparing the average errors of the two populations in  $m_{\text{F}343\text{N}} - m_{\text{F}438\text{W}}$  colours, with both having a mean error of  $\sim 0.025$ . Then, we investigated whether a more severe selection based on photometric errors might invalidate our results. We selected *bona-fide* stars by applying a sigma-rejection in the error versus magnitude diagrams ( $m_{\text{F}336\text{W}}$ ,  $m_{\text{F}343\text{N}}$  and  $m_{\text{F}438\text{W}}$ ) of our original catalogue. We derived the median values in bins of 0.5 mag for each diagram and excluded stars in each bin at more than  $3\sigma$  from the median. We repeated the same analysis with  $1\sigma$  and  $2\sigma$  cuts. Our results stay unchanged and the SP sequence never disappeared.

In Fig. 3.4 we plotted the FP (blue filled circles) and SP (red filled circles) in several colour-magnitude spaces. Panel A shows the  $m_{\text{F}343\text{N}} - m_{\text{F}438\text{W}}$  vs.  $m_{\text{F}438\text{W}}$  CMD of NGC 1978. SP stars follow a red sequence on the RGB while FP stars follow a blue sequence, as expected from their selection. Panel B shows the  $m_{\text{F}336\text{W}} - m_{\text{F}438\text{W}}$  vs.  $m_{\text{F}438\text{W}}$  CMD, panels C and D show the  $m_{\text{F}343\text{N}} - m_{\text{F}555\text{W}}$  vs.  $m_{\text{F}555\text{W}}$  and  $m_{\text{F}336\text{W}} - m_{\text{F}555\text{W}}$  vs.  $m_{\text{F}555\text{W}}$  and, lastly, panels E and F show the  $m_{\text{F}343\text{N}} - m_{\text{F}814\text{W}}$  vs.  $m_{\text{F}814\text{W}}$  and  $m_{\text{F}336\text{W}} - m_{\text{F}814\text{W}}$  vs.  $m_{\text{F}814\text{W}}$  CMDs, respectively. We defined a fidu-

cial line for the selected RGB stars in the  $m_{\text{F}336\text{W}} - m_{\text{F}438\text{W}}$  vs  $m_{\text{F}438\text{W}}$ ,  $m_{\text{F}336\text{W}} - m_{\text{F}555\text{W}}$  vs  $m_{\text{F}555\text{W}}$  and  $m_{\text{F}336\text{W}} - m_{\text{F}814\text{W}}$  vs  $m_{\text{F}814\text{W}}$  CMDs. These are displayed as black solid lines in panels B, D and F of Fig. 3.4. We then calculated the distance of each RGB star from the fiducial line to obtain the  $\Delta(m_{\text{F}336\text{W}} - m_{\text{F}438\text{W}})$ ,  $\Delta(m_{\text{F}336\text{W}} - m_{\text{F}555\text{W}})$  and  $\Delta(m_{\text{F}336\text{W}} - m_{\text{F}814\text{W}})$  verticalised colours. In the insets of panels B, D and F of Fig. 3.4, the histograms of the distribution in  $\Delta(\text{Colours})$  of the FP (gray) and SP (black) stars is shown. The blue (red) thick curve represents the KDE for the FP (SP) stars. Note that the FP and SP sequences were selected in the  $m_{\text{F}343\text{N}} - m_{\text{F}438\text{W}}$  vs.  $m_{\text{F}438\text{W}}$  CMD. In all panels, the distribution of FP presents a clear offset from the SP, with the FP sequence bluer and the SP redder. In the right panels, this was specifically highlighted by showing the  $\Delta(\text{Colors})$  distributions, where the peak of the FP KDE is clearly shifted with respect to the peak of the SP KDE. To quantify this, we performed the Kolmogorov-Smirnov (KS) test between the FP and SP stars distributions in the three  $\Delta(\text{Colours})$ , in order to understand if they are consistent with having been sampled from the same parent distribution. We derived  $p\text{-values} < 10^{-10}$  for all three  $\Delta(\text{Colours})$ , thus demonstrating that the distributions are indeed different. This clearly points toward a chemical effect, as errors on  $m_{\text{F}438\text{W}}$  (WFC3/UVIS) are completely independent from errors on  $m_{\text{F}555\text{W}}$  and  $m_{\text{F}814\text{W}}$  (ACS/WFC). We note that the selection of FP and SP stars was made in the  $m_{\text{F}343\text{N}} - m_{\text{F}438\text{W}}$  vs.  $m_{\text{F}438\text{W}}$  CMD so the  $m_{\text{F}336\text{W}} - m_{\text{F}555\text{W}}$  vs.  $m_{\text{F}555\text{W}}$  and  $m_{\text{F}336\text{W}} - m_{\text{F}814\text{W}}$  vs.  $m_{\text{F}814\text{W}}$  CMD are completely independent measurements.

Fig. 3.5 shows the  $m_{\text{F}555\text{W}} - m_{\text{F}814\text{W}}$  vs.  $m_{\text{F}814\text{W}}$  CMD of NGC 1978 with FP (SP) superimposed as blue (red) filled circles. We performed the same analysis as in the UV CMDs (see Fig. 3.4) and we show the histograms of the distribution for FP (in gray, blue KDE) and SP (black, red KDE) stars in  $\Delta(m_{\text{F}555\text{W}} - m_{\text{F}814\text{W}})$  colours in the inset of Fig. 3.5. In this combination, as expected given the lack of sensitivity to MP in these filters, the two sequences are well mixed, showing no signs of systematic offsets. This is confirmed by the KS test, which returns a  $p\text{-value} = 0.73$ .

Finally, we report on how the two populations are distributed as a function of radial distance from the centre of the cluster. Fig. 3.6 shows the normalized cumulative

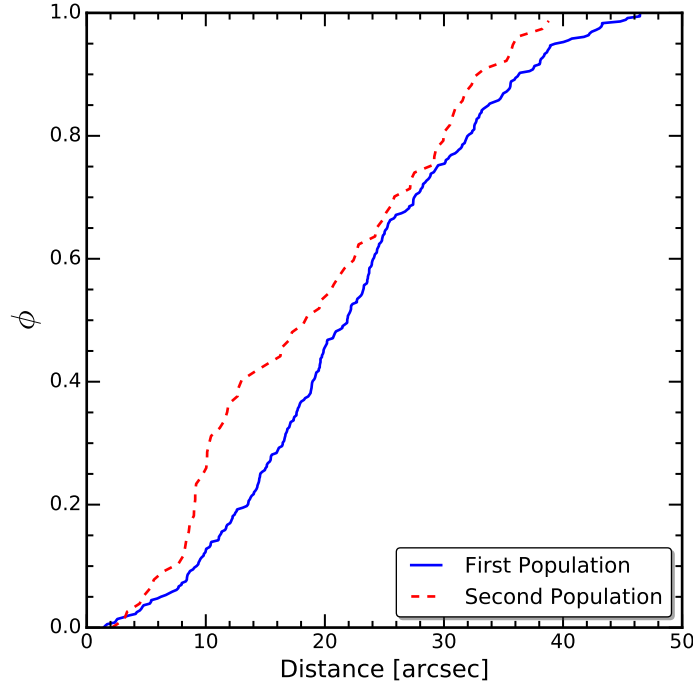


Figure 3.6: Cumulative distribution of FP (blue solid line) and SP (red dashed line) as a function of the radial distance from the cluster centre.

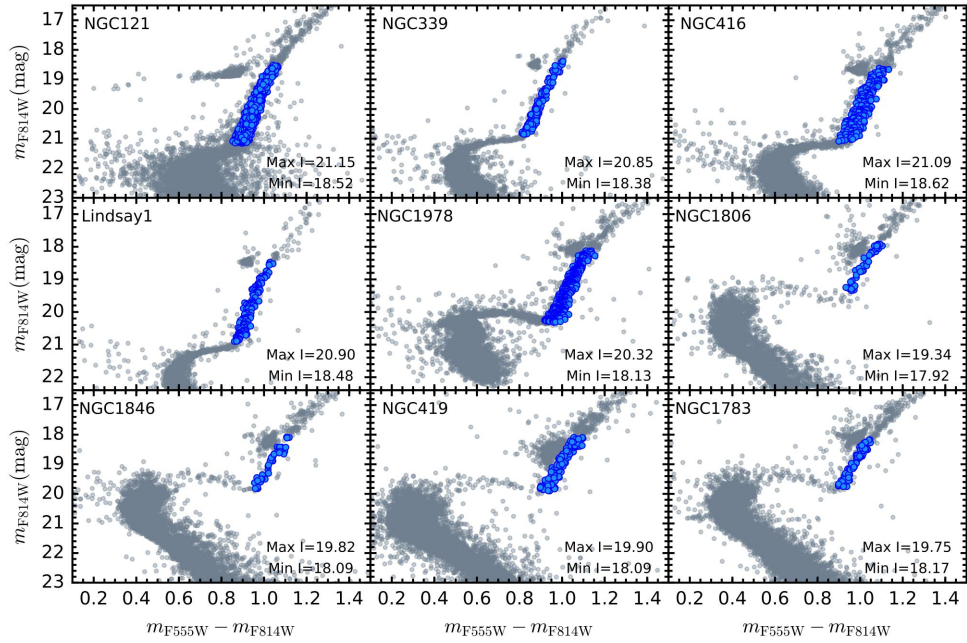


Figure 3.7:  $m_{F555W} - m_{F814W}$  vs.  $m_{F814W}$  CMDs for all the targeted clusters in our HST survey. Blue filled circles indicate the selected RGB stars for each cluster. The maximum and minimum values of the selection in  $m_{F814W}$  magnitudes are superimposed in each panel.

radial distribution of the primordial (blue solid line) and enriched (red dashed line) populations. We found that the second population is more centrally concentrated than the FP up to a distance of  $\sim 50''$  from the cluster centre. We performed the KS test on the two population radial distributions. The probability that they belong to the same parent distribution is relatively low, being  $< 1\%$ . This test statistically shows that the two radial distributions are likely different. Additionally, the evidence for the SP to be centrally concentrated reinforce the cluster membership of the red sequence stars. We also corrected our photometric dataset for differential reddening (DR) and we repeated the exact same analysis. All results stay unchanged. For more specific details on the DR correction procedure, see Chapter 2, §2.2.3.

It might be argued that the SP sequence is composed of evolved binaries on the RGB, due to the likely presence of a large number of blue stragglers in NGC 1978 (see Fig. 3.1). However, evolved blue straggler stars (BSS) should instead be slightly bluer in colour than the RGB, according to [Sills, Karakas & Lattanzio \(2009\)](#), where they assumed that blue stragglers were formed through stellar collision. This is not compatible to what we observe, as the SP distribution of stars is well overlapped to the FP sequence in the  $m_{F555W} - m_{F814W}$  vs  $m_{F814W}$  CMD (Fig. 3.5). Additionally, [Tian et al. \(2006\)](#) looked at BSS formed via mass transfer rather than collision. As pointed out by [Sills, Karakas & Lattanzio \(2009\)](#), their evolutionary tracks of the BSS are comparable to normal stars after the mass transfer occurred. Thus, the same condition mentioned above must apply.

All tests point towards the conclusion that MPs are detected in the RGB of NGC 1978. This was the first cluster hosting chemical abundance anomalies at such a young age ( $\sim 2$  Gyr).

The same analysis reported in this Section was performed on the younger clusters in our sample (namely, NGC 419, 1783, 1806 and 1846). On the contrary, we found no clear evidence for MPs in their RGBs. I will report the global results from our HST survey in the next Section (§3.2).

## 3.2 Results

The  $C_{F336W,F438W,F814W}$  pseudo-colour, defined as  $(m_{F336W} - m_{F438W}) - (m_{F438W} - m_{F814W})$ , has been shown to be very effective at unveiling multiple sequences on the RGB (Monelli et al., 2013; Dalessandro et al., 2016). Here, we take advantage of a similar pseudo-colour, known as  $C_{F343N,F438W,F814W} \equiv (m_{F343N} - m_{F438W}) - (m_{F438W} - m_{F814W}) \equiv \text{CUnBI}$ , to provide a direct and quantifiable comparison between all the clusters in our survey. Additionally, these pseudo-colours do not have a strong dependence on the effective temperature of stars, such that the RGB is almost vertical in the diagram, i.e. splittings are more easily discernible in this combination and are also largely independent of potential spreads in He (see Chapter 2, §2.2.4, Martocchia et al. 2017). We finally exploit  $C_{F343N,F438W,F814W}$  to compare our data with stellar atmosphere models in §3.2.1.

We adopted the same analysis for each cluster. RGB stars have been selected in three CMDs of each cluster to establish membership. Figure 3.7 shows the  $m_{F555W} - m_{F814W}$  vs.  $m_{F814W}$  CMDs for all the targeted clusters in our survey. Blue filled circles represent the RGB stars which passed all three selections. We defined the selection by choosing stars in the lower RGB, which are fainter than the RGB bump (to avoid chemical mixing due to stellar evolutionary effects). We verticalised our selected RGB stars in  $C_{F343N,F438W,F814W}$  vs  $m_{F438W}$  CMD and we calculated the distance  $\Delta\text{CUnBI}$  from the fiducial line for each star. The top left panel of Fig. 3.8 shows the  $C_{F343N,F438W,F814W}$  vs.  $m_{F438W}$  CMD of NGC 1978, while the bottom left panel shows the  $C_{F343N,F438W,F814W}$  vs.  $m_{F438W}$  CMD of NGC 1783, where MPs were not detected. Symbols are as in Fig. 3.4. The black solid line marks the defined fiducial line to derive the  $\Delta\text{CUnBI}$ . As expected in this filter combination, for NGC 1978, FP and SP stars show an unambiguous offset in colours, with the FP having bluer colours and the SP redder. This is also evident in the right top panel of Fig. 3.8, where the NGC 1978 histogram of the  $\Delta\text{CUnBI}$  distributions for both FP and SP is shown. The KDE distributions are also indicated, in blue for the FP and in red for the SP. The same is shown on the bottom right panel of Fig. 3.8, but for NGC 1783, where there is no

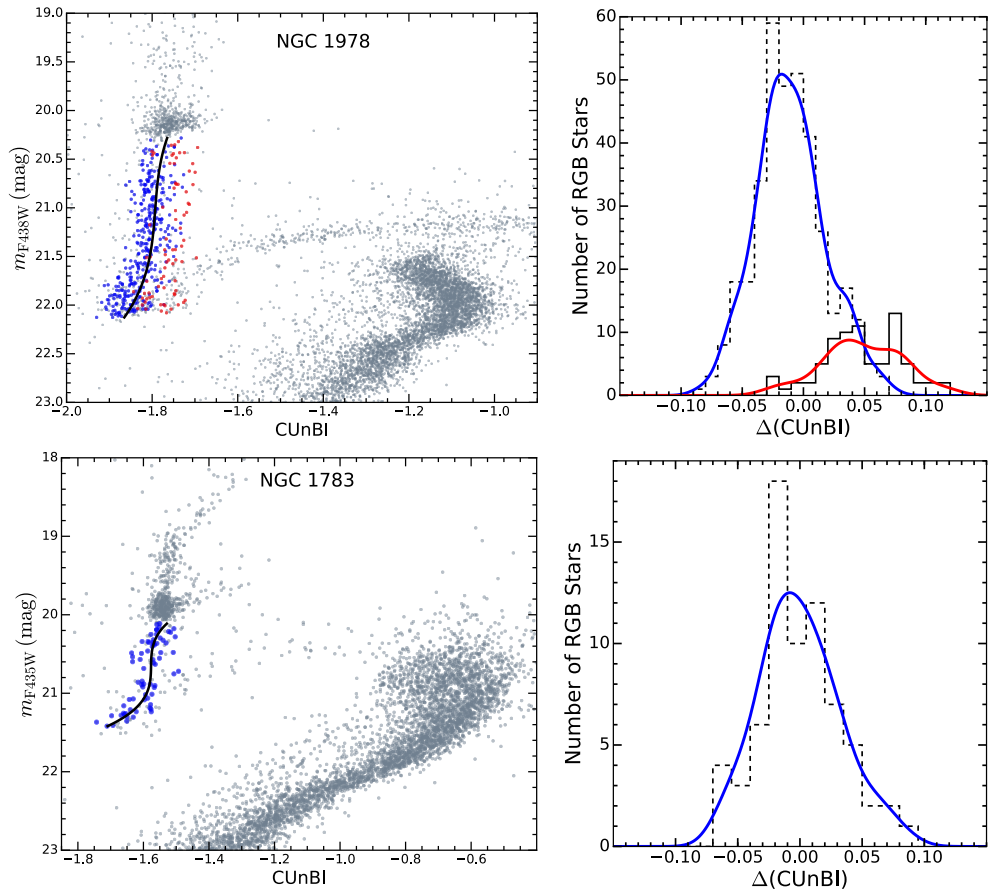


Figure 3.8: Top (bottom) left panels:  $C_{F343N,F438W,F814W}$  ( $C_{\text{UnBI}}$ ) vs  $m_{F438W}$  ( $m_{F435W}$ ) CMD of NGC 1978 (NGC 1783), where symbols are as in Fig. 3.4. The black solid line indicates the fiducial line. Top (bottom) right panels: histogram of the distributions in  $\Delta(C_{\text{UnBI}})$  colours for the FP (dashed) and SP (solid) for NGC 1978 (NGC 1783), with KDEs superimposed (blue for the FP and red for the SP).

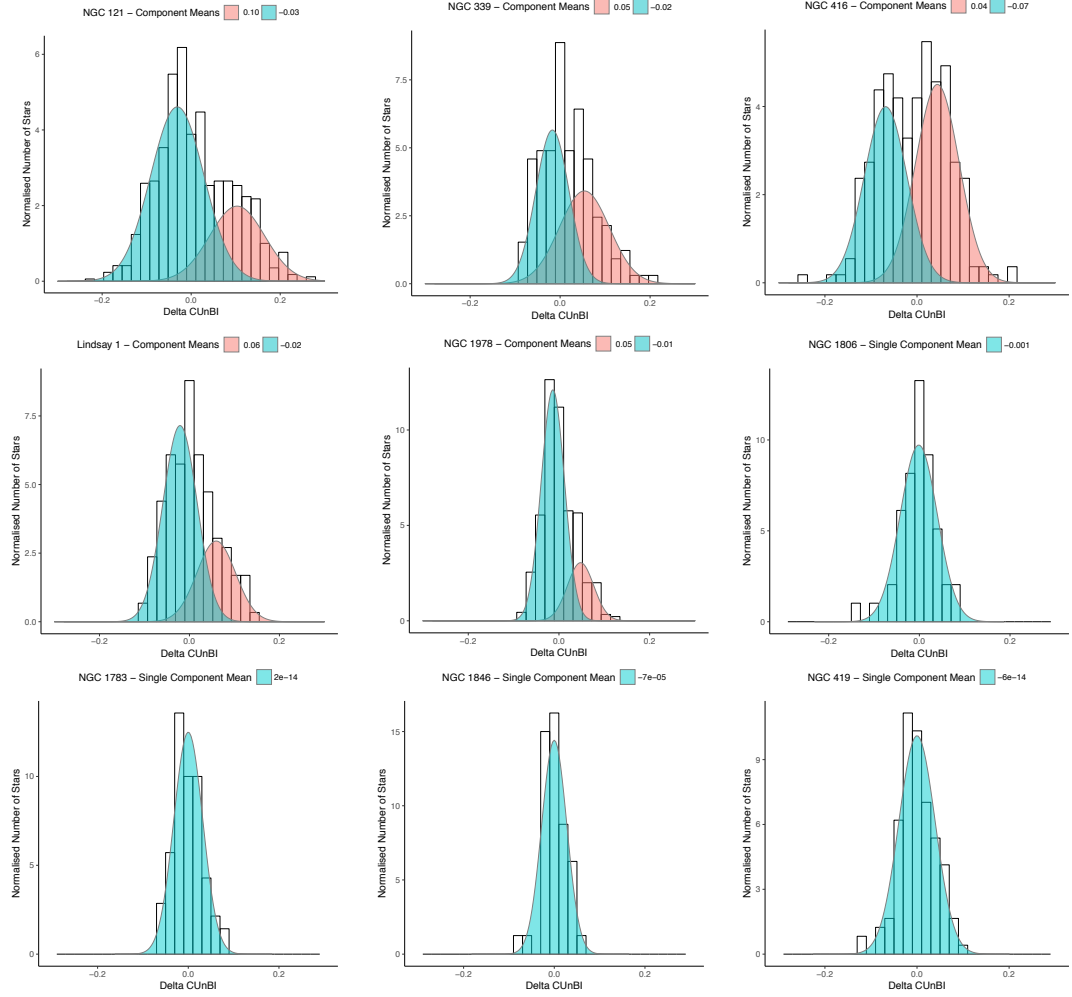


Figure 3.9: Histograms of the distribution of RGB stars in CUnBI colours for all clusters in our survey. The GMM fit on unbinned data are marked in blue for the FP and red for the SP. The means of the Gaussian distributions are labelled on top of the plots.

hint for asymmetry or broadening.

Next, we fit the unbinned verticalised  $\Delta\text{CUnBI}$  data with Gaussian Mixture Models (GMMs, see Fig. 3.9, where we also plot the binned  $\Delta\text{CUnBI}$  distribution for visual representation) to identify the presence of multiple Gaussian components in the colour distribution, hence two or more populations with different N abundance. We fit the data with the SCIKIT-LEARN python package called MIXTURE<sup>2</sup>, which applies the expectation-maximization algorithm for fitting mixture-of-Gaussian models. In order to determine the number of Gaussians which best reproduce the data, we adopted the Akaike Information Criterion (AIC, Akaike 1974). We found that the  $\Delta\text{CUnBI}$

<sup>2</sup><http://scikit-learn.org/stable/modules/mixture.html>

distributions of NGC 1978, NGC 416, NGC 339, NGC 121 and Lindsay 1 are best represented with 2 components, while only one component is found for NGC 419, 1783, 1806 and 1846 (see Fig. 3.9).

The final result is that all clusters older than 2 Gyr show multiple Gaussian components in the fit, i.e. MPs are present, while all clusters younger do not. We then defined  $\delta^{\text{RGB}}(\text{CUnBI})$  as the difference between the means of the two main Gaussian components in the  $\Delta\text{CUnBI}$  distribution. This gives a robust indication on the level of N enrichment present in clusters which host MPs. Errors on  $\delta^{\text{RGB}}(\text{CUnBI})$  were calculated with a bootstrap technique based on 5000 GMMs realizations. We set  $\delta^{\text{RGB}}(\text{CUnBI})$  of clusters which do not show MPs to zero.

Although statistically less likely, to be as conservative as possible, we forced the GMM procedure to fit the one-gaussian component data with two Gaussian distributions. For NGC 1806 and NGC 1846 the fit yields two almost overlapped gaussians, resulting in  $\delta^{\text{RGB}}(\text{CUnBI}) < 0.01$ . In these two cases, we considered the standard deviation of the single Gaussian as upper error on  $\delta^{\text{RGB}}(\text{CUnBI})$ . For NGC 419 and NGC 1783 the fit finds a separated second Gaussian component, with  $\delta^{\text{RGB}}(\text{CUnBI}) \sim 0.04$ , which was used as upper error on  $\delta^{\text{RGB}}(\text{CUnBI})$ . In order to establish the statistical significance on the second Gaussian component for NGC 419 and NGC 1783, we calculated the errors on the normalisation factor with 5000 bootstrap realisations. The normalisation was found to be consistent with zero for both clusters. Finally, in Table 3.1, we also report for each cluster the probability that a bimodal distribution is rejected, which is in agreement with previous studies ([Niederhofer et al., 2017b,a](#); [Martocchia et al., 2017](#)). This was obtained with a parametric bootstrap technique by using the GMM code by [Muratov & Gnedin \(2010\)](#).

It is worth noting that the GMM fitting method was *not* adopted in order to demonstrate that MPs are detected or not in a given cluster. It was just used as a confirmation of our findings. MPs are primarily detected by selecting samples in the  $m_{\text{F343N}} - m_{\text{F438W}}$  vs.  $m_{\text{F438W}}$  CMD and by examining where they order in the different filter combinations.

We plot  $\delta^{\text{RGB}}(\text{CUnBI})$  as a function of cluster age in Fig. 3.10 for all our targets. Devi-

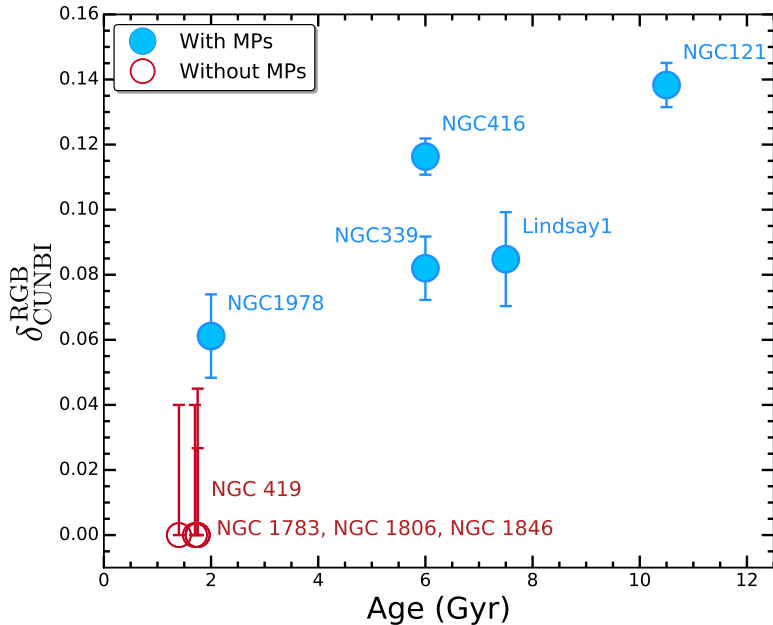


Figure 3.10:  $\delta^{\text{RGB}}(\text{CUnBI})$  as a function of age for the 9 clusters in our HST photometric survey. Clusters which are found to host MPs are indicated with blue filled circles while clusters which do not show MPs are marked with red open circles.

ations from zero, indicating N enrichment, are observed for all clusters older than  $\sim 6$  Gyr, confirming our earlier results (Niederhofer et al., 2017b,a; Hollyhead et al., 2017). Conversely, the narrow RGB in the  $C_{F343N,F438W,F814W}$  vs.  $m_{F438W}$  CMD would exclude the presence of significant nitrogen star-to-star variations in the youngest clusters of our sample, namely NGC 419, 1783, 1806, 1846, with ages of  $\sim 1.5 - 1.7$  Gyr (see also Chapter 2, Martocchia et al. 2017). Finally, strong evidence for MPs is also found for the first time in the  $\sim 2$  Gyr old cluster, NGC 1978. This finding suggests that age is playing a pivotal role in controlling the presence of MPs, as chemical anomalies are detected in all massive clusters older than 2 Gyr while they are lacking at younger ages.

However, it is possible that a certain level of N enrichment (smaller compared to the older clusters) is still present in the younger clusters, which cannot be seen due to observational uncertainties and contamination from field stars (see §3.2.1). Despite this, the main results from this work stay unchanged: we report an unexpected age effect on the onset of MPs. We note that if N-spreads like those observed in the ancient GCs (or those in the 2–8 Gyr old clusters) were present in the clusters younger than 2

Table 3.1: Columns give the following information: (1) cluster name, (2) cluster age in Gyr, (3) probability that a bimodal  $\Delta\text{CUnBI}$  distribution is rejected for each cluster in the survey. References for the ages from Table 2.3.

Cluster Name (1)	Age (Gyr) (2)	$\Delta\text{CUnBI}$ pvalue (3)
NGC 121	10.50	<0.001
Lindsay 1	7.50	0.16
NGC 339	6.00	0.04
NGC 416	6.00	0.03
NGC 1978	2.00	<0.001
NGC 1783	1.75	0.58
NGC 1846	1.75	0.63
NGC 1806	1.70	0.51
NGC 419	1.2-1.6	0.47

Gyr, they would have been readily detected.

### 3.2.1 Comparison with stellar models

We compared MIST isochrones ([Dotter, 2016](#); [Choi et al., 2016](#)) to our data to obtain an estimate of age, metallicity, distance modulus ( $M - m$ ) and extinction values. For NGC 1978, we found that the MIST parameters which best match the data and the isochrones are: (i)  $\log(t/\text{yr}) = 9.35$  ( $t \sim 2.2$  Gyr), (ii)  $[\text{Fe}/\text{H}] = -0.5$ , (iii)  $M - m = 18.5$ , (iv)  $E(B - V) = 0.07$ . The selected isochrone is superimposed on the  $m_{\text{F}555\text{W}} - m_{\text{F}814\text{W}}$  vs.  $m_{\text{F}555\text{W}}$  CMD of NGC 1978 in Fig. 3.1 as a red solid curve. ([Mucciarelli et al., 2007](#)) report an age of  $t = 1.9 \pm 0.1$  Gyr for NGC 1978 by using several sets of different isochrones (Padua, BaSTI, PEL). Our slightly different choice of age might be due to the different set of isochrones used in this work, i.e. MIST isochrones. However, with this work we do not aim at providing an improved estimate of the age of NGC 1978. We rather need to obtain a reliable MIST isochrone fit to our CMD data, as we will use these values as input for MIST models to develop our synthetic photometry. However, as it is clear from Fig. 3.1, our isochrone does not perfectly match data on the MS or the MSTO. Indeed, in adopting MIST isochrones, we were not able to match perfectly data for all evolutionary stages with any parameters combination. Nonetheless, this issue is somewhat irrelevant for our studies, since we

will focus on the RGB stage.

We adopted three chemical mixtures in the models (see Chapter 2, §2.2.4). First, we calculated a set of scaled solar models ( $[C/Fe] = [N/Fe] = [O/Fe] = 0$ ). Next, we calculated a set of N-enhanced models with  $[C/Fe] = [O/Fe] = -0.1$  dex and  $[N/Fe] = +0.5$  dex. Lastly, we calculated a set of models with slightly less degree of N-enhancement but with solar C and O abundances ( $[C/Fe] = [O/Fe] = 0$  and  $[N/Fe] = +0.3$  dex), in order to check degeneracies between C depletion and N enhancement in CUnBI colours.

The C and O abundances were chosen to keep the  $[(C+N+O)/Fe]$  constant between the models, according to what we observe in standard GCs (Brown, Wallerstein & Oke, 1991; Cohen & Meléndez, 2005; Yong, Grundahl & Norris, 2015; Marino et al., 2016). For each of these chemical mixtures we kept the helium abundance (surface  $Y = 0.248$ ) constant and all other abundances fixed at solar. We also assumed that the model atmospheres had the same chemical abundances at all stellar evolutionary stages. We then integrated our model spectra over the filter transmission curves for WFC3<sup>3</sup> and ACS/WFC<sup>4</sup> and used the zeropoints provided on each instruments website to calculate Vega magnitudes. We directly compare our models to the data.

We exploited the CUnBI pseudo-colour to give an estimate of the level of nitrogen enrichment for the SP stars when MPs are detected and to provide an upper limit where MPs are not detected. Fig. 3.11 shows the  $C_{F343N,F438W,F814W}$  vs.  $m_{F438W}$  CMD of NGC 1978, with a zoom in the RGB region. The black solid, dash-dotted, dashed curves represent isochrones for the three chemical mixtures described above, respectively. Blue (red) filled circles mark the selected FP (SP) RGB stars. Fig. 3.11 shows that the  $[N/Fe] = +0.5$  dex and  $[N/Fe] = +0.3$  dex models are almost completely overlapped, with  $[C/Fe]$  and  $[O/Fe]$  abundances depleted in the former but kept solar in the latter. This means that we expect the same spread on the RGB with a different combination of C and N, i.e. there is a degeneracy between C and N abundances. Un-

---

<sup>3</sup>[http://www.stsci.edu/hst/wfc3/ins\\_performance/throughputs/Throughput\\_Tables](http://www.stsci.edu/hst/wfc3/ins_performance/throughputs/Throughput_Tables)

<sup>4</sup><http://www.stsci.edu/hst/acs/analysis/throughputs>

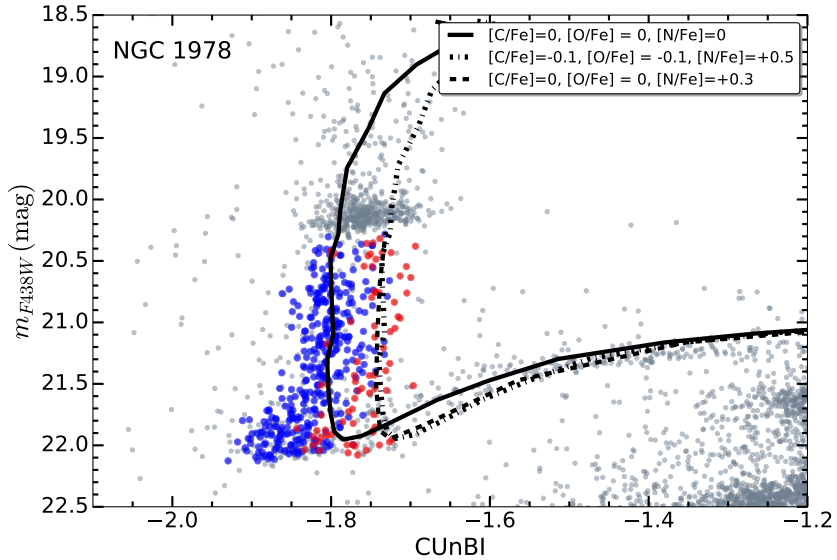


Figure 3.11: CUnBI vs.  $B$  CMD of NGC 1978 zoomed in the RGB region. Blue (red) filled circles indicate the FP (SP) stars. Black solid, dash-dotted, dashed curves represent stellar isochrones for  $[C/Fe] = [N/Fe] = [O/Fe] = 0$ ,  $[C/Fe] = [O/Fe] = -0.1$  and  $[N/Fe] = +0.5$ , and  $[C/Fe] = [O/Fe] = 0$  and  $[N/Fe] = +0.3$  chemical abundance mixtures, respectively.

fortunately, a reliable measure of N enrichment by comparing the observed CUnBI vs.  $m_{F438W}$  CMDs with the models cannot be given, as no spectroscopic measurements of chemical abundances are currently available for this cluster. However, we can still provide a rough estimate, by assuming that MPs in younger clusters are the same as those of ancient GCs, i.e. an enhancement in N is associated with a depletion in C ([Cannon et al., 1998](#)).

Accordingly, we report a N enrichment for NGC 1978 of  $[N/Fe] \sim +0.5$  dex. Also, we can make a differential comparison among NGC 1978 and the younger clusters. We do not detect MPs in NGC 419, 1783, 1806 and 1846 but we cannot exclude the presence of a slight N variation due to observational uncertainties and decontamination from field stars (see §3.2). If we assume a  $[N/Fe] \sim +0.5$  dex for NGC 1978, then we can set an upper limit to any enrichment in the younger clusters (NGC 419, 1783, 1806, 1846) of  $[N/Fe] < +0.3$  dex.

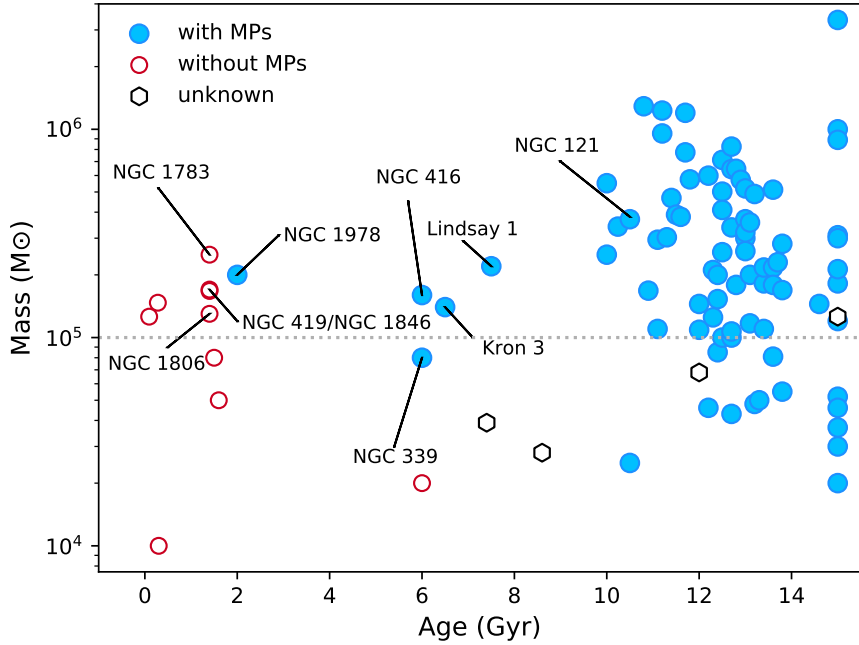


Figure 3.12: The relation between age and mass for the clusters in our survey (labelled) as well as clusters taken from the literature. Clusters which are found to host MPs are indicated with blue filled circles while clusters which do not show MPs are marked with red open circles. Clusters where the presence or absence of MPs is still under debate are shown as open hexagons.

### 3.3 Discussion

In this Chapter, we reported the photometric analysis of new and archival HST images for the LMC cluster NGC 1978 as well as the results from the remaining clusters in our sample. For NGC 1978, the  $m_{F336W} - m_{F438W}$  vs.  $m_{F438W}$  and  $m_{F343N} - m_{F438W}$  vs  $m_{F438W}$  CMDs revealed hints of a splitting in the lower RGB. Additionally, the RGB showed a broadened width compared to the observational errors (Figs. 3.2 and 3.3). We selected RGB stars in three different CMDs and used the  $m_{F343N} - m_{F438W}$  vs.  $m_{F438W}$  CMD to separate the FP from the SP stars. We plotted the FP and SP sequences in several UV CMDs and in all of them, the distribution of FP shows an offset from the SP, with the FP sequence bluer and the SP redder, on average (Fig. 3.4). This does not occur when considering optical CMDs (Fig. 3.5). We also showed that the SP stars present in NGC 1978 is more centrally concentrated than the FP stars (Fig. 3.6). This strongly confirms cluster membership for the red-sequence stars, as well as the

likelihood that they are indeed the product of separate chemical evolution from the FP stars, as SP stars are almost always found to be more centrally concentrated than FP stars.

We can then conclude that MPs are detected in the RGB of NGC 1978, which is  $\sim 2$  Gyr old and has a mass of  $2 - 4 \times 10^5 M_{\odot}$ . This is the first cluster found to host star-to-star abundance variations at such a young age. Future observations to determine if Na (and Al, O, etc...) are necessary to further quantify the results presented here. However, we note that in older GCs where MPs are confirmed to be present, the observed Na spreads are much smaller than the N spreads, hence in NGC 1978 we may only expect Na spreads of  $\sim 0.2$  dex or less. We also revealed that MPs are not instead detected in the RGB of the younger clusters in our survey, namely NGC 1783, 1806, 1846.

We then presented the global results from our HST photometric survey. We took advantage of the CUnBI colour combination in order to compare all the clusters in our survey (§3.2 and Figs. 3.9, 3.10). All clusters older than 2 Gyr host MPs, while chemical anomalies are not detected in those younger than this age. This firmly suggests that there is an age effect in the onset of multiple populations.

We also developed stellar atmosphere models for the chemical anomalies. We exploited CUnBI $\equiv C_{F343N,F438W,F814W}$  to give a rough estimate of the level of N enrichment for the SP stars when MPs are detected and to provide an upper limit where MPs are not detected. We reported a N enrichment for NGC 1978 of  $[N/Fe] \sim +0.5$  dex. Comparing NGC 1978 with the younger clusters, we can set an upper limit to any enrichment in the younger clusters (NGC 419, 1783, 1806, 1846) of  $[N/Fe] < +0.3$  dex (§3.2.1).

In Fig. 3.12 we plot a summary of our HST survey as well as results taken from the literature. We also add here the results for the  $\sim 6.5$  Gyr old SMC cluster Kron 3 (Hollyhead et al., 2018), where MPs have been spectroscopically identified. All of the clusters in our HST survey have masses in excess of  $\sim 10^5 M_{\odot}$ , e.g. the mass for which MPs are almost always found in ancient GCs, but we detect MPs only in clusters older than  $\sim 2$  Gyr.

Taken at face value, this suggests that some mechanism operating only in stars less massive than  $1.5 M_{\odot}$  (the mass of a RGB star at  $\sim 2$  Gyr) may be responsible for the onset of MPs. Note in Fig. 3.12 that there is one cluster older than 2 Gyr where MPs were not detected. This is Berkeley 39, which is a low-mass cluster ( $\sim 10^4 M_{\odot}$ ). Clearly, age is not the only controlling parameter, cluster mass must also come into play, as well as environment might contribute. Future work will be needed to consider the impact of environment on MPs, as a significant factor shaping the amount of chemical anomalies in clusters. Conversely, Ruprecht 106 and IC 4499 are two old clusters ( $> 12$  Gyr) where the presence of MPs is still under debate, with preliminary studies suggesting that MPs may not be present (Villanova et al., 2013; Walker et al., 2011). Also, the presence of MPs is still unknown for other two relatively old clusters, namely Terzan 7 and Pal 12 (7 – 9 Gyr), as only a few stars (less than 5) have light element abundance measurements (e.g. Cohen 2004).

The dependence of light element variations on age is not predicted by any model that has been proposed to explain the formation and evolution of MPs. All self-enrichment models share the notion that a cluster will show MPs only if its mass is larger than a given threshold, i.e. only the most massive clusters should be able to retain the enriched ejecta of a first generation of stars (and accrete new material) to form a second generation. Hence, these models predict that clusters massive enough in the local universe should be undergoing multiple epochs of star-formation, in contradiction with observations (Bastian et al., 2013a; Cabrera-Ziri et al., 2014). More recent versions have attempted to address this issue by invoking special conditions in the early Universe, at redshifts above  $z_{\text{formation}} \sim 2$  (D’Ercole, D’Antona & Vesperini, 2016). However, the discovery of chemical anomalies in NGC 1978 ( $z_{\text{formation}} = 0.17$ ) leads to the conclusion that the onset of MPs cannot be limited to the high- $z$  Universe.

The data presented here tentatively suggest that MPs may be due to a stellar evolutionary effect not yet recognized in standard evolution models. This effect would need to only efficiently operate in stars within massive/dense stellar clusters. NGC 1978 is currently the youngest cluster for which detection of MPs have been reported. At this age ( $\sim 2$  Gyr), the sampled stellar mass in the lower part of the RGB is slightly lower

than  $1.5 M_{\odot}$  while it is  $\sim 1.55 M_{\odot}$  at 1.7 Gyr, i.e. the typical age of the young surveyed clusters where MPs are not found. One potentially important change in this very narrow mass range is that stars above  $\sim 1.5 M_{\odot}$  do not typically possess strong magnetic fields, whereas stars below this mass do. This can also be related with stellar rotational properties, as stars with strong magnetic fields can be magnetically braked, leading to slow rotation rates, whereas stars with weak magnetic fields can remain rapid rotators (e.g. [Cardini & Cassatella 2007](#)). Additionally, we observe the eMSTO in the optical CMD of clusters younger than 1.7 Gyr (NGC 419, 1783, 1806, 1846), while we do not observe such a feature in the  $\sim 2$  Gyr old NGC 1978 (see Fig. 3.7), where the mass of the lower RGB and MSTO stars has decreased below  $1.5 M_{\odot}$ . If the phenomenon is related to stellar rotation and/or magnetic fields, it is worth noting that the rates of stellar rotation are linked to the cluster mass, i.e. rotation can cause environmentally dependent stellar evolutionary effects<sup>5</sup>.

Another intriguing consequence of such an interpretation may be the expected presence of chemical anomalies in stars with masses below  $1.5 M_{\odot}$  on the MS of the young clusters. Furthermore, one immediate implication, to account for the rare objects with  $M < 10^5 M_{\odot}$  seen in Fig. 3.12 that have ages older than 2 Gyr but no MPs, is that the global properties of a cluster (such as its mass, or initial angular momentum) can, under certain circumstances, influence the properties of its individual stars (such as the distribution of rotation speeds). Recent observations ([Corsaro et al., 2017](#)) suggest that this is indeed plausible. However, this remains purely speculative at the moment. This is a completely unexplored direction for the onset of MPs, and further tests need to be carried out to confirm or refute such interpretations.

A major implication of our discovery of MPs in a young (2 Gyr) cluster, is that it lends support to the view that the ancient GCs and young massive clusters (YMCs) share a common formation process, as MPs have now been found in both classes of clusters. While globular and young massive clusters overlap in many of their properties, such as mass, size and stellar density, many models for the formation of GCs have adopted

---

<sup>5</sup>We note that the  $\sim 1.3$  Gyr lower mass open cluster, Trumpler 20, does not show signs of an extended main sequence turnoff. However, it also does not appear to host rapidly rotating stars ([Platais et al., 2012](#)).

special conditions only present in the early Universe ([Trenti, Padoan & Jimenez, 2015](#)). One line of support for such a distinction between the ancient globulars and YMCs was that only globular clusters were thought to host MPs. The results presented here show that the formation of MPs continued at least down to a redshift of  $z = 0.17$ , well past the peak epoch of GC formation in the Universe ( $z = 2 - 5$ , [Brodie & Strader 2006a](#)). Instead, our results support models that explain GC and YMC formation/evolution within a common framework ([Kruijssen, 2015](#); [Pfeffer et al., 2018](#)).

# Chapter 4

## Coeval multiple stellar populations in the young star clusters NGC 1978

As introduced in Chapter 1, depending on which polluter is employed, i.e. the source of enrichment of the chemical anomalies, multiple generational theories predict age spreads from a few Myr (massive and super-massive stars, e.g. [Decressin et al. 2007](#); [de Mink et al. 2009](#), [Denissenkov & Hartwick 2014](#), [Gieles et al. 2018](#)) to 30-200 Myr (asymptotic giant branch, AGB stars, e.g. [D’Ercole et al. 2008](#); [Conroy & Spergel 2011](#)).

An immediate test can be implemented to verify the nature of the polluters, by estimating the age difference among the subpopulations in a cluster. This has been attempted in studies of ancient GCs (e.g., [Marino et al. 2012](#); [Nardiello et al. 2015](#)) but due to the old ages, only upper limits of  $\sim 200$  Myr between the populations have been achieved. If such an experiment could be carried out on younger clusters, more stringent limits could be placed.

One of the most remarkable results from our survey is that NGC 1978, a massive ( $2-4 \times 10^5 M_{\odot}$ , [Westerlund 1997](#)) and relatively young ( $\sim 2$  Gyr old, [Mucciarelli et al. 2007](#)) cluster in the Large Magellanic Cloud (LMC), shows evidence for MPs in its RGB (Chapter 3, [Martocchia et al. 2018a](#)). This is one of the youngest cluster where

the presence of chemical anomalies have been detected. This can be contrasted with NGC 419 which has very similar properties (mass, radius), but it is  $\sim 500$  Myr younger and does not appear to host MPs.

In this Chapter, I take advantage of the unique characteristics of NGC 1978 to place stringent limits on any internal age dispersion. First, I use the subgiant branch (SGB) of NGC 1978 to search for age differences between the different populations in the cluster. Then, we explore the morphology of the MSTO of NGC 1978, showing that this is consistent with a single aged population. This Chapter is based on the work published in [Martocchia et al. \(2018b\)](#).

## 4.1 Observations and Adopted isochrones

In order to translate observational quantities (in units of mag) into age differences in Myr, we used the BaSTI models (“A Bag of Stellar Tracks and Isochrones”, [Pietrinferni et al. 2004](#)). This choice allowed to properly account for the effects of core convective overshooting during the central H-burning stage. We note that the overshooting efficiency  $\Lambda_{\text{ov}}$  is commonly parametrised as a fraction of the pressure scale height ( $H_P$ ). In case of the BaSTI database the following dependence of  $\Lambda_{\text{ov}}$  as a function of the mass: (i)  $\Lambda_{\text{ov}} = 0.2H_p$  for masses larger than  $1.7 M_\odot$ , (ii)  $\Lambda_{\text{ov}} = (M/M_\odot - 0.9)H_p/4$  for stars between  $1.1$ - $1.7 M_\odot$ , and (iii)  $\Lambda_{\text{ov}} = 0H_p$  for stars less massive than  $1.1 M_\odot$ . Stellar masses for a 2 Gyr old cluster are  $\sim 1.45 M_\odot$  at the MSTO and  $\sim 1.47$ - $1.49 M_\odot$  on the SGB. BaSTI isochrones spaced by 20 Myr in age were specifically calculated for this work.

Figure 4.1 shows the  $m_{\text{F555W}} - m_{\text{F814W}}$  vs.  $m_{\text{F814W}}$  CMD of NGC 1978 with a BaSTI isochrone superimposed as a solid violet line. The chosen parameters are the following: (i) age = 2 Gyr, (ii) metallicity  $[\text{Fe}/\text{H}] = -0.35$  dex, and (iii) distance modulus  $\text{DM} = 18.55$  mag, (iv) extinction value  $A_V = 0.16$  mag. The isochrone in Fig. 4.1 nicely reproduces the shape of the  $m_{\text{F555W}} - m_{\text{F814W}}$  vs.  $m_{\text{F814W}}$  CMD in all its evolutionary stages. The adopted metallicity is consistent with results by [Ferraro et al. \(2006\)](#), who

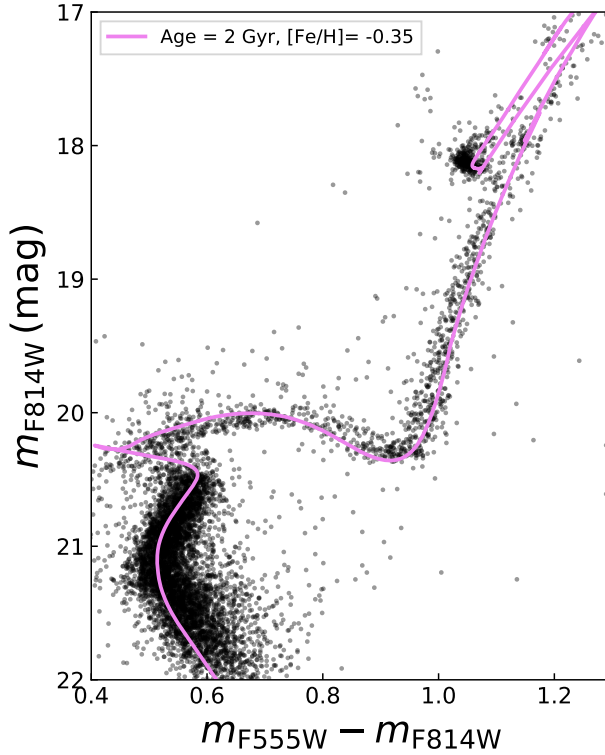


Figure 4.1:  $m_{\text{F}555\text{W}} - m_{\text{F}814\text{W}}$  vs.  $m_{\text{F}814\text{W}}$  CMD of NGC 1978. The violet curve indicates the BaSTI isochrone for values of age = 2 Gyr and metallicity  $[\text{Fe}/\text{H}] = -0.35$  dex. The adopted distance modulus and extinction values are  $\text{DM} = 18.55$  mag and  $A_V = 0.16$  mag, respectively.

found an iron content of  $[\text{Fe}/\text{H}] = -0.38$  dex by analysing 11 high-resolution FLAMES spectra of giant stars in NGC 1978.

Additionally, [Mucciarelli et al. \(2007\)](#) performed an isochrone fitting of the ACS  $m_{\text{F}555\text{W}} - m_{\text{F}814\text{W}}$  vs.  $m_{\text{F}555\text{W}}$  CMD of NGC 1978 by adopting several sets of isochrones. They measured the age of the cluster to be  $1.9 \pm 0.1$  Gyr, which is consistent with the age we adopt.

### 4.1.1 Artificial stars test

We performed artificial star (AS) experiments following the method described in [Dalessandro et al. \(2015\)](#) (see also [Bellazzini et al. 2002; Dalessandro et al. 2016](#)) to derive a reliable estimate of the photometric errors. AS were performed for the entire data-set adopted in the present paper. In particular, we note that they are especially

critical for both the F555W and F814W bands as only one image is available for these filters.

We generated a catalog of simulated stars with an F814W-band input magnitude ( $F814W_{in}$ ) extracted from a luminosity function (LF) modeled to reproduce the observed LF in that band and extrapolated beyond the observed limiting magnitude. We then assigned a  $F336W_{in}$ ,  $F343N_{in}$ ,  $F438W_{in}$  and  $F555W_{in}$  magnitudes to each star extracted from the luminosity function, by means of an interpolation along the ridge mean lines that were obtained in different CMDs by averaging over 0.4 mag bins and applying a  $2\sigma$  clipping algorithm.

Artificial stars were added to real images (which include also real stars) by using the software DAOPHOTII/ADDSTAR (Stetson, 1987). Then, the photometric analysis was performed using the same reduction strategy and PSF models used for real images (see Chapter 2, §2.2.1 for details) on both real and simulated stars. In this way, the effect of radial variation of crowding on both completeness and photometric errors is accounted for. Artificial crowding was minimized by placing stars into the images following a regular grid composed by  $25 \times 25$  pixel cells in which only one artificial star for each run was allowed to lie at a random position within the cell. For each run, we simulated in this way  $\sim 14,000$  stars. The procedure was repeated several times until a minimum number of 100,000 was added to each ACS (for F555W and F814W) or WFC3 (for F343N, F336W and F438W) chip. At each run the positions of the simulated stars are randomly changed. After a large number of experiments, stars are uniformly distributed in coordinates. Stars recovered after the AS photometric analysis have values of  $F336W_{out}$ ,  $F343N_{out}$ ,  $F438W_{out}$ ,  $F555W_{out}$  and  $F814W_{out}$ .

The AS catalog was then used to derive photometric errors for SGB and MS stars, applied in the following analysis (see Sections §4.2, §4.3, §4.4). Errors were derived computing the r.m.s. of the distributions of simulated stars in the  $(mag_{in}, mag_{in} - mag_{out})$  diagrams for all available bands in different magnitude bins and after applying the same selections in the photometry quality indicators (sharpness and chi) that were originally applied to the data (§2.2.1, §3.1). The distribution of the average errors as a function of the distance from the cluster centre for all the considered bands is

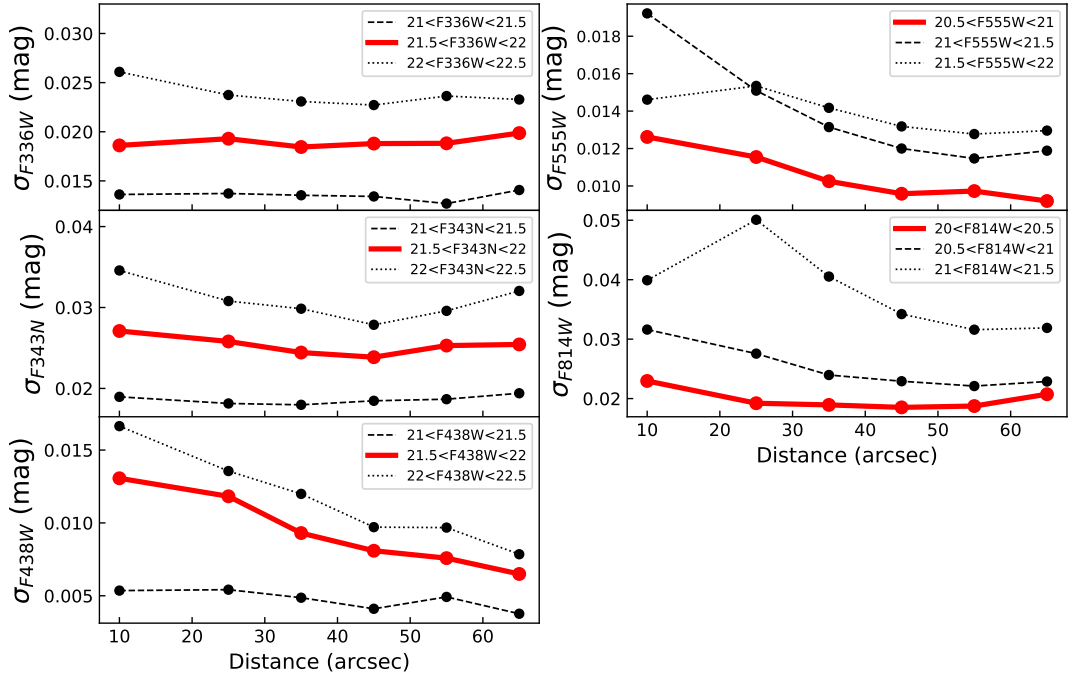


Figure 4.2: Photometric errors for the F336W, F343N, F438W, F555W, F814W filter bands as a function of the distance from the cluster centre. This is shown for three bins of magnitude in each panel. The red line indicates the magnitude bin corresponding to the SGB.

shown in Figure 4.2. As expected, in the optical images (F438W, F555W and F814W) where crowding is stronger, errors progressively decrease moving towards the external regions of the cluster as crowding becomes less and less severe. On the contrary we do not observe any significant variation in the UV filters (F343N and F336W).

## 4.2 SGB stars selection

Firstly, we selected SGB stars in the  $m_{\text{F555W}} - m_{\text{F814W}}$  vs.  $m_{\text{F814W}}$  CMD of NGC 1978, as the SGB and MS overlap in UV filters. Fig. 4.3 shows the  $m_{\text{F555W}} - m_{\text{F814W}}$  vs.  $m_{\text{F814W}}$  CMD of NGC 1978, with black filled circles marking the first selection of SGB stars.

We plotted the first selection of SGB stars in the  $m_{\text{F343N}} - m_{\text{F438W}}$  vs.  $m_{\text{F438W}}$  CMD (left panel of Fig. 4.4). We then made the final selection along the relatively vertical part of the SGB, where there is a visible split in the observed sequence. Red filled

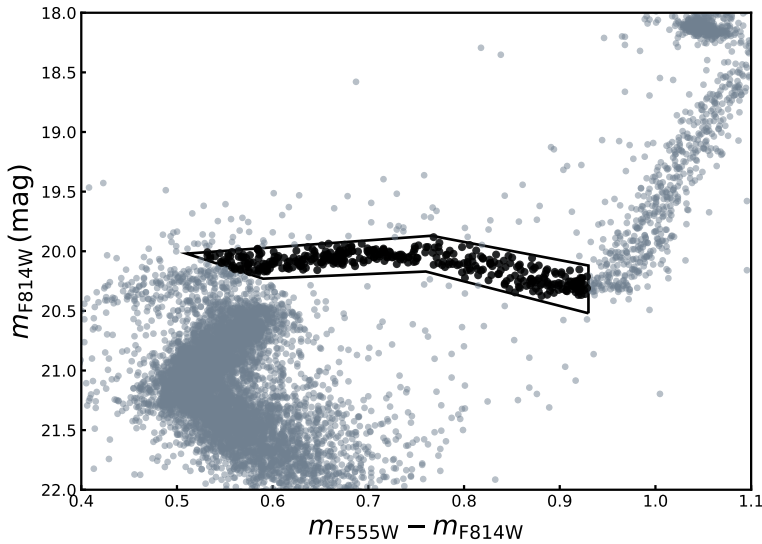


Figure 4.3:  $m_{\text{F}555\text{W}} - m_{\text{F}814\text{W}}$  vs.  $m_{\text{F}814\text{W}}$  CMD of NGC 1978. The black box indicates the locus of the initial selection of SGB stars which are marked by black filled circles.

circles mark the final selected SGB stars in the left panel of Fig. 4.4. Such a selection was made since we expect a split in this region of the SGB, as we will show later on in this Section (see Fig. 4.6).

According to the isochrone describing the shape of the SGB in UV filters (Fig. 4.6), we defined a fiducial line on the blue part of the selected SGB stars in the  $m_{\text{F}343\text{N}} - m_{\text{F}438\text{W}}$  vs  $m_{\text{F}438\text{W}}$  CMD and this is displayed in the right panel of Fig. 4.4 as a solid red line. Black filled circles represent the final selected SGB stars in this figure. Next, we calculated the distance in  $m_{\text{F}343\text{N}} - m_{\text{F}438\text{W}}$  colours of each SGB star from the fiducial line,  $\Delta(m_{\text{F}343\text{N}} - m_{\text{F}438\text{W}})$ . Next, we fit the unbinned verticalised  $\Delta(m_{\text{F}343\text{N}} - m_{\text{F}438\text{W}})$  data with two-component Gaussian Mixture Models (GMMs) to identify the presence of multiple Gaussian components in the colour distribution. We fit the data with the SCIKIT-LEARN python package called MIXTURE<sup>1</sup> (see Chapter 3, §3.2). The result of the fit is shown as a solid black line in the top panel of Fig. 4.5 over the histogram of the distribution in  $\Delta(m_{\text{F}343\text{N}} - m_{\text{F}438\text{W}})$  colours. For comparison, we also show the non-parametric Kernel Density Estimate (KDE) to the unbinned data as a green curve. The blue (red) dashed curve represents the first (second) Gaussian component in the fit. We will refer to the blue component as representative of a first

<sup>1</sup><http://scikit-learn.org/stable/modules/mixture.html>

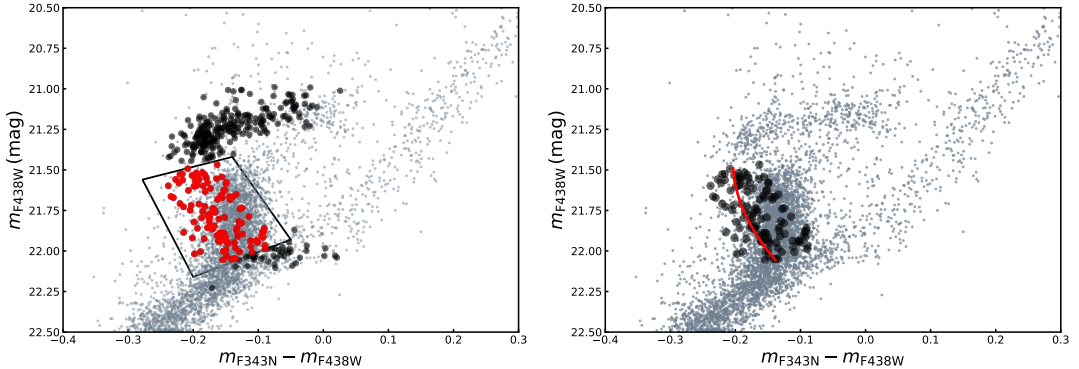
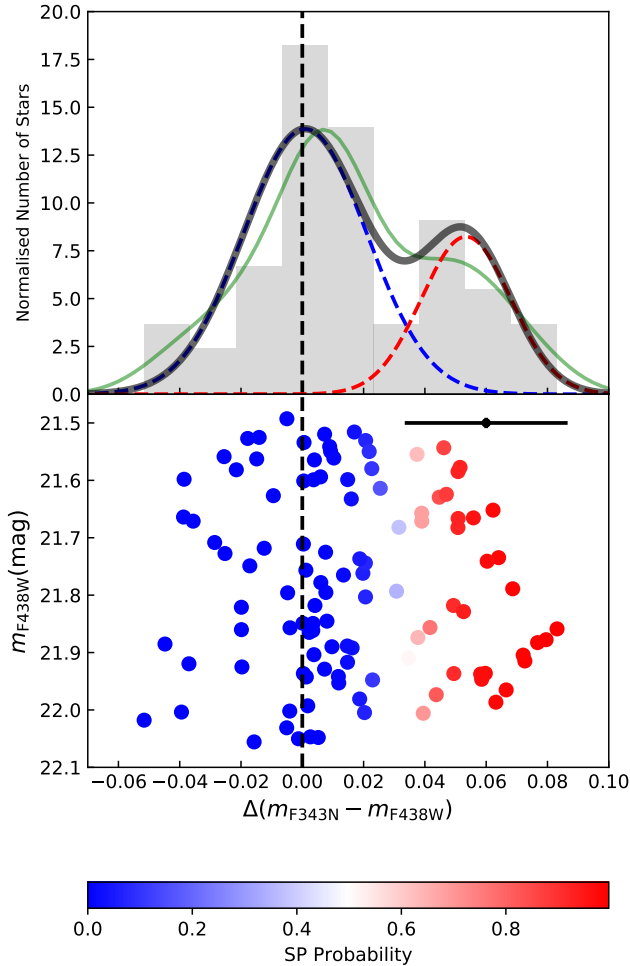


Figure 4.4:  $m_{\text{F}343\text{N}} - m_{\text{F}438\text{W}}$  vs  $m_{\text{F}438\text{W}}$  CMDs of NGC 1978. *Left Panel:* Red filled circles indicate the final selected SGB stars, while black circles represent the stars that did not pass the final selection. *Right Panel:* Black circles mark the final selected SGB stars. The red solid line indicates the fiducial line defined on the edge of the SGB.

population (FP) in the cluster, and to the red component as representative of a second population (SP).

For each star, we assigned a probability to belong to the FP and to the SP by using the respective Gaussian function found by the GMM fit. The bottom panel of Fig. 4.5 shows the  $\Delta(m_{\text{F}343\text{N}} - m_{\text{F}438\text{W}})$  colours vs.  $m_{\text{F}438\text{W}}$ , where the stars are colour coded by the probability to belong to the SP. The black dashed vertical line marks the adopted fiducial line.

The left panel of Fig. 4.6 shows the  $m_{\text{F}343\text{N}} - m_{\text{F}438\text{W}}$  vs.  $m_{\text{F}438\text{W}}$  CMD of the SGB stars in NGC 1978. Final SGB selected stars are indicated with black filled circles. We compare our data with three isochrones superimposed. We extensively described how our stellar N-enriched isochrones are built in Chapter 2, §2.2.4. The blue solid, green dashed, red dotted curves represent theoretical isochrones, derived by using the 2.2 Gyr, [Fe/H]=-0.5 dex MIST isochrone (Dotter, 2016; Choi et al., 2016), for three different chemical abundance mixtures, denominated as solar ([C/Fe]=[O/Fe]=[N/Fe]=0 dex), intermediate ([C/Fe]=[O/Fe]= -0.1 dex, [N/Fe]= +0.5 dex) and enriched ([C/Fe]=[O/Fe]= -0.6 dex, [N/Fe]= +1.0 dex) models, respectively. For the N-enhanced isochrones, the choice of C and O abundances were chosen to keep the [(C+N+O)/Fe] constant between the models, according to what is observed in GCs (e.g. Carretta et al. 2005).



**Figure 4.5:** *Top Panel:* Histogram of the distribution of selected SGB stars in NGC 1978, in  $\Delta(m_{\text{F}343\text{N}} - m_{\text{F}438\text{W}})$  colours. The black solid line represents the two-component GMM best-fit function to the unbinned data. The blue (red) dashed curve represents the first (second) Gaussian component in the fit. The green curve indicates the Kernel Density Estimator (KDE). *Bottom Panel:*  $\Delta(m_{\text{F}343\text{N}} - m_{\text{F}438\text{W}})$  vs.  $m_{\text{F}438\text{W}}$  is shown, where stars are colour coded by the probability to belong to the SP. The black dashed vertical line marks the adopted fiducial line. The black errorbar shown in the bottom panel represents the typical error in  $\Delta(m_{\text{F}343\text{N}} - m_{\text{F}438\text{W}})$  colours and  $m_{\text{F}438\text{W}}$  magnitudes. The error on the  $m_{\text{F}438\text{W}}$  magnitude is smaller than the black filled circle.

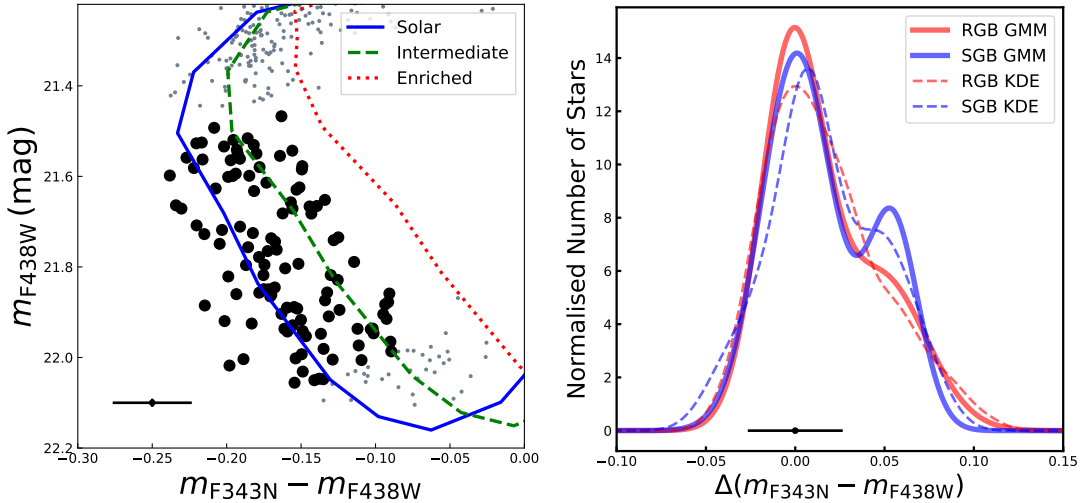


Figure 4.6: *Left panel:* SGB stars in the  $m_{\text{F}343\text{N}} - m_{\text{F}438\text{W}}$  vs.  $m_{\text{F}438\text{W}}$  CMD for NGC 1978. The final SGB selected stars are marked with black filled circles. The solid blue, dashed green and dotted red curves represent our stellar atmosphere models from the 2.2 Gyr,  $[\text{Fe}/\text{H}] = -0.5$  dex MIST isochrone by using solar ( $[\text{C}/\text{Fe}] = [\text{O}/\text{Fe}] = [\text{N}/\text{Fe}] = 0$  dex), intermediate ( $[\text{C}/\text{Fe}] = [\text{O}/\text{Fe}] = -0.1$  dex,  $[\text{N}/\text{Fe}] = +0.5$  dex) and enriched ( $[\text{C}/\text{Fe}] = [\text{O}/\text{Fe}] = -0.6$  dex,  $[\text{N}/\text{Fe}] = +1.0$  dex) chemical abundance mixtures, respectively. *Right panel:* Two-component GMM best-fit function to the unbinned  $\Delta(m_{\text{F}343\text{N}} - m_{\text{F}438\text{W}})$  colours. The red curve is calculated for the selected RGB stars (Chapter 3, §3.1.2), while the blue curve represents the fit to the SGB stars which were selected in this work (see Fig. 4.5). A systematic offset has been applied to the  $\Delta(m_{\text{F}343\text{N}} - m_{\text{F}438\text{W}})$  colours of the RGB such that the GMM’s main peak coincided with the SGB GMM. The black errorbar shown in both panels represents the typical error in  $\Delta(m_{\text{F}343\text{N}} - m_{\text{F}438\text{W}})$  colours and  $m_{\text{F}438\text{W}}$  magnitudes. The error on the  $m_{\text{F}438\text{W}}$  magnitude is smaller than the black filled circle. The red (blue) dashed line represents the KDE for the RGB (SGB) selected stars.

The observed split in the SGB of the  $m_{\text{F}343\text{N}} - m_{\text{F}438\text{W}}$  vs.  $m_{\text{F}438\text{W}}$  CMD is consistent with expectations from theoretical isochrones. Fig. 4.6 reveals that a clear split is expected in  $m_{\text{F}343\text{N}} - m_{\text{F}438\text{W}}$  colours if chemical variations are present in the SGB, which is consistent to what we observe in the data. Note that for  $m_{\text{F}438\text{W}} \lesssim 21.5$  the split in the SGB is less evident and the isochrones tend to merge for smaller magnitudes, while for  $m_{\text{F}438\text{W}} \gtrsim 22.1$  models with different abundance mixtures intersect. This explains the adopted selection which includes only the relatively vertical part of the SGB. Additionally, based on the RGB analysis (Chapter 3, §3.1.2), NGC 1978 is expected to have an intermediate N-enrichment ( $[\text{N}/\text{Fe}] = +0.5$  dex), which is the same enrichment we obtain when comparing data to the isochrones with different chemical mixtures in the SGB (Fig. 4.6).

The right panel of Fig. 4.6 shows the two-component GMM best-fit function to the unbinned  $\Delta(m_{F343N} - m_{F438W})$  colours for both RGB (red curve) and SGB (blue curve) stars. Also, the comparison among the KDEs is shown. It is clear from this figure that both SGB and RGB show the same broadness in  $\Delta(m_{F343N} - m_{F438W})$  colours and very similar GMM best-fit distributions and KDEs.

## 4.3 SGB Analysis

As a first step, we plotted the SGB selected stars (see §4.2) on the  $m_{F555W} - m_{F814W}$  vs.  $m_{F814W}$  CMD. This is shown in the left panel of Fig. 4.7, where stars are colour-coded by the probability to belong to the SP. In this filter combination, no spreads or split are expected due to the presence of MPs (e.g., [Sbordone et al. 2011](#)). In optical filters, the SGB is expected not to be sensitive to MPs assuming that the CNO sum is constant, however the magnitude of the SGB is a strong function of age, hence if there is an age difference between the FP and SP, their SGB magnitudes should differ (e.g., [Li, de Grijs & Deng 2014](#)). Star-to-star variations of He abundance might generate an offset on the SGB as well. However, significant He spreads in standard GCs are usually associated with a large N enrichment (e.g., [Milone et al. 2015](#), [Milone et al. 2017](#)). Assuming that young star clusters behave as old GCs, no remarkable He spreads are to be expected in NGC 1978, as the N enhancement in NGC 1978 appears to be small (Chapter 3, §3.2.1).

A first look at the left panel of Fig. 4.7 reveals that no clear and visible offset is observed between the two populations. In order to better quantify the presence of a possible offset, we defined a fiducial line on the 2 Gyr,  $[Fe/H] = -0.35$  dex BaSTI isochrone on the SGB (Fig. 4.1). This is shown as a black solid curve in both panels of Fig. 4.7. We calculated the distance in  $m_{F814W}$  magnitudes of each SGB star from the fiducial line,  $\Delta(m_{814W})$ . Then, we calculated the weighted mean in  $\Delta(m_{814W})$  for the FP and SP by using the probability to belong to the FP and SP as weights. Our observed age difference between the two populations, in units of magnitude, results to be  $\Delta Mag_{OBS} \equiv <\Delta m_{FP}> - <\Delta m_{SP}> = 0.0027$  mag for the  $m_{F555W} - m_{F814W}$  vs.

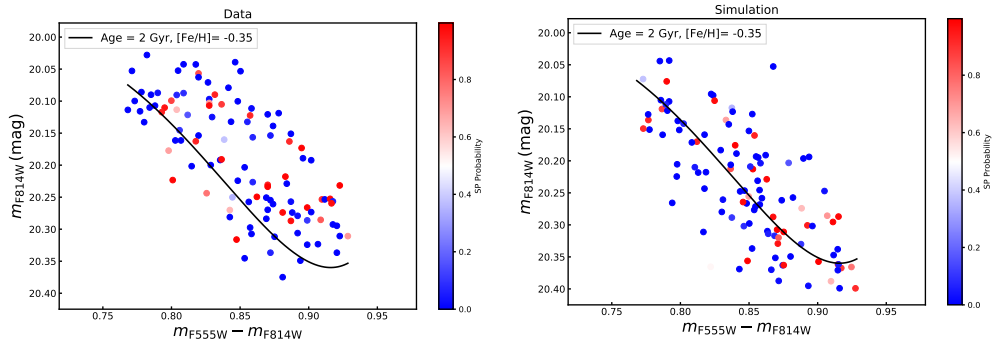


Figure 4.7: *Left panel:* SGB selected stars in the  $V - I$  vs.  $I$  CMD for NGC 1978 (left panel) and MC simulation of our SGB data, where observational errors are taken into account (right panel). Stars are colour-coded according to the probability of belonging to the SP. The black solid line indicates the defined fiducial line on the 2 Gyr,  $[Fe/H] = -0.35$  dex BaSTI isochrone on the SGB (Fig. 4.1).

$m_{F814W}$  CMD.

Hence, we can compare the observed age difference in magnitude to isochrones in the SGB to obtain the age difference in units of Myr. As discussed in §4.1, we used BaSTI isochrones. The left panel of Fig. 4.8 shows the isochrones we used for the calculation, from age = 1.94 Gyr up to 2.08 Gyr, spaced by 20 Myr. Two vertical dashed lines mark the selected region of the SGB where we performed the calculation, corresponding to the observed section of the SGB where the split is seen in UV colours. Firstly, we used the 2 Gyr isochrone as an age reference for NGC 1978 (see Fig. 4.1). We then calculated the mean difference in  $m_{F814W}$  magnitudes between the 2 Gyr isochrone and the other isochrones (displayed in Fig. 4.8), in the SGB. In this way, we can transform the observed difference in magnitude to age differences (defined as  $\Delta\text{Age}$ ).

These values are reported in the right panel of Fig. 4.8. Next, we fit the values with a linear relation and we found the following:

$$(\Delta\text{Age}/\text{Myr}) = 1801.37 \times (\Delta\text{Mag}/\text{mag}) - 3.46. \quad (4.1)$$

The best-fit is shown as a red solid line in the right panel of Fig. 4.8. We then used this relation to convert our observed ( $\Delta\text{Mag}_{OBS}$ ) value into age differences in Myr between the two populations.

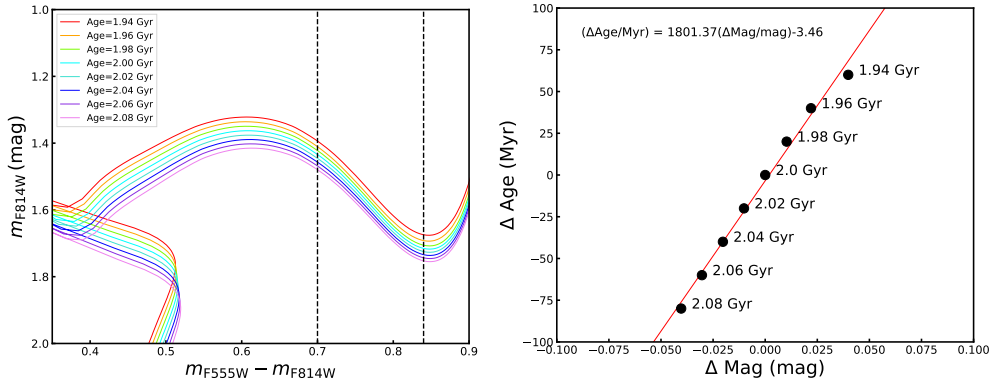


Figure 4.8: *Left Panel:* BaSTI isochrones in the  $m_{\text{F}555\text{W}} - m_{\text{F}814\text{W}}$  vs.  $m_{\text{F}814\text{W}}$  CMD with ages ranging from 1.94 up to 2.08 Gyr, spaced by 20 Myr ( $[\text{Fe}/\text{H}] = -0.35$  dex). The vertical black dashed lines highlight the SGB region used to calculate the expected and observed age differences between the two populations. *Right Panel:*  $\Delta \text{Mag}$  vs.  $\Delta \text{Age}$  relation (red solid line) for the SGB when the isochrones in the left panel are taken into account. See text for more details.

We found that the age difference in the  $m_{\text{F}555\text{W}} - m_{\text{F}814\text{W}}$  vs.  $m_{\text{F}814\text{W}}$  CMD between the FP and SP is 1.4 Myr.

We used Monte Carlo (MC) simulations to estimate the uncertainty of this result. Ideally, we would sample stars from two separate isochrones for the FP and SP and calculate the inferred age difference with respect to the input age difference assuming that the magnitude spread of each population is solely due to the photometry uncertainties. However, the measured value of 1.4 Myr is much smaller than the age resolution of the isochrone grid (20 Myr) and by all means consistent with null intrinsic spread. In this situation we need to investigate the level of stochasticity introduced in this result due to the limited number of available stars. Thus, we sampled from a single isochrone model the same number of stars as the ones used in the fit, using their photometric errors, assigned to them the same probability distribution of belonging to the FP and the SP as in the real data, and repeated this process 100,000 times. The right panel of Fig. 4.7 shows an example of a simulation, which appears to well reproduce our observations. According to Fig. 4.2, we considered as photometric errors for the  $m_{\text{F}555\text{W}}$  and  $m_{\text{F}814\text{W}}$  filters, the values of  $\sigma(m_{\text{F}555\text{W}})$  and  $\sigma(1)$  found for the inner centre of the cluster ( $r < 10''$ ), which also correspond to the maximum values as a function of distance. We found that the Monte Carlo distribution has a mean of 0 mag, as expected, and

$\sigma = 0.013$  mag, that corresponds to an age difference of 19.9 Myr (by using Eq. 4.1).

We found that the age difference between the two populations in the SGB is then  $1 \pm 20$  Myr, which is consistent with zero. If different stellar isochrones are used, we obtain similar constraints. When the MIST models are used (however with a resolution of 40 Myr), we find a measured difference of  $5 \pm 29$  Myr. This is an extremely tight constraint for the origin of MPs and it shows that the two populations have essentially the same age. We will discuss this in detail in §4.5.

We repeated the analysis described above, using the  $m_{\text{F438W}} - m_{\text{F814W}}$  vs.  $m_{\text{F814W}}$  CMD. In this case, the observed age difference between the two populations, in units of magnitude, is  $\Delta\text{Mag}_{\text{OBS}} = 0.0017$  mag. From the simulations, the expected magnitude difference between the two populations is a Gaussian with peak at zero and a  $\sigma = 0.01$  mag. By comparison with  $m_{\text{F438W}} - m_{\text{F814W}}$  vs.  $m_{\text{F814W}}$  BaSTI isochrones, we found that the age difference between FP and SP is consistent with zero, being  $0.5 \pm 14.7$  Myr when an age of 2 Gyr is considered as a reference for the calculation.

One may argue that absolute cluster ages are not well-known due to the degeneracy established by the numerous parameters involving the isochrone fitting. In this case, as a further test for our results, we adopted two other ages as reference age. We did the same isochrone comparison by using an age of 2.5 Gyr and 1.8 Gyr. We then calculated the linear relations among  $\Delta\text{Mag}$  and  $\Delta\text{Age}$  and computed the age difference in Myr between FP and SP by using these new best-fits. We still found that the age difference is consistent with the results from our original experiment.

## 4.4 The Main Sequence Turnoff

In this Section, we will outline the analysis of the MSTO width of NGC 1978.

We selected MS stars in the  $m_{\text{F555W}} - m_{\text{F814W}}$  vs.  $m_{\text{F814W}}$  CMD. Fig. 4.9 shows the  $m_{\text{F555W}} - m_{\text{F814W}}$  vs.  $m_{\text{F814W}}$  CMD of NGC 1978 with black filled circles indicating

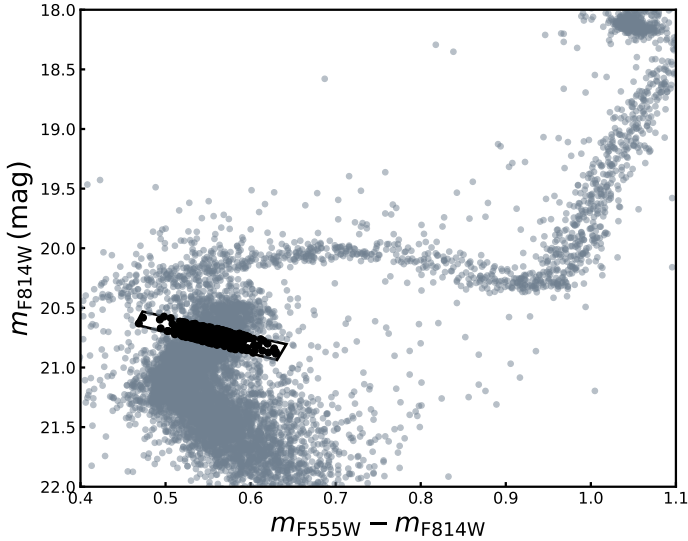


Figure 4.9:  $m_{\text{F}555\text{W}} - m_{\text{F}814\text{W}}$  vs.  $m_{\text{F}814\text{W}}$  CMDs of NGC 1978. The black box indicates the locus of the selection of MS stars, marked by black filled circles.

the MS selected stars. Next, we defined a fiducial line in the  $m_{\text{F}555\text{W}} - m_{\text{F}814\text{W}}$  vs.  $m_{\text{F}814\text{W}}$  space. We calculated the distance in  $m_{\text{F}555\text{W}} - m_{\text{F}814\text{W}}$  colours of each star from the fiducial line,  $\Delta(m_{\text{F}555\text{W}} - m_{\text{F}814\text{W}})$ . The left panel of Fig. 4.10 displays the histogram of the distribution of the selected MS stars in  $\Delta(m_{\text{F}555\text{W}} - m_{\text{F}814\text{W}})$  colours. The blue solid line indicates a Gaussian function centred at zero and with  $\sigma = 0.028$ , which represents the error in  $\Delta(m_{\text{F}555\text{W}} - m_{\text{F}814\text{W}})$  colours obtained from the AS experiment by applying the same selection box that was used for the data (Fig. 4.9). This comparison immediately shows that the observed spread in the MS  $m_{\text{F}555\text{W}} - m_{\text{F}814\text{W}}$  colours can be entirely attributed to observational errors.

Next, we used mock samples from theoretical isochrones in order to compare the MSTO width of the data with simulations. Thus, we can derive an upper limit on the age spread hidden in the observational errors. We randomly sampled 10,000 stars from the 2 Gyr BaSTI isochrone (Fig. 4.1) in the MSTO region<sup>2</sup>, by adding observational errors both in magnitude and colours. We then applied to the simulation the same selection cut applied to the data (Fig. 4.9). For this set of data, we estimated the distance in  $m_{\text{F}555\text{W}} - m_{\text{F}814\text{W}}$  colours of each star from the isochrone,  $\Delta(m_{\text{F}555\text{W}} - m_{\text{F}814\text{W}})$ ; finally, we calculated the standard deviations of stars in  $\Delta(m_{\text{F}555\text{W}} - m_{\text{F}814\text{W}})$  colours,

<sup>2</sup>Random stars were sampled in the colour-magnitude space  $0.42 \lesssim (m_{\text{F}555\text{W}} - m_{\text{F}814\text{W}}) \lesssim 0.62$ ,  $20.4 \lesssim m_{\text{F}814\text{W}} \lesssim 21.1$ .

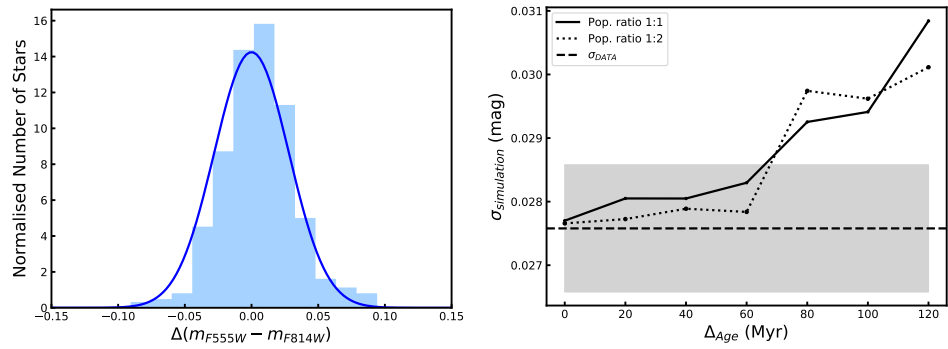


Figure 4.10: *Left panel:* Histogram of the distribution of the selected MS stars in  $\Delta(m_{F555W} - m_{F814W})$  colours. The blue solid line indicates a Gaussian function centred at zero and with  $\sigma = 0.028$ , which represents the observational error obtained from the AS test. *Right panel:*  $\Delta_{\text{Age}}$  as a function of  $\sigma_{\text{simulation}}$  for a population ratio of 1:1 (black solid line) and 1:2 (black dotted line). The black dashed line indicates the value of  $\sigma_{\text{DATA}}$ , while the gray shaded area marks the uncertainty on  $\sigma_{\text{DATA}}$ . See text for more details.

namely  $\sigma_{\text{simulation}}$ . We then did this analysis by sampling 10,000 random stars from the 2 Gyr BaSTI isochrone and 10,000 star from another isochrone simultaneously, imitating two populations separated in age by  $\Delta(\text{age})$ . We repeated this with isochrones spaced by 20, 40, 60, 80, 100 and 120 Myr. Each simulation was treated in exactly the same way as the observations. We calculated  $\sigma_{\text{simulation}}$  for each sample and we show  $\Delta_{\text{Age}}$  as a function of  $\sigma_{\text{simulation}}$  in the right panel of Fig. 4.10. We calculated our  $\sigma_{\text{DATA}}$  from the  $\Delta(m_{F555W} - m_{F814W})$  colours for a direct comparison. This value is shown as a black dashed line in the right panel of Fig. 4.10. The gray shaded area marks the uncertainty on  $\sigma_{\text{DATA}}$ , which was calculated on the unbinned data by using a bootstrap technique (Efron & Tibshirani, 1993) based on 10,000 realizations.

By making a comparison between  $\sigma_{\text{DATA}}$  and  $\sigma_{\text{simulation}}$  (right panel of Fig. 4.10), we can put an upper limit of  $\sim 65$  Myr to an age spread on the MSTO of NGC 1978, at  $2\sigma$  confidence level. We discuss this result in detail in §4.5.

Additionally, based on the results by Goudfrooij et al. (2011), we repeated the same simulations when considering a population ratio of 1:2, i.e. by sampling 10,000 random stars for the younger population and 5,000 stars for the older population. This is shown as a black dotted line in the right panel of Fig. 4.10 and it is consistent with what we found with a 1:1 population ratio. However, we note that this scenario would be inconsistent with the AGB scenario due to the mass-budget problem (e.g., Bastian

& Lardo 2018).

## 4.5 Discussion

The aim of this Chapter was to exploit the unique characteristics of NGC 1978 to place stringent constraints on the presence of a spread in age amongst its multiple constituent stellar populations.

We took advantage of the structure of its SGB to estimate the age difference between the two subpopulations present in NGC 1978. We find an age difference between the two populations of  $1 \pm 20$  Myr, when the  $m_{\text{F}555\text{W}} - m_{\text{F}814\text{W}}$  vs.  $m_{\text{F}814\text{W}}$  CMD is taken into account. If we repeat the same analysis by taking into account the  $m_{\text{F}438\text{W}} - m_{\text{F}814\text{W}}$  vs.  $m_{\text{F}814\text{W}}$  CMD we find an age difference of  $0.5 \pm 14.7$  Myr (§4.3).

From this analysis, it emerges that the two populations present in NGC 1978 have the same age, or at most their age difference is very little.

Such results establish very tight constraints on the onset of multiple populations and provide limits on the nature of the polluters.

Models for the origin of multiple populations which adopt multiple generations of star-formation using AGB stars as the source of polluting material, predict an age difference of at least 30 Myr between the 1st and 2nd populations, potentially being as large as 200 Myr. Our results show instead that the FP and SP in NGC 1978 formed at the same time or very close to each other, creating significant tension with predictions from this family of models.

Currently all models put forward for the nature of multiple populations present serious drawbacks in reproducing the very complicated details provided by the observations (Bastian, Cabrera-Ziri & Salaris 2015, Renzini et al. 2015, Prantzos, Charbonnel & Iliadis 2017, Bastian & Lardo 2018). However, the results presented here support a scenario where no multiple bursts of star formation are invoked or that they happened nearly concurrently, i.e. abundance anomalies are not originated by means of multiple

generations created over a large time separation.

Additionally, we estimated the broadness of the MSTO of NGC 1978. While most LMC and SMC clusters studied to date, aged less than 2 Gyr, clearly show an extended MSTO (e.g. Chapter 1, §1.4, Mackey et al. 2008; Milone et al. 2009), we find that NGC 1978 does not show a prominent eMSTO, i.e. the observed spread in the TO is comparable with photometric errors (§4.4). We can put an upper limit of  $\sim$ 65 Myr to the age spread in the MSTO.

The origin of the eMSTO in young star clusters is strongly debated in the community. However, NGC 1978 is a peculiar and interesting case which might lead to a major breakthrough. The nature of the eMSTO was originally explained by the presence of age spreads of the order of 200-700 Myr within a cluster. Such age spreads, perhaps related to the cluster's high escape velocity (Goudfrooij et al., 2014), require the occurrence of multiple bursts of star formation over an extended period within the cluster.

Bastian & de Mink (2009) proposed that alternatively the eMSTO may be caused by a range of stellar rotation rates in a single-aged population. Predictions and comparisons with observations for the stellar rotation scenario were made by studying eMSTO populations of both intermediate age (Brandt & Huang, 2015) and young massive clusters (YMCs, Niederhofer et al. 2015). The latter found the so-called  $\Delta(\text{Age})$  vs. Age relation, i.e. the expected/inferred age spread within a cluster is directly proportional to the age of the cluster (Fig. 1.7). This trend was also corroborated at younger ages (Milone et al., 2015; Bastian et al., 2016) and it is in good agreement with predictions of the stellar rotation scenario. Such a relation and the results presented here are clearly at odds with predictions of the age spread scenario as the origin of the eMSTO.

We find that chemical abundance variations are present in the RGB of NGC 1978, whereas no MPs are detected in YMCs or intermediate age clusters that show prominent eMSTOs (< 2 Gyr, e.g. Mucciarelli et al. 2014; Cabrera-Ziri et al. 2016b; Martocchia et al. 2017, 2018a). Among these we can find the SMC cluster NGC 419, which has very similar properties to NGC 1978 (mass, radius), but it is  $\sim$ 500 Myr younger and show one of the largest eMSTO.

On the contrary, we do not expect the presence of an eMSTO in NGC 1978 according to the stellar rotation scenario. [Brandt & Huang \(2015\)](#) explicitly predicted a turnover in the distribution, so that by an age of  $\sim 2$  Gyr the eMSTO should disappear (in the rotation scenario) which agrees with the results presented here. Stellar masses for TO stars at this age ( $\sim 2$  Gyr) drop below  $1.5 M_{\odot}$ , such that stars are magnetically braked and become slow rotators. This is fully consistent with the observations, thus the work reported in this Chapter support a scenario where the eMSTO is caused by a stellar rotation effect.

# Chapter 5

## Correlation between cluster age and abundance spreads

So far, our initial sample had a gap between 2 and 6 Gyr and it also focussed on clusters with mass  $\gtrsim 10^5 M_\odot$ . In the current Chapter, we present a photometric study and search for MPs in four additional clusters in the MCs, namely NGC 2121, NGC 2155, Lindsay 38 and Lindsay 113, for which we obtained new HST UV observations. For a list of the observations used, see Table 2.3. These clusters were chosen to sample the parameter space missed in our previous observations: they have ages between  $\sim 2.5$  and  $\sim 6.5$  Gyr and masses  $M \lesssim 10^5 M_\odot$ . We constrained the presence and amplitude of N abundance variations by analysing their RGB widths, consistently with what was done in Chapter 2, 3. Results are compared with what was obtained for the other clusters of the survey and for Galactic GCs (namely 47 Tuc, M15 and NGC 2419) in Section §5.2. For the photometric data reduction and calculation of AS catalogues we refer to Chapter 2, §2.2.1 and Chapter 4, §4.1.1, respectively. The results presented in this Chapter are based on the work published in [Martocchia et al. \(2019\)](#).

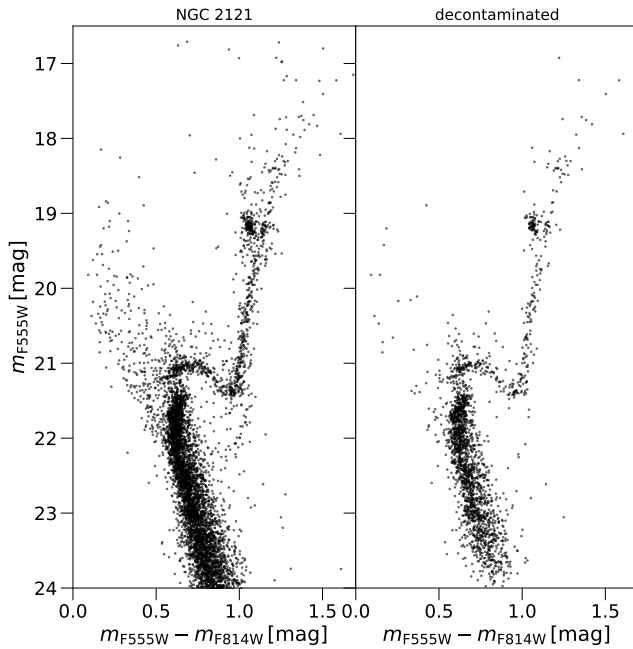


Figure 5.1:  $m_{F555W} - m_{F814W}$  vs.  $m_{F555W}$  CMD of NGC 2121 before (left panel) and after (right panel) the field star subtraction.

## 5.1 Analysis

For NGC 2121, NGC 2155 and Lindsay 113, the analysis presented in this Chapter was performed in a circular region around the cluster centre (the “cluster region”). Stars were selected within a radius of 40 arcsec from the centre of NGC 2121 and NGC 2155 and within a radius of 45 arcsec from the centre of Lindsay 113<sup>1</sup>. The centre of each cluster was estimated by fitting a two-dimensional Gaussian to the distribution of the stellar density. For NGC 2121 and NGC 2155, we performed a statistical de-contamination analysis to use likely cluster members. For the background subtraction technique we refer to Chapter 2, §2.2.2. Figure 5.1 shows the  $m_{F555W} - m_{F814W}$  vs.  $m_{F555W}$  CMD of NGC 2121 before (left panel) and after (right panel) the field star subtraction, while Fig. 5.3 reports the  $m_{F336W} - m_{F438W}$  vs.  $m_{F438W}$  CMDs of NGC 2121 and NGC 2155 before and after the decontamination.

Field stars were not subtracted in Lindsay 38 and Lindsay 113 since it was not possible

<sup>1</sup>The radii of the clusters were selected to maximise the areas of the background and cluster regions at the same time, avoiding overlap between the two.

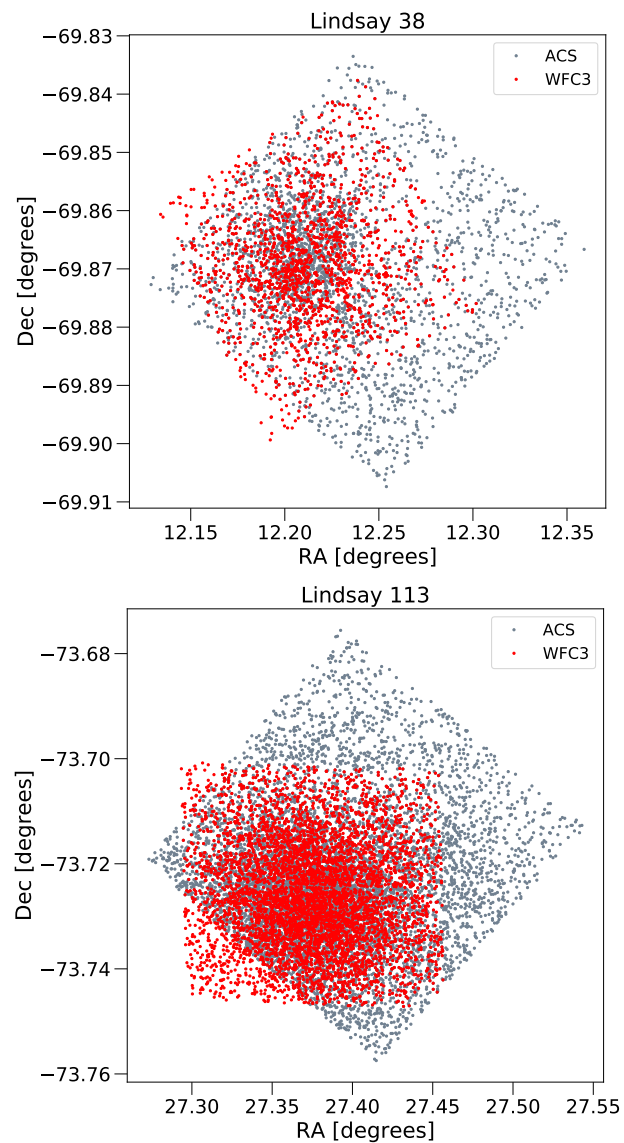


Figure 5.2: ACS(grey) and WFC3(red) map for Lindsay 38 (top) and Lindsay 113 (bottom) FOV.

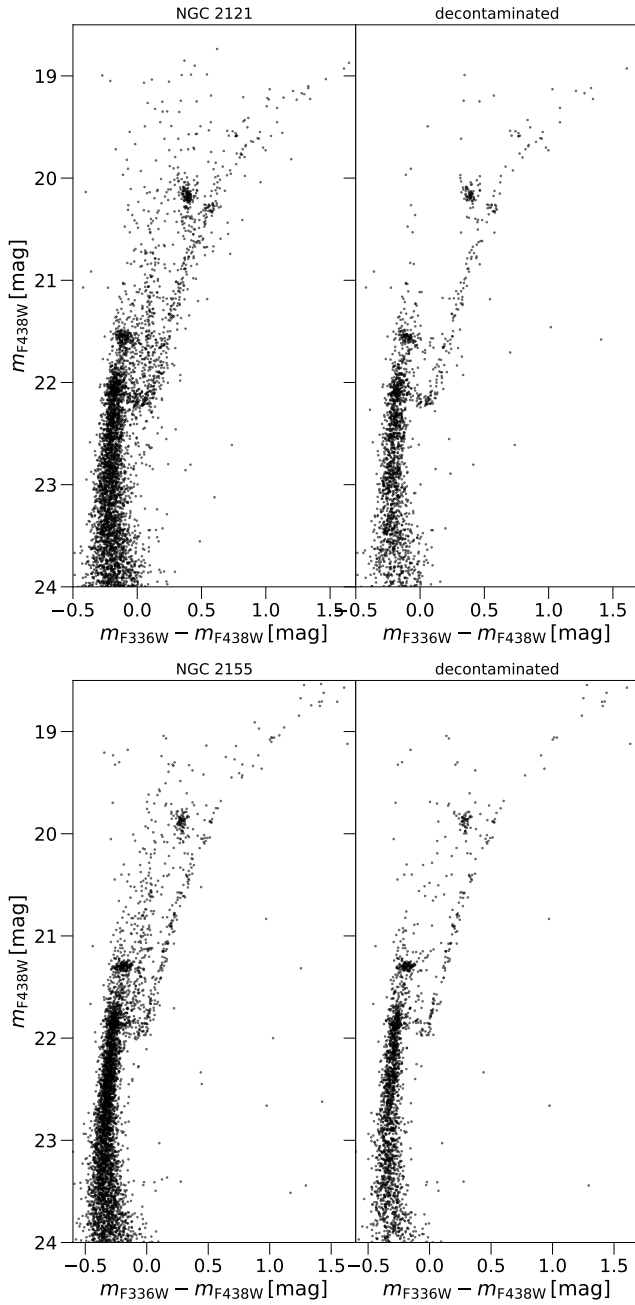


Figure 5.3:  $m_{F336W} - m_{F438W}$  vs.  $m_{F438W}$  CMDs of NGC 2121 (left panels) and NGC 2155 (right panels) before and after the field star subtraction.

to define a background region that is extended enough. Figure 5.2 shows the RA vs. Dec map for Lindsay 38 (top) and Lindsay 113 (bottom), where the FOV covered by the ACS(WFC3) camera is indicated in grey(red). A first look reveals that the  $m_{\text{F}555\text{W}} - m_{\text{F}814\text{W}}$  vs.  $m_{\text{F}555\text{W}}$  CMDs of Lindsay 38 and Lindsay 113 are rather clean from field stars contamination (see Fig. 5.4). In the current analysis, we considered all the stars in common between the ACS and WFC3 catalogue for Lindsay 38.

We note that, for NGC 2155, the WFPC2 catalogue was only used to give an estimate of the age of the cluster (see §5.1.1). The optical images (F450W and F555W/WFPC2) only have one exposure per filter (Table 2.1) and we found that the addition of these filters to the catalogue was not useful, instead it only added noise.

We also corrected our photometric catalogues for differential reddening (§2.2.3). We found that our clusters are not significantly affected by differential reddening, with a maximum  $\delta E(B - V)$  of  $\sim 0.003$  mag for Lindsay 38 and  $\sim 0.005$  mag for Lindsay 113 and NGC 2121.

As in our previous analysis (Chapters 2,3), we first selected bona-fide RGB stars in the  $m_{\text{F}555\text{W}} - m_{\text{F}814\text{W}}$  vs  $m_{\text{F}814\text{W}}$  CMD and then in the  $m_{\text{F}438\text{W}} - m_{\text{F}814\text{W}}$  vs  $m_{\text{F}814\text{W}}$  CMD, except for NGC 2155 where RGB stars were selected in the  $m_{\text{F}336\text{W}} - m_{\text{F}438\text{W}}$  vs  $m_{\text{F}438\text{W}}$  CMD. Stars were selected between the base of the lower RGB ( $\sim 0.5$  magnitude above the main sequence turnoff) and the RGB bump, to avoid contamination by SGB or AGB stars. Figure 5.4 shows the  $m_{\text{F}555\text{W}} - m_{\text{F}814\text{W}}$  vs  $m_{\text{F}814\text{W}}$  CMDs of NGC 2121, Lindsay 113 and Lindsay 38, and the  $m_{\text{F}336\text{W}} - m_{\text{F}438\text{W}}$  vs.  $m_{\text{F}438\text{W}}$  CMD for NGC 2155. Black filled circles indicate the final selected RGB stars.

We used the pseudo-colour  $C_{\text{F}336\text{W}, \text{F}438\text{W}, \text{F}343\text{N}}$  to look for a broadening in the RGB, and to make a homogeneous comparison with the other clusters in our sample. This colour is defined as  $C_{\text{F}336\text{W}, \text{F}438\text{W}, \text{F}343\text{N}} = (\text{F}336\text{W} - \text{F}438\text{W}) - (\text{F}438\text{W} - \text{F}343\text{N})$  and it has already been proven to be very effective at separating populations with different N abundances (Niederhofer et al., 2017b,a). Figure 5.5 shows the  $C_{\text{F}336\text{W}, \text{F}438\text{W}, \text{F}343\text{N}}$  vs.  $m_{\text{F}438\text{W}}$  CMDs for all the clusters analysed in this Chapter, where black filled circles represent the final selected RGB stars in each panel. At a first look, the UV CMDs

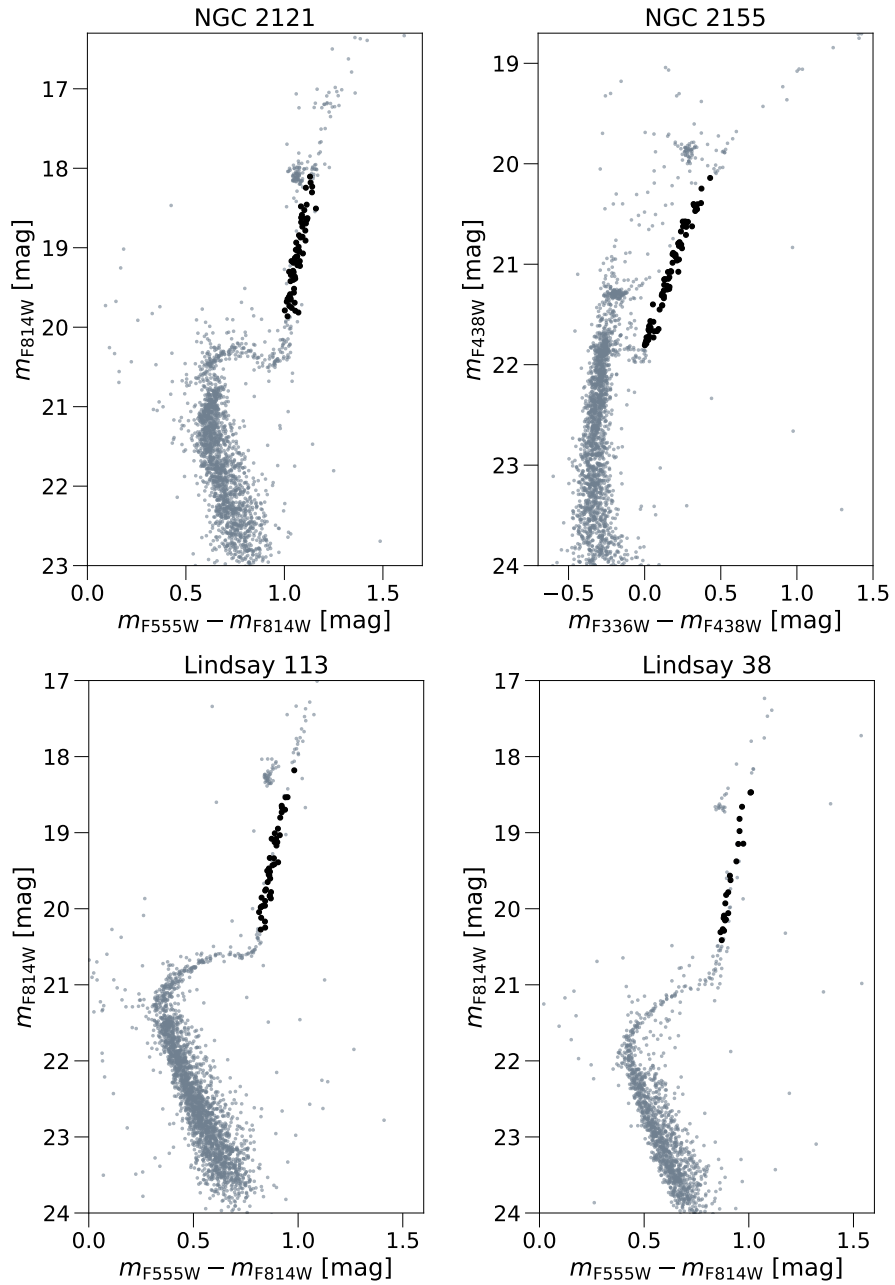


Figure 5.4:  $m_{F555W} - m_{F814W}$  vs.  $m_{F814W}$  CMDs for NGC 2121, Lindsay 113, Lindsay 38 and  $m_{F336W} - m_{F438W}$  vs.  $m_{F438W}$  CMD for NGC 2155. Black circles indicate the final selected RGB stars.

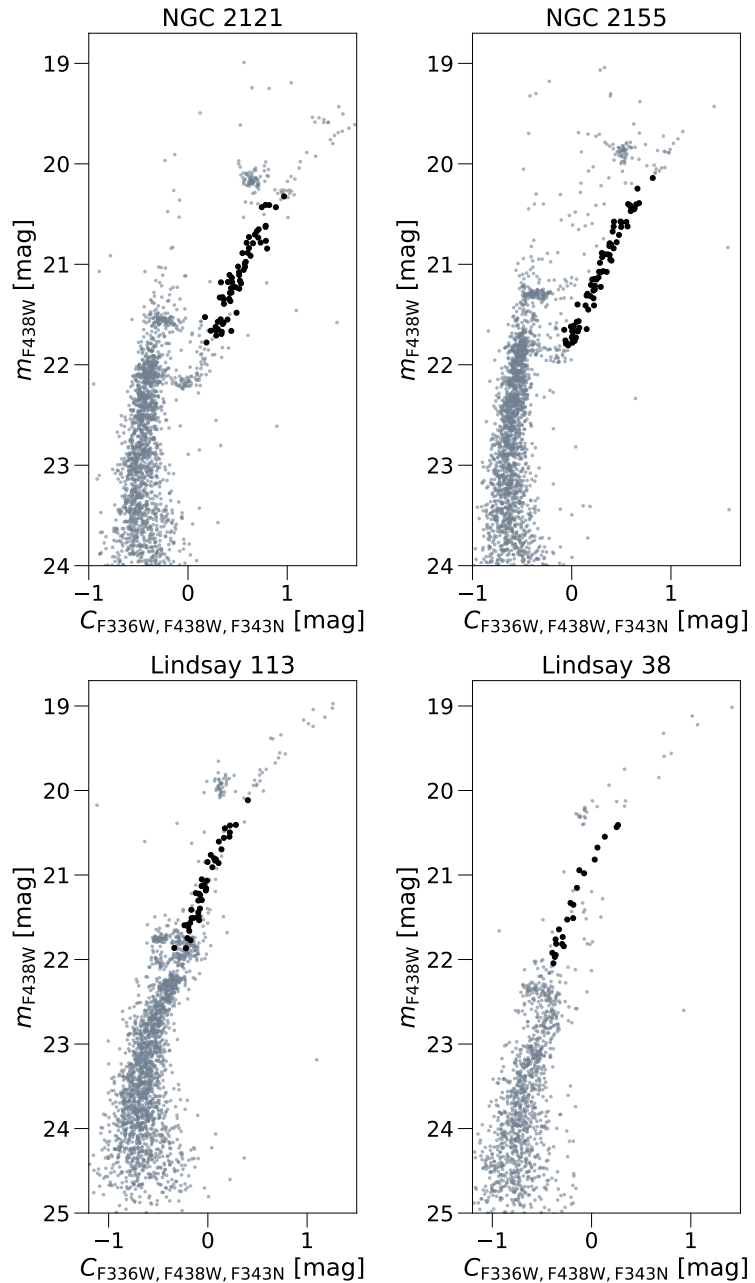


Figure 5.5:  $C_{F336W, F438W, F343N}$  vs.  $m_{F438W}$  CMDs for the clusters analysed in this Chapter. Black circles indicate the final selected RGB stars.

reveal no clear evidence for splits in the RGB and the RGB looks quite narrow in all cases, except for NGC 2121. To quantify the broadening of the RGB, we took advantage of the AS experiments (§4.1.1).

We selected RGB stars in the  $C_{F336W,F438W,F343N}$  vs.  $m_{F438W}$  CMDs of the simulated AS catalogues in the same range of magnitude and colours as for the selected observed RGB stars. We then used fiducial lines to verticalise the RGB and obtain  $\Delta(\text{colours})$  for both observed and simulated catalogues. Figure 5.6 shows the  $\Delta(C_{F336W,F438W,F343N})$  distributions for observed (black) and simulated (pink) RGB stars for the clusters analysed in this Chapter. We also calculated the standard deviations of each distribution and these are also superimposed in each panel of Fig. 5.6. Errors on standard deviations of the observed distributions were calculated with a bootstrap technique based on 5,000 realizations.

In all clusters, except for Lindsay 38, a significant broadening in the observed distributions is present when comparing them to the simulated distributions. The observed standard deviations are at least twice as large as the standard deviations of the simulated single stellar population from the AS tests (see  $\sigma$ s reported in Fig. 5.6).

The case of Lindsay 38 is dominated by poor statistics, as the RGB is composed by  $\sim 20$  stars. By looking at Fig. 5.6, there are no signs of evident broadening in the RGB of Lindsay 38. The standard deviation of the observed distribution is comparable with what we expect from the simulated AS distribution, within the errors.

Hence, the fact that the distributions of NGC 2121, NGC 2155 and Lindsay 113 are broader than what is expected from a single stellar population, suggests that N variations are present in the RGB stars of such clusters. Based on the current dataset and error estimation, no N variations are instead found in Lindsay 38. A comparison with the other clusters in our HST survey will be made in the next Section (§5.2).

We then fit the discrete  $\Delta(C_{F336W,F438W,F343N})$  data with Gaussian Mixture Models (GMM) to identify the presence of multiple Gaussian components in the colour distribution. We thus derived the probability that a bimodal distribution is rejected for each cluster. Within our observational uncertainties, we find p-values larger than 25%

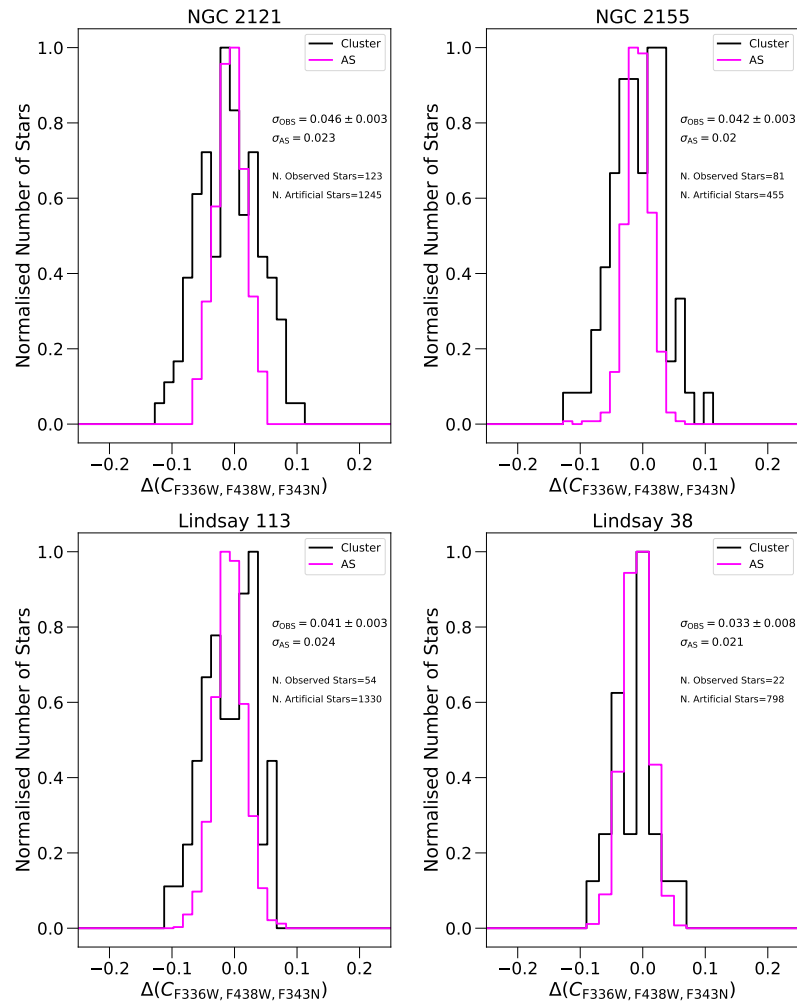


Figure 5.6: Histograms of the distributions of observed (black) and simulated (pink) RGB stars in verticalised  $C_{F336W}, F438W, F343N$  colours for the clusters analysed in this Chapter. The same bin size was used for real data and AS. Superimposed on the plots are the values of the standard deviations of the distributions. See text for more details.

for all clusters, which demonstrates that bimodality is unlikely in all cases. This was obtained with a parametric bootstrap technique by using the GMM code by [Muratov & Gnedin \(2010\)](#).

When comparing observations to AS catalogues we should note that the errors obtained from AS experiments are systematically underestimated. The main reason is that all AS experiments are simplified to some extent and they are not able to account for all the instrumental sources of noise. The main factor responsible for the error underestimation is likely that the PSF used to fit the artificial stars is also the one used to create them, at odds with what happens with the real stars. The typical difference between errors from AS and true observational uncertainties has been estimated in previous studies and is of the order of 30 – 40% (see Fig. 4 of [Dalessandro et al. 2011a](#) and related text and Fig. 21 of [Milone et al. 2012](#)). In all clusters, except for Lindsay 38, we observe that the width of the observed distributions is  $\gtrsim 50\%$  of the width of the AS distributions, thus we can safely say that a broadening (which is not due to photometric errors) is present in NGC 2121, NGC 2155 and Lindsay 113. Our results for NGC 2121 agree with the conclusions of [Li & de Grijs \(2019\)](#).

### 5.1.1 Age Determination

To estimate the age of the clusters in our sample, we superimposed BaSTI isochrones ([Pietrinferni et al. 2004](#)) on the optical CMDs of the clusters analysed in this Chapter. We decided to assume average and fixed distance moduli for the LMC and SMC to minimize the number of free parameters involved in the age determination. We assume  $(m - M)_{\text{LMC}} = 18.477$  ([Pietrzynski et al., 2019](#)) and  $(m - M)_{\text{SMC}} = 18.965$  ([Graczyk et al., 2019](#)).

Several isochrones with different metallicities have been used for the fitting of each cluster. The metallicity was chosen to best match simultaneously the RGB and MS. Figure 5.7 shows the  $m_{\text{F}555\text{W}} - m_{\text{F}814\text{W}}$  vs.  $m_{\text{F}555\text{W}}$  CMDs for NGC 2121 and Lindsay 38 and the  $m_{\text{F}450\text{W}} - m_{\text{F}555\text{W}}$  vs.  $m_{\text{F}555\text{W}}$  CMD for NGC 2155. Superimposed on the data are three isochrones at different ages, where certain values of metallicity [Fe/H]

and extinction  $E(B - V)$  were adopted. For NGC 2121, we found that the best fit parameters reproducing the shape of the CMD in all its evolutionary stages are: age  $\simeq 2.5$  Gyr, metallicity  $[Fe/H] = -0.35$  dex, and extinction value  $E(B - V) = 0.08$  mag. We find a similar best fit age for NGC 2155 ( $\sim 2.5$  Gyr) along with a metallicity of  $[Fe/H] = -0.66$  dex and  $E(B - V) = 0.03$  mag. For these clusters, we used BaSTI isochrones that account for the effects of core convective overshooting during the central H-burning stage.

For Lindsay 38, the best fit parameters we found by fitting canonical BaSTI isochrones are the following: age  $\simeq 6.5$  Gyr,  $[Fe/H] = -1.5$  dex,  $E(B - V) = 0.02$  mag.

BaSTI isochrones on Lindsay 113 could not fit well both MS, RGB and the horizontal branch (HB) at the same time, thus we also explored MIST isochrones (Dotter 2016; Choi et al. 2016). Figure 5.8 shows the  $m_{F555W} - m_{F814W}$  vs.  $m_{F555W}$  CMDs for Lindsay 113, where BaSTI (left) and MIST (right) isochrones at different ages are superimposed. By adopting the same extinction, we find that there is no considerable difference between the results we get either with BaSTI or MIST. Thus, we found that the best isochrones reproducing the CMD are the 4-4.5 Gyr MIST isochrones with  $[Fe/H] = -1.3$  dex and  $E(B - V) = 0.01$  mag (respectively blue and orange curves in Fig. 5.8). We also note that for NGC 2155 and Lindsay 38, the HB is not matched perfectly. A better fit could be reached by slightly changing the cluster distance moduli. However, we conservatively decided to keep them fixed as the required changes have only a small impact on the derived ages.

Table 6.1 provides information about the parameters adopted for the clusters analysed in this Chapter. Values of cluster masses from the literature are also reported.

The results shown here are fairly consistent with the literature. Glatt et al. (2008b) report an age of  $6.5 \pm 0.5$  Gyr and a metallicity  $[Fe/H] = -1.5$  dex for Lindsay 38 by using the Dartmouth isochrones. Also, Rich, Shara & Zurek (2001) report an age of  $3.2 \pm 0.5$  Gyr for both NGC 2121 and NGC 2155 by using the Padova isochrones, slightly older than what we found, assuming  $[Fe/H] = -0.68$  dex and using Girardi isochrones. Finally, Mighell, Sarajedini & French (1998) report an age of 4 – 5 Gyr for Lindsay 113, with

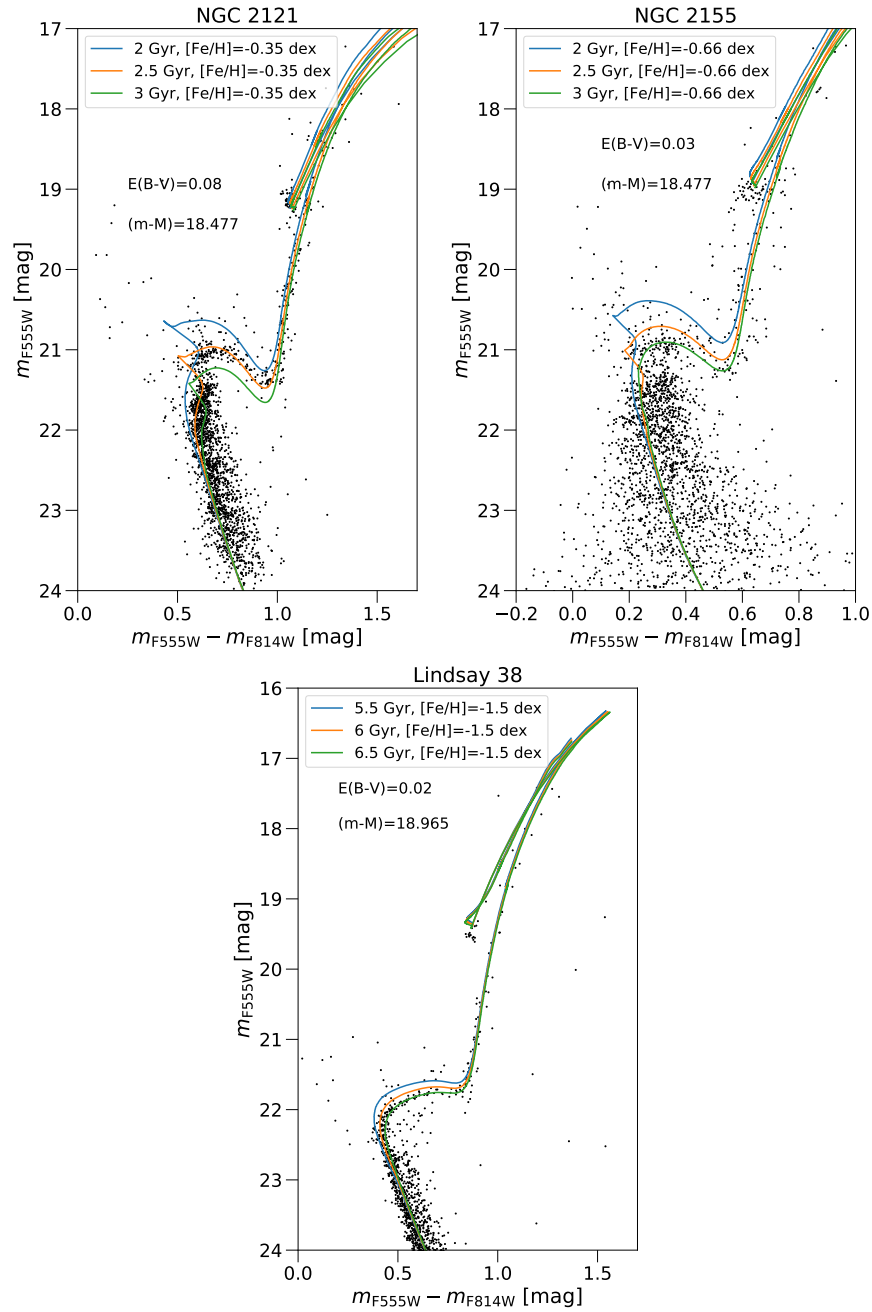


Figure 5.7:  $m_{F555W} - m_{F814W}$  vs.  $m_{F555W}$  CMDs for NGC 2121, NGC 2155 and Lindsay 38, respectively from left to right. The blue, orange and green curves represent BaSTI isochrones at different ages (see legend). The metallicity adopted for each cluster is reported in the legend. Finally, the values of the extinction  $E(B - V)$  and distance modulus  $(m - M)$  are shown in the upper left part of the plots.

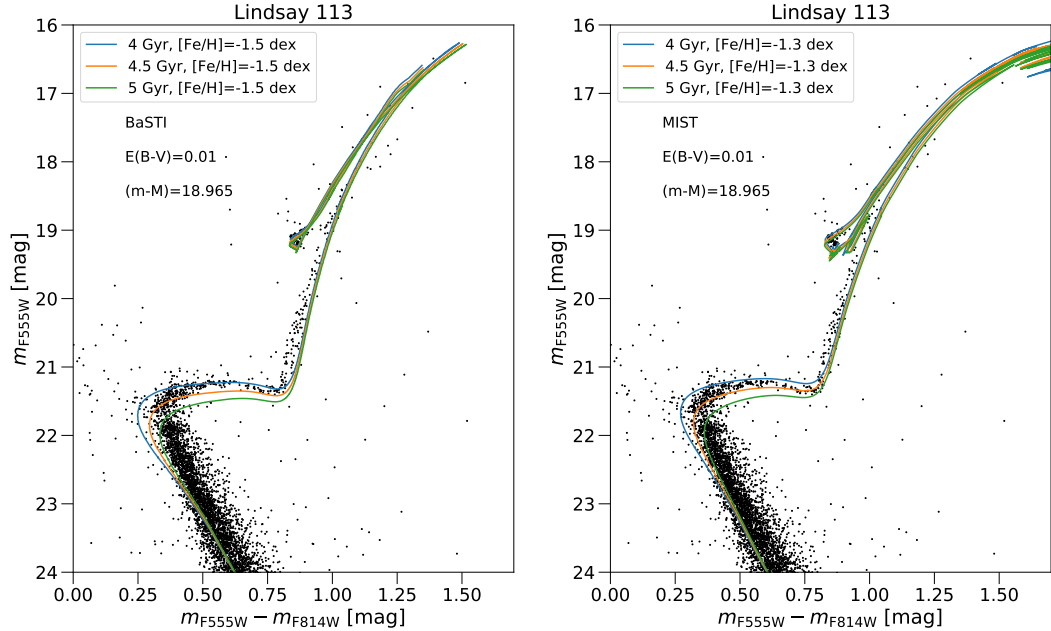


Figure 5.8:  $m_{\text{F}555\text{W}} - m_{\text{F}814\text{W}}$  vs.  $m_{\text{F}555\text{W}}$  CMDs for Lindsay 113. The blue, orange and green curves represent BaSTI (left) or MIST (right) isochrones at different ages. The adopted metallicity is reported in the legend for each panel. Finally, the values of the extinction  $E(B - V)$  and distance modulus ( $m - M$ ) are shown in the upper left part of the plots.

Table 5.1: Adopted values of age, metallicity, distance modulus and reddening for the clusters analysed in this Chapter. The reported cluster masses are taken from the literature.

Cluster Name	Age (Gyr)	[Fe/H] (dex)	$(m - M)$ (mag)	$E(B - V)$ (mag)	Mass ( $\times 10^5 \text{ M}_\odot$ )	Mass Ref.
NGC 2121	2.5	-0.35	18.477*	0.08	1	(1)
NGC 2155	2.5	-0.66	18.477*	0.03	0.36	(1)
Lindsay 113	4.5	-1.3	18.965 <sup>†</sup>	0.01	0.23	(2)
Lindsay 38	6.5	-1.5	18.965 <sup>†</sup>	0.02	0.15	(3)

(1) McLaughlin & van der Marel (2005); (2) Chantereau et al. (2019); (3) Glatt et al. (2011).

\*: fixed value from Pietrzynski et al. (2019) (LMC) <sup>†</sup>: fixed value from Graczyk et al. (2019) (SMC).

a [Fe/H]=-1.2 dex.

From spectroscopy of red giant stars, [Grocholski et al. \(2006\)](#) find a [Fe/H]=-0.5 dex for NGC 2121 and NGC 2155. We find that NGC 2121 is slightly more metal rich ([Fe/H]=-0.35 dex, see Table 6.1), although errors due to the employment of different methods and isochrones need to be taken into account. Slightly different values have been reported in the literature for Lindsay 113, from [Fe/H]=-1.2 dex ([Da Costa & Hatzidimitriou, 1998](#)) to [Fe/H]=-1.03 dex ([Parisi et al., 2015](#)), which are also fairly consistent to what we find ([Fe/H]=-1.3 dex, see Table 6.1). Finally, no spectroscopic estimates for the metallicity of Lindsay 38 is reported in the literature so far, to the best of our knowledge.

## 5.2 Results

We combined the results obtained for the clusters analysed in this Chapter (namely NGC 2121, NGC 2155, Lindsay 113 and Lindsay 38) with those from Chapters 2, 3 (i.e. NGC 419, 1783, 1806, 1846, 1978, 416, 339, 121, Lindsay 1). Finally, we added three ancient clusters ( $\gtrsim 12$  Gyr) located in the MW, namely NGC 2419, M15 and 47 Tuc.

We calculated the standard deviation of the verticalised distribution of bona-fide RGB stars selected as described in Section 5.1 in  $C_{F336W,F438W,F343N}$  colours for the entire sample. The left panel of Figure 5.9 reports the standard deviation as a function of cluster age. Circles indicate clusters with MPs, while squares represent clusters with no significant detection of MPs. Data are colour-coded by cluster mass. Errors on standard deviations were calculated with a bootstrap technique based on 5,000 realizations.

It is interesting to observe that older clusters show much wider RGBs with respect to the younger ones, representative of more extreme populations. We find that the standard deviations in  $C_{F336W,F438W,F343N}$  of the sample analysed in this Chapter (namely NGC 2121, NGC 2155, Lindsay 113 and Lindsay 38) are comparable, within the er-

rors, with the standard deviations of the clusters that are aged  $\lesssim 2$  Gyr. Note that to establish whether chemical anomalies are present in the clusters of our sample, we compare the RGB width ( $\sigma$ ) with expectations from photometric errors. However, it is also likely that clusters younger than 2 Gyr might potentially hide smaller N variations that are not detectable by current photometric studies. Future spectroscopic observations or higher precision photometry will be crucial to understand if this may be the case or not.

Furthermore, it appears that there is not a continuous trend between  $\sigma$  and cluster age, as clusters in the age range 2.5–4 Gyr have narrower widths of the RGB with respect to NGC 1978, for instance. Nonetheless, other parameters need to be taken into account.

Cluster mass (at the present day) has been already established to play a fundamental role in the chemical anomalies picture (e.g., Milone et al. 2017, §1.6), with the extension of the abundance variations becoming larger with increasing stellar mass. Masses for the MCs clusters are taken from Table 2.3, while masses for the galactic GCs are from Baumgardt & Hilker (2018). We note that the cluster mass of our sample is no longer relatively constant. The galactic GCs are 5-10 times more massive than our previous sample, while the new MCs sample reported in this Chapter is lower mass, by factors of 2-5.

Lindsay 38 is old enough ( $\sim 6.5$  Gyr) that one would expect a broader RGB, if age would be the only parameter correlated to abundance variations. However, this cluster also has a lower mass compared to NGC 339 or NGC 416, by almost one order of magnitude.

We also explored the behaviour of the RGB by using the pseudo colour  $C_{F343N,F438W,F814W} \equiv (F343N - F438W) - (F438W - F814W)$  which was used in our previous HST survey study (Chapters 2,3). The right panel of Figure 5.9 reports the standard deviation of the RGB distributions in verticalised  $C_{F343N,F438W,F814W}$  colours as a function of cluster age, colour-coded by cluster mass. However, we did not include two clusters of our sample in this plot, namely NGC 2121 and NGC 2155. For the former, we analysed the errors in the WFPC2 F555W and F814W filters and we noticed

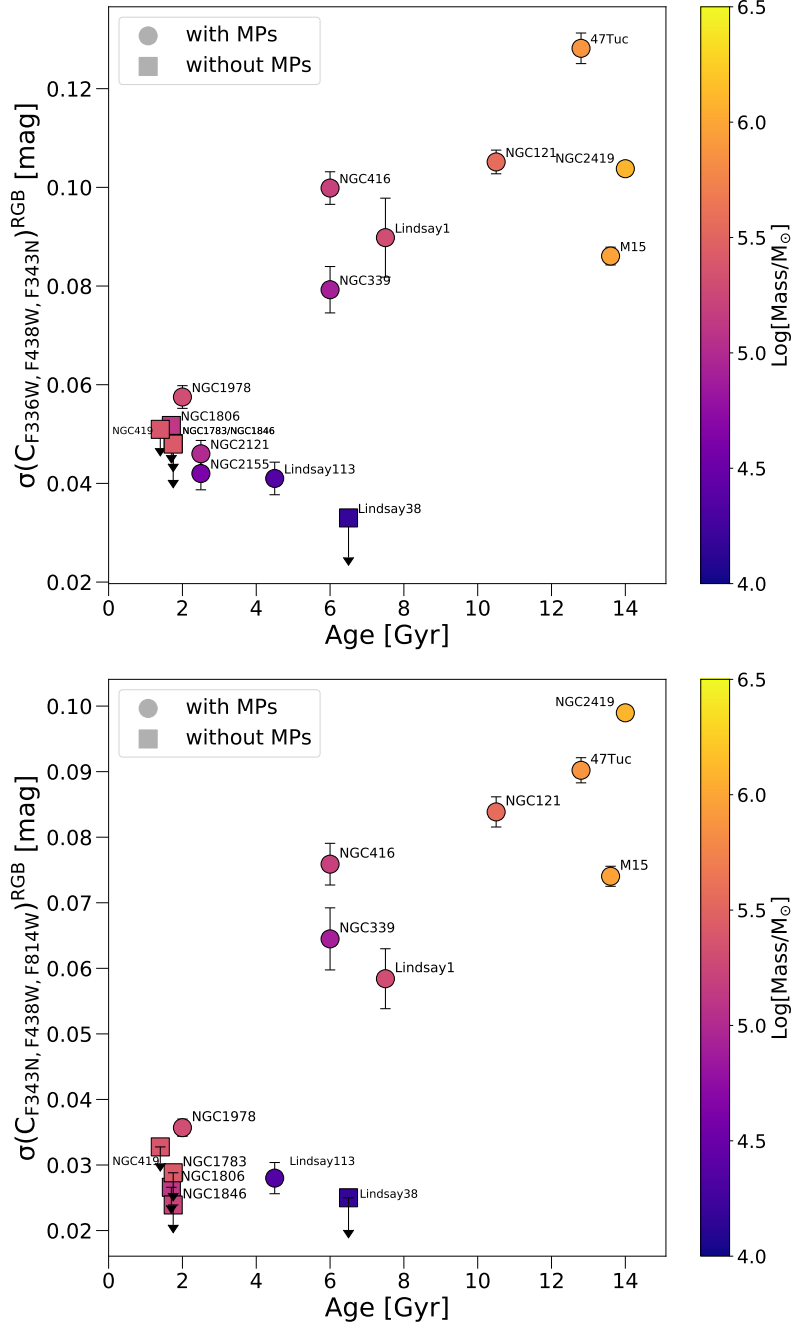


Figure 5.9: Standard deviation of the RGB observed distribution in  $C_{F336W,F438W,F343N}$  (left) and  $C_{F343N,F438W,F814W}$  (right) colours as a function of cluster age for all the clusters in our HST survey plus 47 Tuc, NGC 2419 and M15. Circles represent cluster with MPs, while squares indicate clusters with no MPs. Data are colour-coded by cluster mass.

that these are more than twice as much compared to the ACS optical filter errors for Lindsay 38 and Lindsay 113. For this reason, we decided not to show the results for NGC 2121 in the  $C_{F343N,F438W,F814W}$  plots. Regarding NGC 2155, we do not have the necessary filters, as only WFPC2 observations in F450W and F555W bands are available (see Table 2.1). New optical observations are clearly needed to fully characterise those two clusters. The  $\sigma(C_{F343N,F438W,F814W})$  vs. age plot is consistent with what we found in  $C_{F336W,F438W,F343N}$  colours. This contributes to strengthen the result that a correlation between N spread and cluster age is present.

Cabrera-Ziri et al. (in preparation) will present a detailed modelling of the effect of age (i.e., the effective temperature of the RGB) and metallicity on the measured widths of  $C_{F336W,F438W,F343N}$  and  $C_{F343N,F438W,F814W}$ . However, for the purposes of this work, the models confirm that  $C_{F343N,F438W,F814W}$  is essentially independent of age and also of [Fe/H] down to the regime of metal-poor Galactic GCs. Any observed variation/relationship between  $C_{F343N,F438W,F814W}$  and cluster age can then be attributed to a signature of N enrichment. There is a small effect of [Fe/H] on  $C_{F336W,F438W,F343N}$ , in the sense that lower [Fe/H] values result in smaller  $\Delta(C_{F336W,F438W,F343N})$  values, but as the two Galactic GCs M15 and NGC 2419 have much lower [Fe/H] but larger  $\sigma(C_{F336W,F438W,F343N})$  values, it is clear that N variations are the driver with age in that diagram as well.

## 5.3 Discussion

The origin of the unusual chemical patterns typically found in GC stars has remained an unsolved puzzle so far. Although much effort has been put into developing new scenarios (e.g. [Gieles et al. 2018](#); [Breen 2018](#); [Howard et al. 2018](#)), no consensus has been reached and many observational results remain unexplained (see [Bastian & Lardo 2018](#)). The exploration of whether a star cluster hosts MPs based on certain cluster properties has been an important avenue of investigation. It is now established that (present day) cluster mass is a fundamental property controlling the extent of which MPs are present, with the star-to-star abundance variations becoming more

severe with increasing cluster mass (e.g., Bragaglia et al. 2012; Schiavon et al. 2013; Milone et al. 2017). On the other hand, we also know that mass cannot be the only parameter which comes into play, as many massive star clusters, although much younger than ancient GCs, do not show evidence for the chemical anomalies (Mucciarelli et al., 2008; Cabrera-Ziri et al., 2016b; Lardo et al., 2017; Martocchia et al., 2017, 2018a).

To shed light onto this, we planned a photometric survey to target star clusters that are as massive as old GCs, but significantly younger. In this Chapter, we reported on the photometric analysis of new HST UV images for four clusters in the MCs, namely NGC 2121, NGC 2155, Lindsay 113 and Lindsay 38. These clusters have a mass a few times  $10^4 M_\odot$  except for NGC 2121 which is  $\sim 10^5 M_\odot$  (see Table 6.1) and they are aged between  $\sim 2.5$  and  $\sim 6$  Gyr.

The UV CMDs of each cluster (see Fig. 5.5 for the  $C_{F336W,F438W,F343N}$  vs.  $m_{F438W}$  CMDs) reveal no presence of splits in the RGBs. We quantified the broadening of the RGB by comparing the observed verticalised distributions of RGB stars with artificial RGB stars (§5.1). Three out of four clusters in the sample show a significant broadening with respect to photometric errors in  $C_{F336W,F438W,F343N}$  colours, i.e. colours that are sensitive to N variations; Lindsay 38 is the only cluster of the sample whose RGB width is compatible with the errors. Thus, we add three intermediate-age clusters to our HST survey that show MPs in the form of N spread, namely Lindsay 113, NGC 2121 and NGC 2155.

In Chapter 3, we reported a correlation between cluster age and N enhancement as inferred from photometry, for 9 clusters in the sample. Here we expand our sample to 16 clusters by adding also three GCs (age  $\gtrsim 12$  Gyr) from the MW, namely NGC 2419, M15 and 47 Tuc. We calculate the standard deviation of the verticalised RGB distribution in  $C_{F336W,F438W,F343N}$  and  $C_{F343N,F438W,F814W}$  colours and we plot this quantity as a function of cluster age. Our results are shown in Fig. 5.9. We find that older clusters show larger widths of the RGB, thus larger N enhancement. The addition of 7 clusters to the previous sample strengthens the idea that cluster age plays a role in shaping the properties of MPs in GCs.

However, the exact role of age is currently unknown. It could be suggested that the onset of MPs is due to an evolutionary effect. In our sample we are comparing stars of different masses along the RGB. Some unidentified process operating only in stars less massive than  $1.5 M_{\odot}$  (the mass of a RGB star at  $\sim 2$  Gyr) may be responsible for the formation of the chemical anomalies. Accordingly, we tentatively argue that chemical anomalies could be expected to be found in stars with masses below  $1.5 M_{\odot}$  on the main sequence of young clusters ( $< 2$  Gyr, c.f. §5 point iv, [Cabrera-Ziri et al. 2016b](#)).

We note however that our observations are effectively probing N variations among RGB stars within our sample of clusters. An alternative explanation might therefore be linked to stellar evolutionary processes where the observed surface abundance of N in RGB stars may be affected. If this is the case, we may expect to find N-spreads on the main sequence of clusters that do not correspond to the spreads observed along the RGB. This can also be tested by looking at elements less likely to be affected by stellar evolution, e.g., Na or Al.

It is interesting to note that cluster age and cluster mass seem to work simultaneously. We find that a difference in cluster mass also has an impact at younger ages. As already argued in §5.2, we observe that Lindsay 38 has a similar age to NGC 339 and NGC 416 but its RGB is less than half as wide. The mass of Lindsay 38 is estimated to be  $\sim 10^4 M_{\odot}$  ([Glatt et al., 2011](#)), an order of magnitude smaller than those of NGC 339 and NGC 416.

However, since all of the clusters in our sample belong to the MCs, it is also possible that the appearance of MPs at 2 Gyr could be due to an unknown environmental effect. It would be extremely interesting to test the presence of MPs in clusters beyond the MW and its satellites, but this remains difficult, and new techniques based on integrated light will likely be necessary.

# Chapter 6

## Is Fornax 4 the nuclear star cluster of the Fornax dwarf spheroidal galaxy?

Fornax 4 is the most distinctive globular cluster in the Fornax dwarf spheroidal. Located close to the centre of the galaxy, more metal-rich and potentially younger than its four companions (namely, Fornax clusters number 1, 2, 3 and 5), it has been suggested to have experienced a different formation than the other clusters in the galaxy.

In this Chapter we use HST/WFC3 photometry to characterize the stellar population content of this system and shed new light on its nature. By means of a detailed comparison of synthetic HB and RGB with the observed colour-magnitude diagrams, we find that this system likely hosts stellar sub-populations characterized by significant iron spread up to  $\Delta[\text{Fe}/\text{H}] \sim 0.4$  dex and possibly by also some degree of He abundance variations  $\Delta Y \sim 0.03$ . We argue that this purely observational evidence, combined with the other peculiarities characterizing this system, supports the possibility that Fornax 4 is the nuclear star cluster of the Fornax dwarf spheroidal galaxy. A spectroscopic follow-up for a large number of resolved member stars is needed to confirm this interesting result and to study in detail the formation and early evolution of this system and more in general the process of galaxy nucleation. This Chapter is based on the work by [Martocchia et al. \(2020\)](#).

## 6.1 Introduction

Fornax and Sagittarius are the only known dwarf spheroidals (dSphs) in the Local Group that host a GC system. Interestingly, despite having a relatively small stellar mass of a few times  $10^7 M_\odot$  ([McConnachie, 2012](#)), the Fornax dSph hosts at least five GCs, with the existence of a sixth one announced recently ([Wang et al., 2019](#)).

The Fornax GC system is interesting in many aspects: its GC specific frequency, i.e. the number of clusters normalised to the total visual magnitude of the galaxy, is among the largest observed ([Georgiev et al., 2010](#)), and even more intriguing is the observed difference in the peak metallicity of its GCs compared to the underlying stellar metallicity ([Larsen, Strader & Brodie, 2012b](#)). These properties of the Fornax GC system provide important constraints for GC formation efficiency as well as mass-loss and self-enrichment ([Larsen, Strader & Brodie, 2012b](#); [Lamers et al., 2017](#)).

Similarly to what is observed in ancient GCs in the MW, the Fornax clusters show light-element chemical abundance variations among their stars (multiple populations, MPs, Chapter 1, §1.3). To constrain the presence of MPs in Fornax clusters, [Larsen et al. \(2014a\)](#) analysed the width of the RGB of Fornax 1, 2, 3 and 5 by using HST filters sensitive to N variations finding that all four clusters host MPs in the form of N spreads. Additionally, [D'Antona et al. \(2013\)](#) examined the morphology of the HB of the same GCs concluding that such systems must host a large fraction of He-rich stars.

To date, no investigation of MPs in the cluster Fornax 4 has been performed. This cluster was likely excluded from previous studies due to the high contamination from field stars as this system is located very close to the galaxy center. The first and only hint that Fornax 4 might host chemical variations was given by [Larsen, Strader & Brodie \(2012a\)](#). They calculated the [Mg/Fe] from the integrated light spectra of Fornax 3, 4 and 5, finding it to be significantly lower than the [Ca/Fe] and [Ti/Fe] ratios, contrary to what is generally observed in field stars in the Galaxy and in dSphs. They interpreted this as a potential signature of MPs.

By using optical HST photometry, [Buonanno et al. \(1999\)](#) found that Fornax 4 has a

much redder HB and brighter SGB than the other GCs in Fornax. They concluded that Fornax 4 is  $\sim 3$  Gyr younger than the other clusters, which are on average  $\sim 12$  Gyr old. They derived a metallicity of  $[\text{Fe}/\text{H}] < -2$  dex for Fornax 4, which is significantly lower than what obtained by [Strader et al. \(2003\)](#) based on integrated spectroscopy ( $[\text{Fe}/\text{H}] = -1.5$  dex) and by [Larsen, Strader & Brodie \(2012a\)](#) ( $[\text{Fe}/\text{H}] = -1.4$  dex). The other GCs in the Fornax dSph are more metal-poor, with metallicities ranging from  $[\text{Fe}/\text{H}] = -1.8$  dex to  $[\text{Fe}/\text{H}] = -2.3$  dex ([Larsen, Strader & Brodie, 2012a](#)). These results have been recently confirmed by [de Boer & Fraser \(2016\)](#) who studied the star formation history of Fornax 4 and found that it is indeed younger and more metal-rich compared to the other clusters in the galaxy.

The position, higher metallicity and younger age of Fornax 4 led many authors (e.g. [Hardy 2002](#); [Strader et al. 2003](#)) to consider it as the nuclear star cluster (NSC) of the Fornax dSph. A NSC is a very dense and massive star cluster which resides in the innermost region of a given galaxy ([Böker et al., 2002](#); [Neumayer et al., 2011](#)). If this is the case for Fornax 4, it should be expected to show a significant iron spread, as is typically observed in such systems (e.g. [Walcher et al. 2006](#); [Lyubenova et al. 2013](#); [Kacharov et al. 2018](#)). However, at the moment there is no consensus about the real nature of Fornax 4 and whether or not it is a genuine GC or a NSC is still an open question (see the discussion in [Hendricks et al. 2016](#) for more details).

By using HST/WFC3 archival observations, we study in detail the stellar population properties of Fornax 4 with the aim of providing new clues on its nature and formation. This Chapter is structured as follows: in Section §6.2 we report on the photometric reduction procedures, while we outline the calculation of the structural parameters in Section §6.3. We estimate the age of Fornax 4 in Section §6.4. In Section §6.5 we characterize the stellar population properties in the system. Finally, we discuss and conclude in §6.6.

## 6.2 Observations and data reduction

We used HST/WFC3 images obtained through filters F438W and F814W (GO-13435, P.I. M. Monelli). The dataset consists of: i) 12 exposures of 200s each for the F438W, ii) 6 exposures of 150s each for the F814W.

The same photometric method reported in Chapter 2 has been applied to the Fornax 4 data.

### 6.2.1 Artificial Stars Test

We performed AS experiments following the method described in [Dalessandro et al. \(2011a\)](#), see also [Bellazzini et al. 2002; Dalessandro et al. 2015, 2016](#)) to derive a reliable estimate of the photometric errors. Briefly, we generated a catalog of simulated stars with a F814W-band input magnitude ( $F814W_{in}$ ) extracted from a luminosity function (LF) modeled to reproduce the observed LF in that band and extrapolated beyond the observed limiting magnitude. We then assigned a  $F438W_{in}$  magnitude to each star extracted from the luminosity function, by means of an interpolation along the mean ridge line obtained from the observed  $m_{F438W} - m_{F814W}$  vs  $m_{F814W}$  CMD. Artificial stars were added to real images by using the software DAOPHOTIV/ADDSTAR. We minimized “artificial crowding”, placing stars into the images following a regular grid composed by  $15 \times 15$  pixel cells (roughly corresponding to 10 FWHM) in which only one artificial star for each run was allowed to lie. More than 100,000 stars have been simulated in each WFC3 chip. AS experiments have adopted the same reduction strategy and models for PSF that are used for real images on both real and simulated stars. In such a way, the effect of radial variation of crowding on both completeness and photometric errors is accounted for. The AS catalog was then used to derive photometric errors for HB and RGB stars, which will be used in the following analysis (see §6.5). The analysis of the AS stars was carried out applying the same cuts in photometric quality indicators (sharpness – *sharp*) that have been applied in the data (see Section 6.3). The method reported here is very similar to the one performed in Chapter

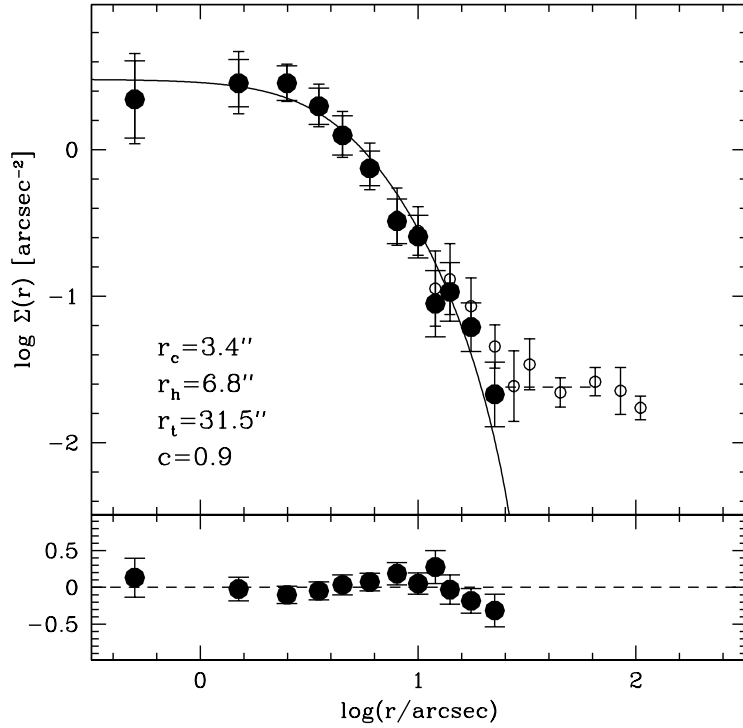


Figure 6.1: **Top panel:** Stellar density of Fornax 4 as a function of radius. The open circles indicate the observed density profile while the black filled circles represent the background subtracted stellar density profile. The black solid line represents the best fit of the King profile. The dashed line indicates the estimation of the background. **Bottom panel:** the residuals of the fit are shown. See the text for more details.

4, §4.1.1.

## 6.3 Structural Parameters

To derive the structural parameters of Fornax 4, we built the cluster number density profile by using stars with sharpness  $|sharp| < 0.1$ . As a first step we derived the centre of gravity of the cluster by using the same approach described in [Dalessandro et al. \(2013a\)](#). A first estimate of the cluster center was performed by eye, then the center was measured through an iterative procedure that averages the absolute positions of the stars lying within four different concentric radial regions ranging from  $10''$  to  $25''$  with a step of  $5''$ . Only stars with  $m_{F438W} < 25$  were selected. The adopted cluster center is the mean of the different derived values,  $C_{grav} = (02:40:07.737, -34:32:10.96)$ ,

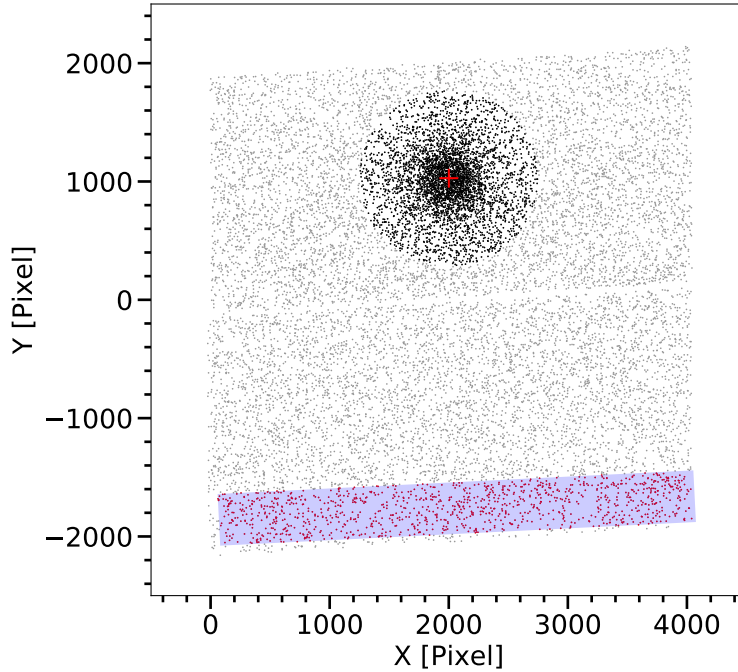


Figure 6.2: Distortion-corrected X vs Y map for the WFC3 field. The red cross indicates the centre of the cluster while black circles represent stars that are within a radius of 30 arcsec from the centre of the cluster. The purple region represents the area defined for the background, where stars used for the decontamination are indicated as red circles.

with uncertainties  $\sigma_{R.A.} = 0.4''$  and  $\sigma_{Dec} = 0.3''$ . The density profile analysis was performed following the procedure fully described in [Miocchi et al. \(2013\)](#).

We used the AS catalogue to calculate the photometric completeness as a function of the distance from the cluster centre and magnitude. We assigned a completeness value  $C$  to every star in the real catalogue. We split the WFC3 FoV in 19 concentric annuli centered on  $C_{grav}$ , each one divided into two, three, or four sub-sectors. In each sub-sector, we estimated the total number of stars with  $m_{F438W} < 24$  normalized to their completeness, i.e.  $\Sigma(1/C)$ . The projected stellar density in each annulus is then the mean of the values measured in each sub-sector and the uncertainty has been estimated from the variance among the sub-sectors. The derived density profile is shown in Figure 6.1 as open circles. The dashed line indicates the background, which was determined from stars at  $\text{Log}(r/\text{arcsec}) > 1.4$ . The black filled circles represent the background subtracted stellar density profile. We then derived the cluster structural parameters by fitting the observed density profile with a spherical, isotropic,

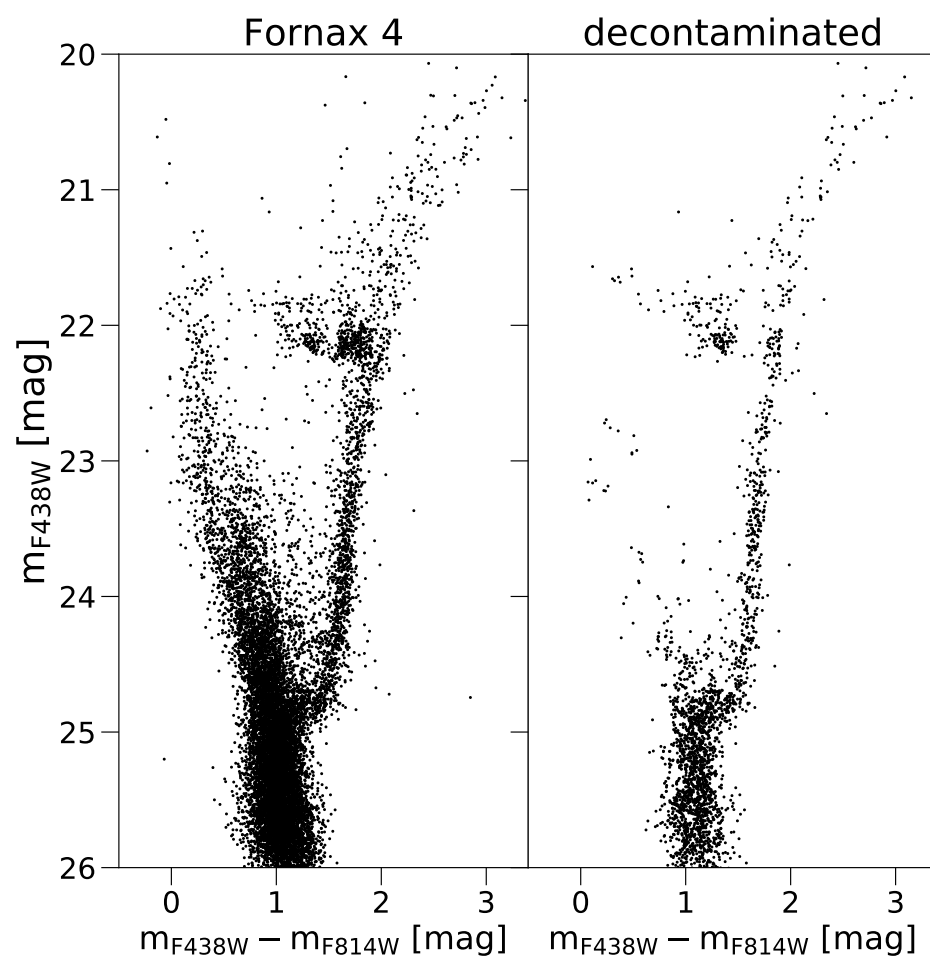


Figure 6.3:  $m_{\text{F}438\text{W}} - m_{\text{F}814\text{W}}$  vs.  $m_{\text{F}438\text{W}}$  CMD of Fornax 4 before (left panel) and after (right panel) the field star subtraction.

single-mass [King \(1966\)](#) model. The best-fit model results in a cluster with a King dimensionless potential  $W_0 = 5.0$ , corresponding to a concentration parameter of  $c = 0.9$ , a core radius of  $r_c = (3.4 \pm 0.7)''$  and a tidal radius  $r_t = (31.5 \pm 4.8)''$ .

The structural parameters of the Fornax clusters were previously studied by [Webbink \(1985\)](#) and more recently by [Mackey & Gilmore \(2003\)](#). The latter determined the surface brightness profile of Fornax 4 by using WFPC2 observations in F555W and F814W bands. They find a core radius of  $(2.64 \pm 0.27)''$  which is compatible within the errors with the value obtained in this work, although slightly lower.

Based on the obtained structural parameters, we then selected stars within a radius of  $30''$  from the centre of Fornax 4, as “cluster region”. Figure 6.2 shows the instrumental coordinates (X,Y) map for Fornax 4 in the WFC3 field. Black points represent the selected stars in the cluster region while the red cross indicates  $C_{grav}$ . We performed a statistical decontamination analysis to get a clean CMD, following the method by [Niederhofer et al. \(2017a\)](#). We defined a background reference region with the same area as the cluster region in order to statistically subtract field stars from the cluster CMD in the  $m_{F438W} - m_{F814W}$  vs.  $m_{F438W}$  space. For every star in the background region, the closest star in colour-magnitude space in the cluster region is removed. Since the contamination in the field of Fornax 4 is large, we performed the field stars subtraction by using 3 different areas for the background region: one at the bottom of chip 2 (see Fig. 6.2, the purple area), one at the centre of chip 2 and a final one on the top. No significant differences were detected between the cleaned CMDs in the three cases. Hence, for the following analysis we decided to use the catalogue where the cluster and background regions are defined as in Fig. 6.2. Fig. 6.3 shows the  $m_{F438W} - m_{F814W}$  vs.  $m_{F438W}$  CMD of Fornax 4, before (left panel) and after (right panel) the field star subtraction. While statistical decontamination may be prone to non-negligible uncertainties (e.g. [Dalessandro et al. 2019](#)), it is possible to note how both the main sequence and red clump ( $m_{F438W} - m_{F814W} \sim 1.5$  mag and  $m_{F438W} \sim 22$  mag) of the young population of stars in the Fornax dSph disappear after the correction.

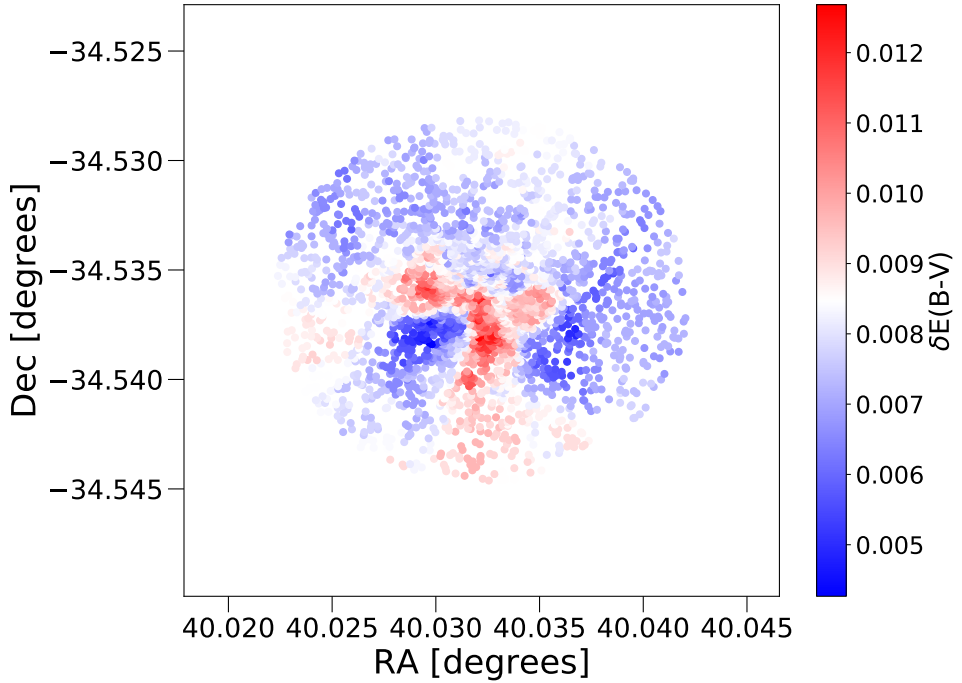


Figure 6.4: Differential reddening map for Fornax 4 in the cluster region. See text for more details.

### 6.3.1 Differential extinction

We corrected our photometric catalogue for differential reddening (DR) by using the same method reported in [Dalessandro et al. \(2018\)](#) and [Saracino et al. \(2018\)](#). We used our field stars subtracted catalogue for the estimation of the DR (see §6.3). We selected RGB stars in the magnitude range  $22.5 \lesssim m_{F438W} \lesssim 24.5$  and we defined a fiducial line in the  $m_{F438W} - m_{F814W}$  vs.  $m_{F438W}$  CMD for these stars. We then calculated the geometric distance ( $\Delta D$ ) from stars in this magnitude range that are  $2\sigma$  away from the line, where  $\sigma$  represents the difference in colour between the stars and the fiducial line. For each star in the catalogue, the DR correction is then estimated by computing the mean of the  $\Delta D$  values of the 20 nearest (in space) selected stars. By changing the number of neighbour stars (from 10 to 30), we obtain very similar results. The  $\delta E(B - V)$  is obtained through the following equation:

$$\delta E(B - V) = \frac{\Delta D}{\sqrt{2R_{F438W}^2 + R_{F814W}^2 - 2R_{F438W}R_{F814W}}}, \quad (6.1)$$

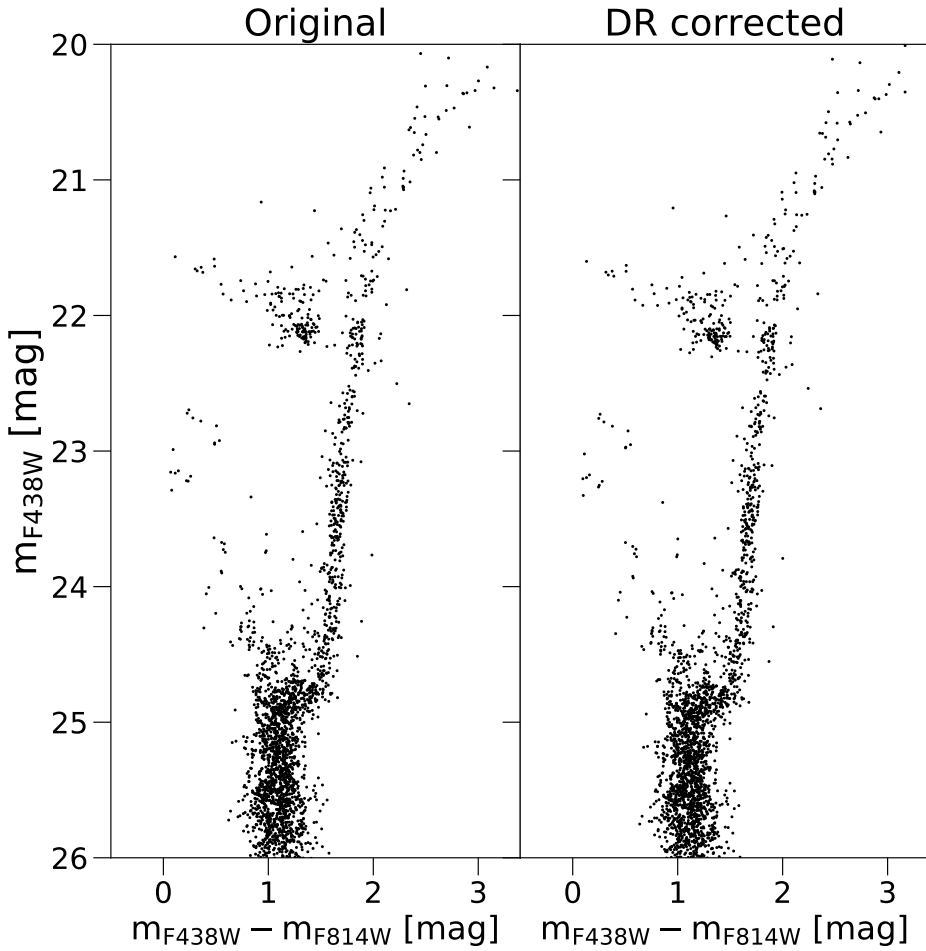


Figure 6.5: Field stars subtracted  $m_{F438W} - m_{F814W}$  vs.  $m_{F438W}$  CMDs of Fornax 4 before (left panel) and after (right panel) the differential reddening correction.

where  $R_{F438W} = 4.18$  and  $R_{F814W} = 1.86$  are the adopted extinction coefficients. Fig. 6.4 shows the DR map for Fornax 4 in the cluster region (see §6.3), while Fig. 6.5 shows the  $m_{F438W} - m_{F814W}$  vs.  $m_{F438W}$  CMDs of Fornax 4 before (left panel) and after (right panel) the DR correction. We find a maximum  $\delta E(B - V)$  of  $\sim 0.013$  mag, thus our catalogue is not significantly affected by differential extinction. Hereafter, we will use the DR corrected photometric catalogue.

## 6.4 Age and metallicity of Fornax 4

We used BaSTI isochrones (“A Bag of Stellar Tracks and Isochrones”, [Pietrinferni et al. 2004](#)) in the  $m_{F438W} - m_{F814W}$  vs.  $m_{F438W}$  CMD to obtain estimates of the [Fe/H]

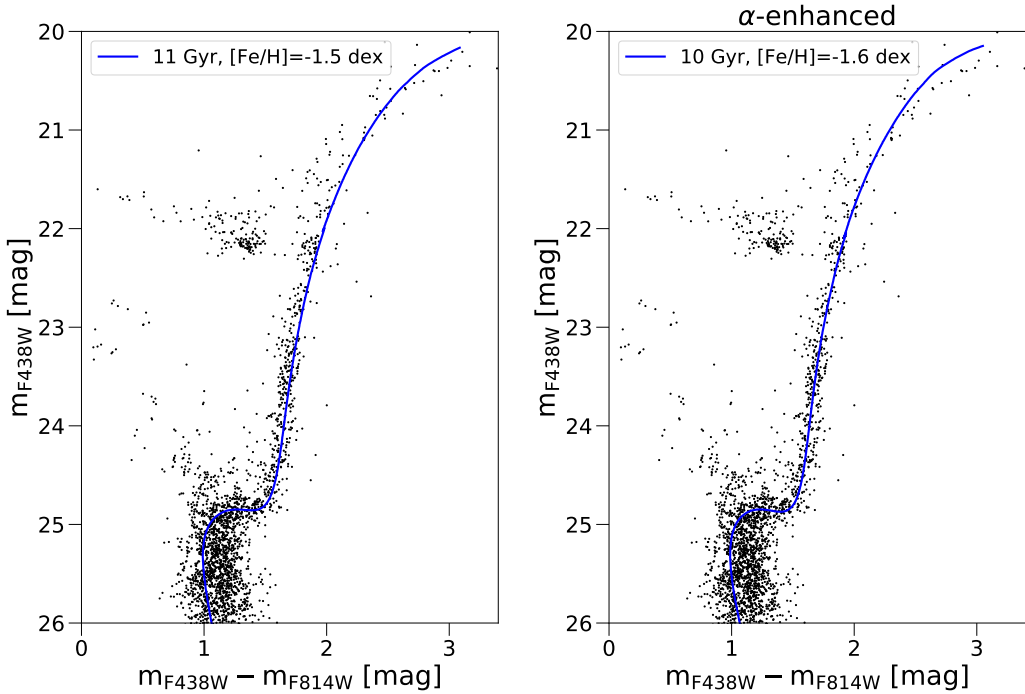


Figure 6.6:  $m_{\text{F}438\text{W}} - m_{\text{F}814\text{W}}$  vs.  $m_{\text{F}438\text{W}}$  CMDs for Fornax 4. The blue curve represents best fit solar (left panel) and  $\alpha$ -enhanced (right panel) BaSTI isochrone with the ages and metallicities shown in each panel. These are displayed with values of the extinction  $E(B - V) = 0.04$  mag and distance modulus  $(m - M)_0 = 20.94$  mag.

and age of the cluster. For the absolute distance modulus we adopt the value  $(m - M)_0 = 20.94$  mag obtained from the HB modelling (see discussion in §6.5.2), while for the extinction we used  $E(B - V) = 0.04$ , which is in the range between 0.02 and 0.08 mag found in the literature (see §6.1). The extinction ratios employed to determine the extinction in the WFC3 filters have been calculated as described in Girardi et al. (2008), using the spectral energy distributions employed in BaSTI (Pietrinferni et al., 2004).

The best matching solar-scaled isochrone has  $[\text{Fe}/\text{H}] = -1.5$  dex, and an age  $t = 11$  Gyr, whilst with  $\alpha$ -enhanced ( $[\alpha/\text{Fe}] = +0.4$  dex, the only  $\alpha$  enhancement available) isochrones we get  $[\text{Fe}/\text{H}] = -1.6$  dex and  $t = 10$  Gyr (Fig. 6.6). We are assuming that there is no chemical variation (in He and/or Fe) when estimating the age of the cluster. In §6.5.2 we will discuss the presence of an initial He abundance and/or  $[\text{Fe}/\text{H}]$  spreads, using synthetic HB modelling and colour spread of the RGB. The derived distance modulus can change by a few 0.01 mag compared to  $(m - M)_0 = 20.94$ , when these

Table 6.1: Properties of Fornax 4 derived in this work.

Cluster	Fornax 4
Age	10–11 Gyr
[Fe/H]	-1.5 – -1.6 dex
$(m - M)_0$	20.94 mag
$E(B - V)$	0.04 mag
$r_c$	3.4 arcsec
$r_t$	31.5 arcsec

abundance spreads are included, but this does not affect substantially (less than 1 Gyr) the age estimates.

The [Fe/H] values determined from Fig. 6.6 are in disagreement with [Buonanno et al. \(1999\)](#), who find  $[\text{Fe}/\text{H}] < -2$ . However, our results agree well with the integrated light spectroscopy analyses by [Strader et al. \(2003\)](#) and [Larsen, Strader & Brodie \(2012a\)](#). Also, our solar-scaled age and metallicity are consistent with the work of [Hendricks et al. \(2016\)](#). They used WFPC2 optical photometry and Dartmouth isochrones, finding a best fit of  $t = 10$  Gyr and  $[\text{Fe}/\text{H}] = -1.5$  dex, assuming no  $\alpha$ -enhancement.

Regarding the  $\alpha$  elements, [Larsen, Strader & Brodie \(2012a\)](#) report a small alpha-enhancement ( $[\alpha/\text{Fe}] \sim +0.13$  dex) using integrated light spectroscopy, while [Hendricks et al. \(2016\)](#) report  $[\alpha/\text{Fe}] = -0.19$  dex, although this result is based on a single member star, the only resolved star that has been studied so far in Fornax 4 spectroscopically. Given the current lack of consensus regarding the level of  $\alpha$ -enhancement present in Fornax 4 stars, we consider both isochrones in Figure 6.6 as best fits.

Table 6.1 displays the information on Fornax 4 derived in this study.

## 6.5 Stellar population characterization

In this Section we perform a detailed analysis of the RGB and HB population width and morphology to constrain the possible presence of sub-populations with different metallicity and/or He abundance.

### 6.5.1 The RGB width analysis

We focused our analysis on observed RGB stars in the  $m_{\text{F438W}} - m_{\text{F814W}}$  vs.  $m_{\text{F438W}}$  CMD, in the magnitude range  $22.6 < m_{\text{F438W}} < 24.3$ , i.e. the lower RGB, which is the more populated. We estimated an average error in this magnitude range from our AS tests (see §6.2.1) and we obtained  $\text{e}(m_{\text{F438W}}) \simeq 0.018$  mag and  $\text{e}(1) \simeq 0.012$  mag<sup>1</sup>. We find that observed RGB width in the selected magnitude range is  $\sim 0.042$  mag, hence it is significantly larger than what expected from photometric errors.

Since both He and Fe abundance variations affect stellar temperatures during the RGB phase, they are both expected to produce a broadening of the RGB.

First, we quantitatively estimated the value of  $\Delta[\text{Fe}/\text{H}]$  needed to reproduce the width of the cluster RGB. We generated 500 isochrones with a uniform distribution in metallicity, by interpolating between the  $\alpha$ -enhanced BaSTI isochrone from  $[\text{Fe}/\text{H}] = -1.6$  dex up to  $[\text{Fe}/\text{H}] = -1.0$  dex (see Fig. 6.6 and Table 6.1). We kept  $\Delta Y = 0$ . We populated each isochrone of the distribution in such a way that the LF in F438W magnitudes of the observed RGB is reproduced. We then added Gaussian noise to each isochrone according to the photometric uncertainties listed above, in order to simulate the RGB with a range of metallicities. We let the spread  $\Delta[\text{Fe}/\text{H}]$  vary. We compared the observed versus the simulated width of the RGB for spreads  $\Delta[\text{Fe}/\text{H}] = +0.2$ ,  $+0.3$ ,  $+0.4$  and  $+0.5$  dex. We verticalised the observed and simulated RGBs by defining two different fiducial lines in the  $m_{\text{F438W}} - m_{\text{F814W}}$  vs.  $m_{\text{F438W}}$  space. This is done to account for the different slope of the RGB between the observations and the theoretical isochrones. We then calculated the distance in  $m_{\text{F438W}} - m_{\text{F814W}}$  colours of each star from the respective fiducial line,  $\Delta(m_{\text{F438W}} - m_{\text{F814W}})$ .

The results are shown in the top panels of Fig. 6.7, where we plot the histogram of the distribution of the verticalised  $m_{\text{F438W}} - m_{\text{F814W}}$  colours vs.  $m_{\text{F438W}}$  magnitudes for

---

<sup>1</sup>Errors were derived computing the r.m.s. of the distributions of simulated stars in the  $(\text{mag}_{in}, \text{mag}_{in} - \text{mag}_{out})$  diagrams for the available bands in different magnitude bins (the RGB in this case) and after applying the same selections that were originally applied to the data. We calculated the distribution of the errors as a function of the distance from the cluster centre. To be conservative, the values we adopted for the errors are the maximum in each band, measured close to the cluster centre.

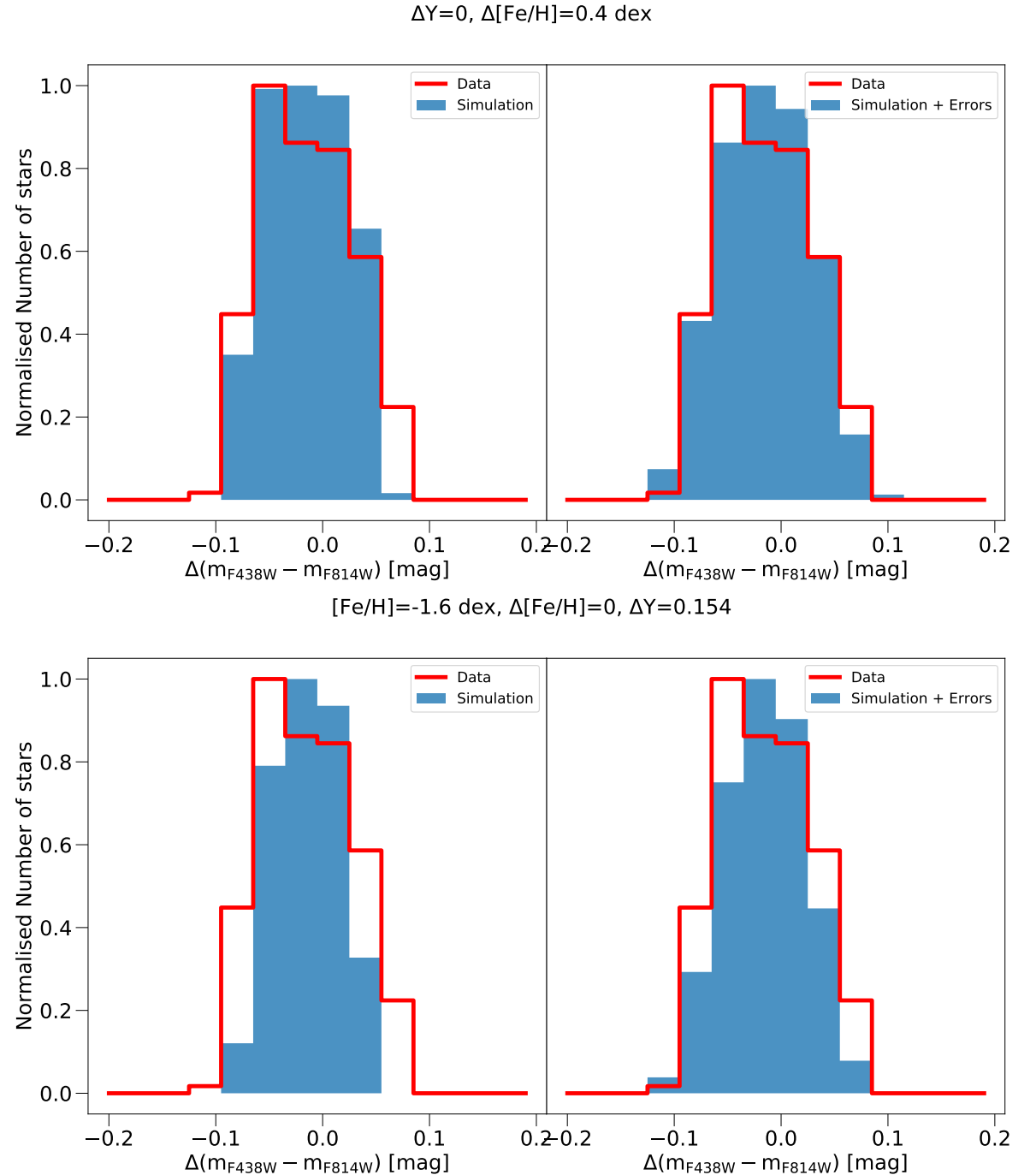


Figure 6.7: Histograms of verticalised  $m_{\text{F}438\text{W}} - m_{\text{F}814\text{W}}$  colours vs.  $m_{\text{F}438\text{W}}$  magnitudes for observed (red) and simulated (blue filled) RGB stars for  $\Delta Y=0$ ,  $\Delta[\text{Fe/H}] = +0.4 \text{ dex}$  (top panels) and  $\Delta Y=0.154$ ,  $\Delta[\text{Fe/H}] = 0 \text{ dex}$  (bottom panels). See text for more details.

observed (red) and simulated (blue filled) RGB stars. The histograms are normalised to the maximum of the distributions. The left panel shows the comparison between the data and the simulations when no photometric errors are included. For each spread we performed a KS test to compare the data and simulated distributions. We obtained the highest p-value ( $\sim 65\%$ ) when a spread  $\Delta[\text{Fe}/\text{H}] = +0.4$  dex is employed.

We repeated the same analysis on the RGB assuming now that there is no variation in Fe and investigating the possible presence of a He spread. Therefore we used isochrones at fixed metallicity ( $[\text{Fe}/\text{H}] = -1.6$  dex) with different He content. We generated 500 isochrones with a uniform distribution in He, ranging from  $\text{Y}=0.246$  to  $\text{Y}=0.4$ . We repeated exactly the same steps described above and we show the results in the bottom panels of Fig. 6.7. To reproduce the observed width of the RGB, at least a  $\Delta\text{Y}=0.154$  is needed. While probably an even larger He variation would allow a better match with the observed RGB width, this is the maximum spread we can obtain with the available set of models.

It is important to stress that, when comparing observations to simulations that include errors estimated from the AS, such errors may be underestimated, thus the values we report for  $\Delta[\text{Fe}/\text{H}]$  and  $\Delta\text{Y}$  are upper limits. The main reason is that all AS experiments are simplified to some extent and they are not able to account for all the instrumental sources of noise. The typical difference between errors from AS and true observational uncertainties has been estimated in previous studies and is of the order of 30 – 40% (see Fig. 4 of [Dalessandro et al. 2011a](#) and related text and Fig. 21 of [Milone et al. 2012](#)). We repeated the same analysis above by using errors that are 30% larger. According to the KS test, we still found that the simulated distributions that best reproduce the observations are the ones having  $\Delta[\text{Fe}/\text{H}] = +0.4$  dex ( $\Delta\text{Y}=0$ ), and  $\Delta\text{Y}=0.154$  ( $\Delta[\text{Fe}/\text{H}]=0$ ).

We can therefore safely conclude that either Fornax 4 hosts stars with significantly different metallicity, with a total iron abundance spread of  $\Delta[\text{Fe}/\text{H}] = +0.4$  dex, or stellar sub-populations with large He variations for a total  $\Delta\text{Y}=0.154$ . A combination of sub-populations with smaller variations of Fe and He can also match the observed RGB colour distribution. For instance, we reproduced the width of the RGB by making a

simulation that includes a spread in He  $\Delta Y=0.03$  (which will be constrained in the next Section §6.5.2) and a slightly lower iron spread  $\Delta[\text{Fe}/\text{H}] = +0.3$  dex.

### 6.5.2 The Horizontal Branch analysis

To try and constrain better the range of  $Y$  and/or  $[\text{Fe}/\text{H}]$  spanned by the cluster initial chemical composition, we performed a detailed analysis of the horizontal branch, whose morphology is also affected by variations of the initial helium and metal content. To this aim we used the same approach described in [Dalessandro et al. \(2011b, 2013b\)](#) which is based on the comparison between observations and synthetic HB models.

Fornax 4 hosts a relatively large number of variable stars ([Greco et al., 2007](#)), for which we have only observations at a random phase. Thus, before analysing the HB with stellar models, we needed to identify these stars in our catalogue, and remove them from the comparison.

The first identification of variable stars in the Fornax clusters was performed by [Greco et al. \(2007\)](#). By taking  $B$  and  $V$  time series photometry with MagIC on the Magellan Clay Telescope, they found 29 variable stars (out of which, 27 are identified as RR Lyrae), in a  $2.4' \times 2.4'$  area centred on Fornax 4. They claimed that the 22 stars located within the innermost  $30''$  are likely cluster members. Since we have several exposures in each filter in our dataset (§6.2), we used the variability index (VI) yielded by DAOPHOT to check for variable stars. We marked as “variable” all stars having  $\text{VI} > 2$  both in the F438W and F814W band. Figure 6.8 shows a zoomed-in  $m_{\text{F438W}} - m_{\text{F814W}}$  vs.  $m_{\text{F438W}}$  CMD around the HB region. Magenta squares represent the stars that are found to be variable in both bands simultaneously. In total we find 28 variable stars.

We matched our whole Fornax 4 photometric catalogue with the [Greco et al. \(2007\)](#) variable stars catalogue, in order to identify variable stars independently from our method (i.e. the VI index). We find 25 out of 29 stars in common. Of the remaining four, three stars are not in our WFC3 field of view while one star from the [Greco](#)

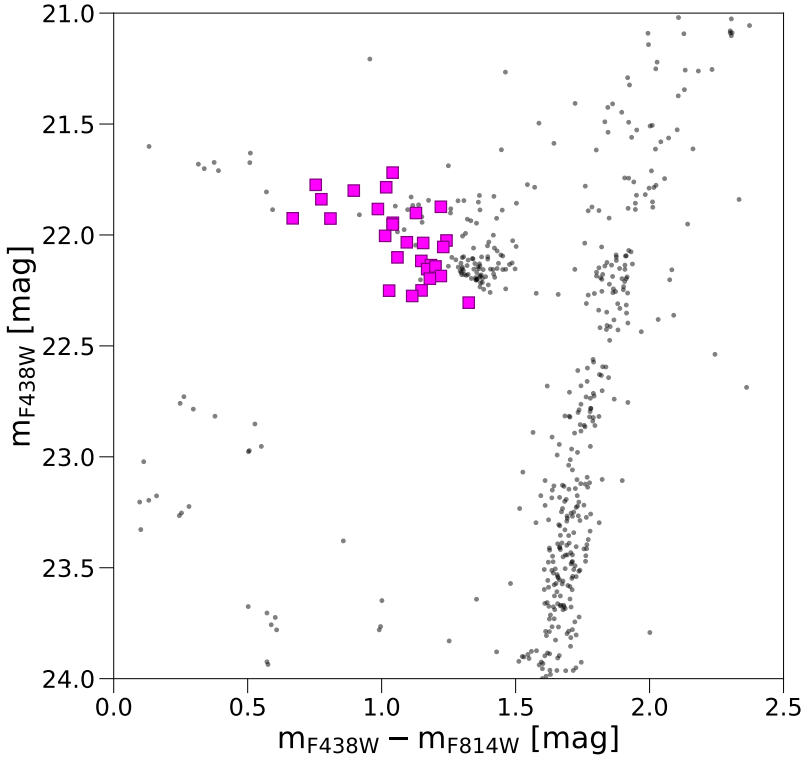


Figure 6.8: Zoomed in  $m_{\text{F}438\text{W}} - m_{\text{F}814\text{W}}$  vs.  $m_{\text{F}438\text{W}}$  CMDs for Fornax 4. Magenta squares represent variable stars identified in this work.

[et al. \(2007\)](#) catalogue is not identified in the match. Out of these 25 stars in common, we were able to identify 19 stars as variables according to the VI index. We then removed all our 28 variable stars (pink squares in Fig. 6.8) from the following analysis.

To assess the impact of He and Fe abundance spreads on the cluster HB we compared the observed  $m_{\text{F}438\text{W}} - m_{\text{F}814\text{W}}$  vs  $m_{\text{F}438\text{W}}$  CMD with synthetic HB models. This technique has been already applied to several Galactic GCs (e.g., [Dalessandro et al. 2011b, 2013b](#)) and also Magellanic Clouds' clusters (e.g. [Niederhofer et al. 2017b, Chantereau et al. 2019](#)). For the synthetic HB calculations we used the BaSTI  $\alpha$ -enhanced HB models ([Pietrinferni et al. 2004, 2006](#)) with metallicity  $[\text{Fe}/\text{H}] = -1.6$  dex, and employed the code described in [Dalessandro et al. \(2013b\)](#). In our simulations with a  $[\text{Fe}/\text{H}]$  spread we have replaced the interpolation in  $Y$  with an interpolation in  $[\text{Fe}/\text{H}]$ , keeping the structure of the code unchanged. After assuming a reference age  $t = 10$  Gyr (that fixes the initial value of the mass currently evolving at the tip of the RGB), the only remaining parameters that determine the mass distribution (hence

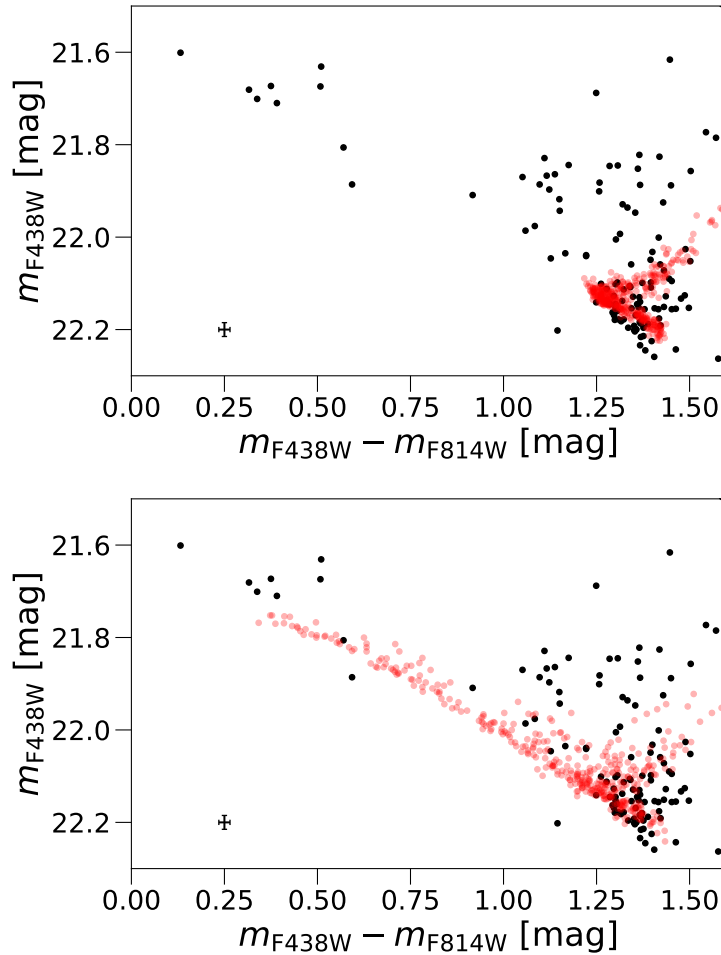


Figure 6.9:  $m_{\text{F}438\text{W}} - m_{\text{F}814\text{W}}$  vs.  $m_{\text{F}438\text{W}}$  CMD of HB stars in Fornax 4. Black circles denote observations while red circles represent synthetic HB stars. The left panel displays a synthetic HB calculated with  $\Delta Y=0$ ,  $\Delta M=0.165 M_{\odot}$  (with Gaussian  $\sigma=0.001 M_{\odot}$  spread) and  $(m-M)_0=20.94$  mag. The right panel shows a synthetic HB calculated with  $\Delta Y=0$ ,  $\Delta M$  between 0.165 and 0.225  $M_{\odot}$  (uniform distribution),  $(m-M)_0=20.94$  mag. Average photometric errors are reported in the lower left corner. See text for more details.

magnitudes and colours) along the synthetic HB are the total mass lost by the RGB progenitors  $\Delta M$ , the range of initial Y ( $\Delta Y$ ) or [Fe/H] ( $\Delta [\text{Fe}/\text{H}]$ ) values, and their statistical distribution. In our simulations we also input the  $1\sigma$  photometric errors as obtained from the AS test (see §6.2.1). We notice that in terms of the mass distribution along the synthetic HB a variation of the cluster age can be compensated by changing  $\Delta M$ . For example, an age increase by 1 Gyr is compensated by a  $\sim 0.02M_{\odot}$  decrease of  $\Delta M$ .

As a first test, we checked whether a match of the observed HB morphology with theoretical models requires a spread of initial chemical composition. To this purpose, we have first calculated a synthetic HB with a small RGB mass loss,  $\Delta M=0.165M_{\odot}$  (and a Gaussian  $\sigma$  spread equal to  $0.001M_{\odot}$ ). We assumed the same  $E(B-V)=0.04$  mag employed in the isochrone fitting, and determined a cluster distance modulus by matching the peak of the number distribution of synthetic stars' magnitudes, to the observed one in the  $m_{\text{F}438\text{W}} - m_{\text{F}814\text{W}}$  colour range between 1.25 and 1.45 mag (the well populated red end of the observed HB distribution). In this way we have fixed the distance modulus also for the other simulations that follow. From the left panel of Fig. 6.9, it is obvious that this simulation is not able to reproduce the full colour and magnitude extension of the observed HB. Hence, the right panel of Fig. 6.9 shows another synthetic HB, this time calculated with  $\Delta M$  uniformly distributed between  $0.165M_{\odot}$  and  $0.225M_{\odot}$ , e.g. with a much larger mass loss spread. The colour extension is now well reproduced, but the synthetic HB is too faint to match the stars observed between  $m_{\text{F}438\text{W}} - m_{\text{F}814\text{W}}=0.25$  and 0.50. In these simulations and the ones that follow, the observed star count distribution as a function of colour is different from the synthetic ones. This is however not essential for our purposes, as we are not trying to perform a best fit of the HB. This would be impossible given that the instability strip of the observed HB is depopulated, because we removed RR Lyrae variables for which we lack average magnitude measurements. The goal of this analysis is to test whether the initial chemical composition scenarios inferred from the RGB are broadly consistent with the observed HB morphology.

As a second step we have examined whether the cluster HB can be reproduced by

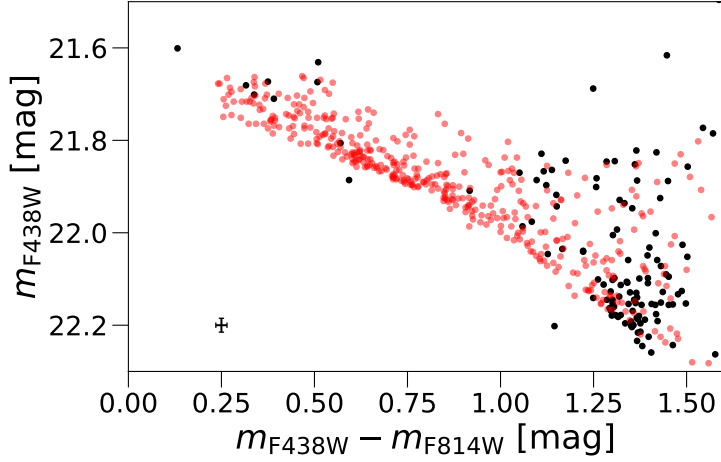


Figure 6.10: As Fig. 6.9, but the synthetic model is calculated with a spread in iron  $\Delta[\text{Fe}/\text{H}] = +0.4$  dex (uniform distribution),  $\Delta Y = 0$ ,  $\Delta M = 0.23 + 0.06([\text{Fe}/\text{H}] + 1.62)\text{M}_\odot$ ,  $(m - M)_0 = 20.86$  mag. See text for more details.

models with constant  $Y=0.246$  and  $\Delta[\text{Fe}/\text{H}] \sim +0.4$  dex, as derived from the RGB colour distribution. To this aim we have calculated a synthetic HB with a uniform probability  $[\text{Fe}/\text{H}]$  distribution between  $[\text{Fe}/\text{H}] = -1.62$  dex and  $[\text{Fe}/\text{H}] = -1.22$  dex, and a mass loss that increases linearly with  $[\text{Fe}/\text{H}]$  as  $\Delta M = 0.23 + 0.06([\text{Fe}/\text{H}] = +1.62)\text{M}_\odot$ , and a  $1\sigma$  Gaussian dispersion of  $0.005\text{M}_\odot$  around this mean relationship. This comparison is shown in Figure 6.10. A constant mass loss irrespective of  $[\text{Fe}/\text{H}]$  produces a HB too extended in colour compared to the observations. Notice that in case of a  $[\text{Fe}/\text{H}]$  spread the metal poor component is located at the blue end of the synthetic HB.

We have then checked whether models with a range of initial He abundances  $\Delta Y$  (at constant  $[\text{Fe}/\text{H}]$ ) compatible with the RGB constraint can also match the observed HB of Fornax 4. Figure 6.11 compares the observed HB with a synthetic one calculated including a He spread  $\Delta Y = 0.03$  (uniform probability distribution), and  $\Delta M = 0.160\text{M}_\odot$  and Gaussian distribution with  $\sigma = 0.003\text{M}_\odot$ . The observed HB is overall well matched with this small value of  $\Delta Y$ , totally incompatible with the large  $\Delta Y$  (at fixed  $[\text{Fe}/\text{H}]$ ) inferred from the RGB. To make this point even clearer, the same figure shows for comparison also the zero age horizontal branch (ZAHB) for both  $Y = 0.246$  and  $Y = 0.40$ . The  $Y = 0.40$  ZAHB is extremely overluminous compared to the data.

From this simple analysis, we are able to establish that a small spread of initial He

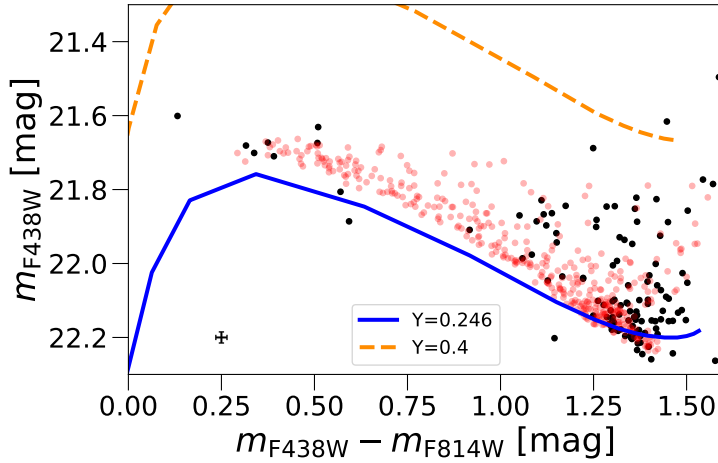


Figure 6.11: As Fig. 6.9, but the synthetic HB stars are calculated with  $\Delta Y=0.03$  (uniform distribution),  $\Delta M=0.160 M_{\odot}$  (Gaussian distribution with  $\sigma=0.003 M_{\odot}$ ), and  $(m-M)_0=20.98$  mag. The solid blue and dashed orange curves represent the ZAHB for  $Y=0.246$  and  $Y=0.4$  at  $[\text{Fe}/\text{H}]=-1.6$  dex, respectively. See text for more details.

abundances (up to  $\Delta Y=0.03$ ) can also reproduce the shape of the HB of Fornax 4, but this spread is much lower than what derived from the RGB, assuming a constant  $[\text{Fe}/\text{H}]$ .

The only way to achieve consistency between the RGB width and the HB morphology of Fornax 4 is to invoke either an initial spread of  $[\text{Fe}/\text{H}]$  (of about 0.4 dex) at constant  $Y$ , or both a small spread of  $Y$  ( $\Delta Y$  up to  $\sim 0.03$ ) and a spread of  $[\text{Fe}/\text{H}]$  of less than  $\sim 0.4$  dex. As an example, in Sect. §6.5.1 we have also reported that the width of the RGB can be reproduced by a combination of a spread in He  $\Delta Y=0.03$  and slightly less iron spread  $\Delta [\text{Fe}/\text{H}]=+0.3$  dex.

## 6.6 Discussion

In this Chapter we investigated the nature of Fornax 4 by characterizing its stellar population properties. Indeed, because of its position, metallicity and age, this system has been suggested to be the nucleus of the Fornax dSph galaxy (e.g. [Hardy 2002](#); [Strader et al. 2003](#)).

By using archival HST/WFC3 observations, we confirm that Fornax 4 is younger than

the other clusters in the galaxy. In fact, we find the age of Fornax 4 is of the order of  $t = 11$  Gyr (or  $t = 10$  Gyr if  $\alpha$ -enhancement is present within the cluster). We also find that Fornax 4 is more metal-rich than what previously found by Buonanno et al. (1999) ( $[\text{Fe}/\text{H}] = -1.5/-1.6$  dex) using optical CMDs, and in agreement with previous integrated light spectroscopic studies (Strader et al., 2003; Larsen, Strader & Brodie, 2012a).

We performed a detailed analysis of both the RGB and HB of Fornax 4 by means of a comparison between observations and synthetic CMDs. We find that the RGB and HB morphology can be simultaneously reproduced either by assuming the presence of sub-populations with a spread in iron  $\Delta[\text{Fe}/\text{H}] \sim 0.4$  dex or a combination of a slightly milder Fe spread and a variation of He abundance of  $\Delta Y \sim 0.03$  (see §6.5.1, §6.5.2). While the exact amount of these variations may depend on model assumptions and the exact modeling of the photometric errors, this analysis clearly shows that *a non-negligible iron spread is needed to reproduce the stellar population properties of Fornax 4*. This is a key information to assess the nature of this system. In fact, this result, in combination with its metallicity, position and age, provides support to the possibility that Fornax 4 is the NSC of the Fornax dSph.

The most common scenarios invoke that NSCs form in-situ from the galaxy's central gas reservoir (e.g. Bekki 2007; Antonini, Barausse & Silk 2015; Fahrion et al. 2019), or through GCs merging (e.g. Tremaine, Ostriker & Spitzer 1975; Agarwal & Milosavljević 2011; Arca-Sedda & Capuzzo-Dolcetta 2014), or through a combination of these (e.g. Hartmann et al. 2011; Antonini, Barausse & Silk 2015; Guillard, Emsellem & Renaud 2016). While the exact formation of NSCs is still debated (see Neumayer, Seth & Boeker 2020 for a recent review), the general expected outcome is a system located at the center of the host galaxy which is characterized by the presence of sub-populations differing in terms of their iron abundances (e.g. Bekki & Freeman 2003; Bellazzini et al. 2008). Additionally, typical NSCs have a more extended star formation history and some contribution from younger stars (e.g. Walcher et al. 2005; Kacharov et al. 2018). This seems not to be the case for Fornax 4, however it is currently not possible to establish this with the current data available. Indeed, the star

formation history of Fornax was recently derived by [Rusakov et al. \(2020\)](#) showing predominant intermediate age and old population (5 – 10 Gyr). If Fornax 4 sank in the centre of the galaxy less than  $\sim$ 5 Gyr ago, it would not have had much chance to accrete a substantial amount of gas and thus form additional stars.

Interestingly, it seems that Fornax 4 does not reside exactly in the kinematic centre of the galaxy, contrary to what it is found for M54, for instance. [Hendricks et al. \(2014\)](#) calculated the radial velocity (RV) of the Fornax dSph and this results to be  $\sim$ 9 km/s higher than the RV of Fornax 4 (see [Hendricks et al. 2016](#) for a more detailed discussion). Nonetheless, if the infalling of GCs is the dominant formation mechanism, finding a kinematic misalignment between the NSC and the center of the galaxy is expected (e.g. [Capuzzo-Dolcetta & Miocchi 2008](#); [Feldmeier et al. 2014](#)).

While the interpretative scenario of Fornax 4 as the nucleus of the dwarf galaxy is extremely fascinating, it is necessary to confirm this result by performing a detailed spectroscopic and kinematic study of resolved member stars within the GC. It is important to note, in fact, that only one likely member star in the cluster has been analysed spectroscopically ([Hendricks et al., 2016](#)) so far. This would provide a quantitative and reliable measurement of its stellar population chemical and kinematical patterns thus allowing a critical assessment of its formation and early evolution (see e.g. [Sills et al. 2019](#); [Alfaro-Cuello et al. 2019](#)), and more in general on the process on NSC formation and galaxy nucleation, being the second closest case after M54 ([Bellazzini et al., 2008](#)).

# Chapter 7

## Conclusions and Future Work

### 7.1 Conclusions

The main goal of this thesis has been to place fresh and new constraints on theories for the origin of multiple populations in star clusters. This has been performed by expanding the parameter space where MPs are found, especially focussing on cluster age and mass. Since most of the previous MPs studies were performed on old clusters ( $> 10$  Gyr), the natural question to ask is: are chemical anomalies only restricted to the ancient GCs?

In the previous chapters, I presented the results from two joint surveys. Our HST photometric survey is composed of 13 star clusters both in the LMC and SMC. They are massive ( $>$  a few times  $10^4 M_\odot$ ) and they span a very wide range of ages (from  $\sim 1.5$  up to  $\sim 10$  Gyr). This is combined with a spectroscopic survey, which is composed by ESO-VLT FORS2 observations of four star clusters in the Magellanic Clouds, spanning ages from  $\sim 2$  up to  $\sim 8$  Gyr. Three new clusters were also just observed in September 2019 (age=  $1.5 - 2$  Gyr) with FORS2 (see next Section §7.2). The goal of the survey is to search for a potential dependence on the onset of multiple population on cluster age, by looking at clusters that are as massive as the ancient GCs, but significantly younger. Our photometric technique consisted in studying the RGB stars

in filters that are sensitive to N variations, as they encompass the NH molecular band (namely the HST F336W and F343N filters, see Chapter 2). Expanding the search for MPs towards different cluster ages is of extreme importance in order to potentially obtain new constraints for the formation mechanisms, aiming at explaining the origin of chemical anomalies.

The first important result we obtained is the discovery of chemical anomalies as N variations in intermediate age clusters, i.e. aged  $\sim 6 - 7.5$  Gyr, both photometrically and spectroscopically. This corresponds to a redshift of formation for the MPs of  $z = 0.75$ .

We then looked at the younger clusters. We did not find photometric evidence for MPs in clusters that are younger than 2 Gyr ( $\sim 1.5 - 1.7$  Gyr). However, we finally looked at MPs in star clusters in the age gap between 2 and 6 Gyr: two  $\sim 2$  Gyr old clusters, two aged  $\sim 2.5$  Gyr, and a 4 Gyr old one. We found MPs in the form of N variations in all of these clusters. We did not find evidence for chemical anomalies in Lindsay 38 though, a  $\sim 6.5$  Gyr old, but quite low mass cluster ( $\lesssim 2 \times 10^4 M_\odot$ ).

The main results from our surveys are shown in Fig. 7.1, where an updated version of the cluster mass versus cluster age diagram is shown.

The main results are summarised and commented below:

- **MPs in the form of N spreads were observed in intermediate age stars clusters down to  $\sim 2$  Gyr**, which corresponds to a redshift of formation for MPs  $z_{form}=0.17$ . We found MPs in nearly all the intermediate age clusters down to an age of  $\sim 2$  Gyr, implying that MPs in the form of N spreads are *not* only restricted to the ancient GCs. This means that the mechanism responsible for the onset of MPs must have acted at least down to a redshift of  $\sim 0.17$ , hence it is unlikely that special conditions only present in the early Universe are the main drivers for the formation of MPs (see §3.3, D’Ercole, D’Antona & Vesperini 2016). However, it does not seem to be the case for clusters that are younger than 2 Gyr, as they do not show MPs in the form of N spreads. The reason for this is still under

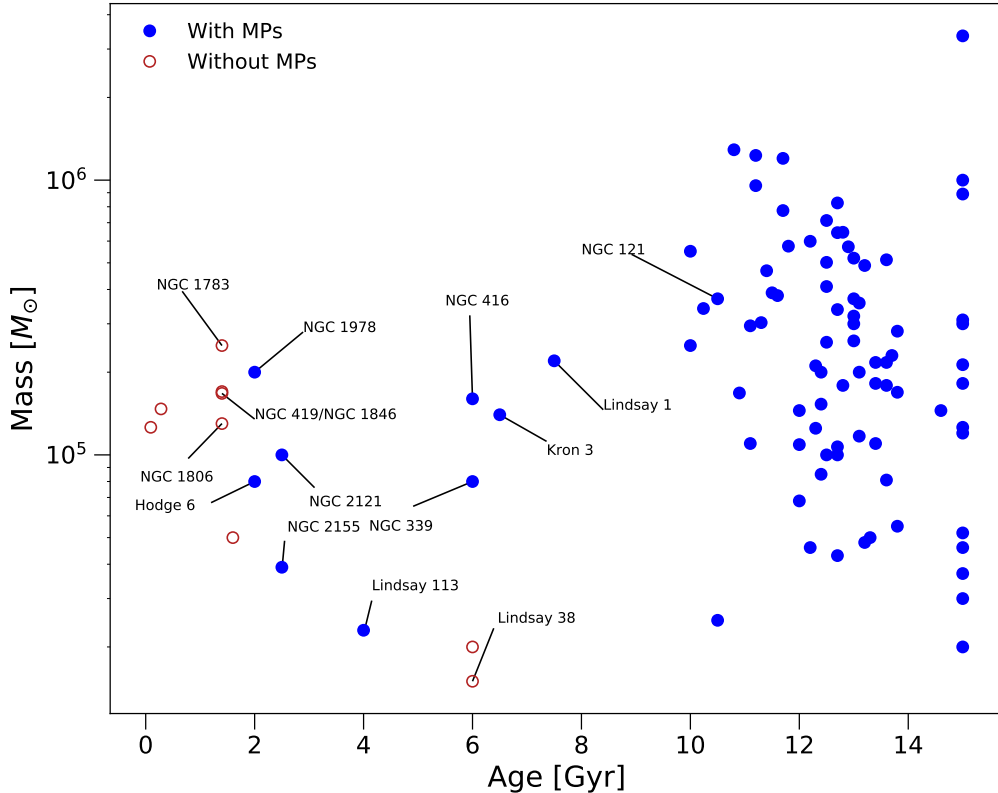


Figure 7.1: Final cluster mass versus cluster age diagram. The clusters from our sample are labeled. Blue filled (red open) circles represent sources with (without) multiple populations. See the compilation by [Krause et al. \(2016\)](#) and references therein.

investigation. By looking at RGB stars at different ages, we are also sampling stars with different stellar masses. RGB stars in a  $\sim 2$  Gyr old population are less massive than  $1.5 M_{\odot}$ , while they become more massive than  $1.5 M_{\odot}$  for populations younger than 2 Gyr. It would then be interesting to investigate whether this threshold is connected to other phenomena; indeed, stars below this mass threshold can be magnetically braked ([Cardini & Cassatella, 2007](#)). Also, the extended main sequence turnoff feature appears below this age threshold ( $\sim 2$  Gyr) in star clusters, but there are no hints of a correlation between this phenomenon and chemical anomalies to date. Another interesting implication from these results is that for the first time multiple stellar populations are detected in intermediate age clusters down to such a young age ( $\sim 2$  Gyr). As described in Chapter 1, ancient GCs and YMCs overlap in all their global properties, such as cluster masses, sizes and densities. However, the lack of the distinctive chemical

abundance variations in the younger clusters led many to consider the formation of old GCs unique to the special conditions found in the early Universe (e.g. [Trenti, Padoan & Jimenez 2015](#)). The results presented in this thesis suggest that the formation and evolution of YMCs and ancient GCs might instead happen through the same channel ([Kruijssen, 2015](#); [Pfeffer et al., 2018](#); [Kruijssen et al., 2019](#)).

- **No age difference is observed between the MPs of young star clusters.** Discovering and studying MPs in younger clusters allowed to place very stringent limits on any age spread between the different populations present in such objects (see Chapter 4). Indeed, works focused on ancient GCs were only able to put upper limits of  $\sim 200$  Myr ([Marino et al., 2012](#); [Nardiello et al., 2015](#)). By taking advantage of the youth of NGC 1978, we find that the two populations present in this cluster are coeval, i.e. they were formed at the same time or their age difference is very small. In a more recent work, we also confirm this result in another intermediate-age cluster in our HST sample, namely NGC 2121 ([Sarcino et al., 2020](#)). These results are crucial for models that aim at explaining the formation of MPs, as they predict a range of expected age differences among the constituent populations within a cluster. For instance, self-enrichment models that advocate AGB stars as polluters are not consistent with the constraints found in this work. AGB stars need at least 30 Myr to evolve and potentially more time is needed to form a second generation within the cluster. On the other hand, models that invoke very massive and/or fast rotating massive stars ( $> 15 M_{\odot}$ ), are still consistent with these new constraints.
- **We observe a correlation between N spread and age of the clusters** (Chapter 5), which is not predicted by any scenario proposed for the formation of MPs. We examined how the width of the RGB in the clusters varies as a function of cluster age and we found that older clusters show larger abundance spreads compared to the younger clusters. The role of age is currently unknown and under investigation, but the observations might point towards a stellar evolutionary effect. I expand more on this in the next Section 7.2.

- **We find a very tight TO in NGC 1978** (see Chapter 4). This finding lends support to the stellar rotation scenario for the origin of the eMSTO (see [Bastian & de Mink 2009](#)). Indeed, stars at the TO in  $\sim 2$  Gyr old populations are below  $\sim 1.5M_{\odot}$ . Below this mass, stars become magnetically braked and slow down. This is what is predicted by [Brandt & Huang \(2015\)](#) and [Georgy et al. \(2019\)](#), i.e. after an age of  $\sim 2$  Gyr star clusters are not expected to show an eMSTO feature.

## 7.2 Avenues for Future Study

Through the study presented in this thesis, I have demonstrated that intermediate age clusters host MPs in the form of N spreads within their RGB stars. Nevertheless, open questions remain whether such objects might have the exact same stellar populations present in the ancient GCs. Indeed, old GCs exhibit specific chemical abundance patterns still not observed in their younger counterparts, i.e. Na-O (possibly Mg-Al) anti-correlations. Future steps definitely involve the full chemical characterisation of young star clusters, as so far we have explored only N variations (and He to a certain extent, [Chantereau et al. 2019](#); [Lagioia et al. 2019](#)).

However, Na and O abundances in intermediate age star clusters in the LMC were estimated by [Mucciarelli et al. \(2008, 2014\)](#) and they found no spread both in Na and O, although their sample was based on a relatively small number of stars. Most of their targets are younger than  $\sim 2$  Gyr, where we also do not observe N spreads. However, they also find no Na-O anti-correlation in the  $\sim 2$  Gyr cluster NGC 1978, which does show N spreads (Chapter 3). Additionally, there have been quite a few studies based on integrated light techniques. [Cabrera-Ziri et al. \(2016b\)](#); [Lardo et al. \(2017\)](#) looked for Na and Al anomalies but did not find any in very young clusters ( $< 40$  Myr). Very recently, [Bastian et al. \(2019\)](#) found chemical anomalies in the form of Na spreads in G114, a very massive ( $> 10^7 M_{\odot}$ ) star cluster in the NGC 1316 galaxy. They also did not find Na spreads in NGC 1978. Additionally, no Na spreads are reported for two young star clusters ( $\sim 600$  Myr old) in the merger remnant NGC 7252, even though

they are very massive ( $\sim 10^7 - 10^8 M_{\odot}$ , [Bastian et al. 2020](#)).

Integrated light techniques are very powerful as they allow us to analyse the chemical composition of stars in distant clusters. However, they cannot tell us all the details, e.g. how the different populations are spatially segregated or the fraction of anomalous stars with respect to the field-like ones.

Our group has recently obtained ESO VLT/MUSE ([Bacon et al., 2010](#)) time to study 5 massive, intermediate age clusters in the MCs. MUSE data will allow a very promising and innovative way of studying MPs in star clusters (e.g. [Latour et al. 2019](#)). The studies mentioned above by [Mucciarelli et al. 2014](#) that searched for Na and Al spreads in MCs intermediate age clusters were based on high resolution spectroscopy with GIRAFFE and UVES at the VLT ([Pasquini et al., 2002](#)). However, this limited the observations to the outer regions of clusters due to crowding in the inner regions, and to bright RGB stars, due to the higher spectral resolution. MUSE opens the possibility to (i) estimate the abundance of stars located in the most crowded regions of the cluster, thanks to the sensitivity of AO assisted observations combined with the power of PampelMuse spectra extraction software ([Kamann, Wisotzki & Roth, 2013](#)), (ii) obtain such estimates for hundreds to thousands of stars instead of a few 10s. This will allow us to study chemical patterns in young clusters for many elements that have not been yet explored at such a young age (e.g., Na, Mg and many other alpha and iron-peak elements). While the lower resolution of MUSE makes it challenging to measure individual abundances of stars, it has recently been demonstrated that with high S/N data it is possible, see [Latour et al. \(2019\)](#). Additionally, MUSE will also give hints on the kinematic difference between the populations present in a given cluster ([Hénault-Brunet et al., 2015](#)), which will provide fundamental insights into distinguishing different formation scenarios for MPs.

The second main result from this thesis is the correlation between N spreads and age of the cluster (Chapter 5), which deserves further investigation. This dependence on age is not predicted by any model that has been proposed to explain the formation and evolution of MPs. Hence, converting the photometrically determined correlation between cluster age and N spread into a spectroscopic counterpart is a crucial constraint

for the developments of new quantitative scenarios for the origin of MPs. We already have VLT/FORS2 spectroscopic data for three intermediate age (2-8 Gyr old) clusters (Hollyhead et al., 2017, 2018, 2019) and I just obtained data for other 3 clusters which are between 1.5 and 2 Gyr old. Furthermore, FORS observations of RGB stars in old ( $>9$  Gyr) Milky Way clusters are available in the ESO archive (Pancino et al., 2010), for which C and N abundances can be measured as well. For these ancient clusters, the [N/Fe] spread is expected to be large, of the order of  $\sim 1.5\text{-}2$  dex, as seen from already available measurements carried out by using different instruments (e.g., Lardo et al. 2012). This sample will also be used to investigate dependencies of the relation on factors such as metallicity and cluster mass. The combination of these datasets will enable a systematic and homogeneous study and will allow us to obtain the first spectroscopic counterpart of the N vs. age correlation, covering a very wide range of ages (from  $\sim 1.5$  up to  $> 10$  Gyr).

Interestingly, in a recent work, Salaris et al. (2020) explored the effect of the first-dredge up (FDU) on the widths of the RGB of star clusters showing MPs, in typical photometric pseudo-colours sensitive to N-variations also presented in this thesis (e.g.  $C_{F336W,F438W,F343N}$ ,  $C_{F343N,F438W,F814W}$ ). The FDU involves the dredge up to the stellar surface of matter burnt in the core by H fusion, due to the convective zone penetrating deeper and deeper towards the core. The corresponding change of surface N abundance depends on the initial N abundance but also on the mass of the star, hence its age (Salaris et al., 2015). Salaris et al. (2020) found that the FDU reduces the widths of the RGB (for a given amount of initial abundance differences between the populations) and that this is a strong function of age. This is crucial as it means that what we are estimating from the RGB widths of star clusters is a N spread that has been modified by the FDU and would lead to an underestimation of the initial N abundance variation. This might also explain why MPs are not observed in clusters younger than 2 Gyr, although the FDU cannot account for the total extent of the correlation between N spreads and cluster age (Chapter 5). Hence, the observed correlation between cluster age and N spread is a combination of initial N spreads and the effect of the FDU.

It would then be critical to estimate the *initial* N abundances, i.e. not affected by the

FDU and evolutionary effects, as a function of cluster age. A pilot study has recently been performed by Cabrera-Ziri et al., submitted. We looked for abundance variations in the MS of the  $\sim 1.5$  Gyr old, massive ( $\sim 10^5 M_\odot$ ) cluster NGC 419 (see Chapter 2), making a comparison with Galactic GCs such as 47 Tuc, NGC 6352 and NGC 6637 which have similar metallicities ([Fe/H] =  $-0.7$  dex). We used HST photometry to analyse MS stars that have the same range in stellar masses of stars where MPs are found in old GCs, i.e.  $\sim 0.75 - 1.05 M_\odot$ . We found that the colour distributions of NGC 419 in the lower MS are consistent with what is expected from a cluster with homogeneous abundances. However, the sensitivity of the current dataset cannot exclude small initial abundance variations. It is thus necessary to probe a dependency on mass and age by expanding the sample to other clusters. The HST or the upcoming James Webb Space Telescope will be the facilities necessary for such future follow-up studies.

# Bibliography

- Adamo A., Bastian N., 2015, arXiv e-prints, arXiv:1511.08212
- Adamo A., Kruijssen J. M. D., Bastian N., Silva-Villa E., Ryon J., 2015, MNRAS, 452, 246
- Agarwal M., Milosavljević M., 2011, ApJ, 729, 35
- Akaike H., 1974, IEEE Transactions on Automatic Control, 19, 716
- Alfaro-Cuello M. et al., 2019, ApJ, 886, 57
- Antonini F., Barausse E., Silk J., 2015, ApJ, 812, 72
- Arca-Sedda M., Capuzzo-Dolcetta R., 2014, MNRAS, 444, 3738
- Asplund M., Grevesse N., Sauval A., Scott P., 2009, ARAstron. Astrophys., 47, 481
- Bacon R. et al., 2010, Society of Photo-Optical Instrumentation Engineers (SPIE) Conference Series, Vol. 7735, The MUSE second-generation VLT instrument, p. 773508
- Bastian N., Cabrera-Ziri I., Davies B., Larsen S., 2013a, MNRAS, 436, 2852
- Bastian N. et al., 2017, MNRAS, 465, 4795
- Bastian N., Cabrera-Ziri I., Salaris M., 2015, MNRAS, 449, 3333
- Bastian N., de Mink S., 2009, MNRAS, 398, L11
- Bastian N., Kamann S., Cabrera-Ziri I., Georgy C., Ekström S., Charbonnel C., de Juan Ovelar M., Usher C., 2018, MNRAS, 480, 3739

- Bastian N., Lamers H. J. G. L. M., de Mink S. E., Longmore S. N., Goodwin S. P., Gieles M., 2013b, MNRAS, 436, 2398
- Bastian N., Lardo C., 2018, ARA&A, 56, 83
- Bastian N. et al., 2020, arXiv e-prints, arXiv:2003.03428
- Bastian N. et al., 2016, MNRAS, 460, L20
- Bastian N. et al., 2019, MNRAS, 489, L80
- Baumgardt H., Hilker M., 2018, MNRAS, 478, 1520
- Baumgardt H., Hilker M., Sollima A., Bellini A., 2019, MNRAS, 482, 5138
- Baumgardt H., Makino J., 2003, MNRAS, 340, 227
- Bedin L. R., Piotto G., Anderson J., Cassisi S., King I. R., Momany Y., Carraro G., 2004, ApJL, 605, L125
- Bedin L. R., Piotto G., Zoccali M., Stetson P. B., Saviane I., Cassisi S., Bono G., 2000, A&A, 363, 159
- Bekki K., 2007, PASA, 24, 77
- Bekki K., Freeman K. C., 2003, MNRAS, 346, L11
- Bellazzini M., Fusi Pecci F., Montegriffo P., Messineo M., Monaco L., Rood R. T., 2002, AJ, 123, 2541
- Bellazzini M. et al., 2008, AJ, 136, 1147
- Bertelli G., Girardi L., Marigo P., Nasi E., 2008, A&A, 484, 815
- Bertelli G., Nasi E., Girardi L., Chiosi C., Zoccali M., Gallart C., 2003, AJ, 125, 770
- Billett O. H., Hunter D. A., Elmegreen B. G., 2002, AJ, 123, 1454
- Böker T., Laine S., van der Marel R. P., Sarzi M., Rix H.-W., Ho L. C., Shields J. C., 2002, AJ, 123, 1389

- Bragaglia A., Gratton R. G., Carretta E., D’Orazi V., Sneden C., Lucatello S., 2012, *A&A*, 548, A122
- Brandt T. D., Huang C. X., 2015, *ApJ*, 807, 25
- Breen P. G., 2018, *MNRAS*, 481, L110
- Brodie J., Strader J., 2006a, *ARAstron. Astrophys.*, 44, 193
- Brodie J. P., Strader J., 2006b, *ARA&A*, 44, 193
- Brown J., Wallerstein G., Oke J., 1991, *AJ*, 101, 1693
- Buonanno R., Corsi C. E., Castellani M., Marconi G., Fusi Pecci F., Zinn R., 1999, *AJ*, 118, 1671
- Cabrera-Ziri I., Bastian N., Davies B., Magris G., Bruzual G., Schweizer F., 2014, *MNRAS*, 441, 2754
- Cabrera-Ziri I. et al., 2016a, *MNRAS*, 457, 809
- Cabrera-Ziri I. et al., 2015, *MNRAS*, 448, 2224
- Cabrera-Ziri I., Lardo C., Davies B., Bastian N., Beccari G., Larsen S. S., Hernandez S., 2016b, *MNRAS*, 460, 1869
- Cannon R., Croke B., Bell R., Hesser J., Stathakis R., 1998, *MNRAS*, 298, 601
- Capuzzo-Dolcetta R., Miocchi P., 2008, *MNRAS*, 388, L69
- Cardini D., Cassatella A., 2007, *ApJ*, 666, 393
- Carretta E., Bragaglia A., Gratton R., Lucatello S., 2009a, *A&A*, 505, 139
- Carretta E. et al., 2009b, *Astron. Astrophys.*, 505, 117
- Carretta E., Bragaglia A., Gratton R., Recio-Blanco A., Lucatello S., D’Orazi V., Cassisi S., 2010, *Astron. Astrophys.*, 516, A55
- Carretta E. et al., 2014, *A&A*, 564, A60

- Carretta E., Gratton R. G., Lucatello S., Bragaglia A., Bonifacio P., 2005, *A&A*, 433, 597
- Chantereau W., Salaris M., Bastian N., Martocchia S., 2019, *MNRAS*, 484, 5236
- Choi J., Dotter A., Conroy C., Cantiello M., Paxton B., Johnson B., 2016, *ApJ*, 823, 102
- Cohen J., Meléndez J., 2005, *AJ*, 129, 303
- Cohen J. G., 2004, *AJ*, 127, 1545
- Colucci J. E., Bernstein R. A., Cameron S. A., McWilliam A., 2012, *ApJ*, 746, 29
- Conroy C., 2012, *ApJ*, 758, 21
- Conroy C., Spergel D. N., 2011, *ApJ*, 726, 36
- Cordoni G., Milone A. P., Mastrobuono-Battisti A., Marino A. F., Lagioia E. P., Tailo M., 2019, arXiv e-prints, arXiv:1908.11692
- Corsaro E. et al., 2017, *Nature Astronomy*, 1, 0064
- Cottrell P. L., Da Costa G. S., 1981, *ApJL*, 245, L79
- Crowther P. A. et al., 2016, *MNRAS*, 458, 624
- Da Costa G. S., Hatzidimitriou D., 1998, *AJ*, 115, 1934
- Dalessandro E., Ferraro F. R., Bastian N., Cadelano M., Lanzoni B., Raso S., 2019, *A&A*, 621, A45
- Dalessandro E., Ferraro F. R., Massari D., Lanzoni B., Miocchi P., Beccari G., 2015, *ApJ*, 810, 40
- Dalessandro E. et al., 2013a, *ApJ*, 778, 135
- Dalessandro E., Lanzoni B., Beccari G., Sollima A., Ferraro F. R., Pasquato M., 2011a, *ApJ*, 743, 11

- Dalessandro E., Lapenna E., Mucciarelli A., Origlia L., Ferraro F., Lanzoni B., 2016, *ApJ*, 829, 77
- Dalessandro E. et al., 2018, *A&A*, 618, A131
- Dalessandro E. et al., 2014, *ApJL*, 791, L4
- Dalessandro E., Salaris M., Ferraro F. R., Cassisi S., Lanzoni B., Rood R. T., Fusi Pecci F., Sabbi E., 2011b, *MNRAS*, 410, 694
- Dalessandro E., Salaris M., Ferraro F. R., Mucciarelli A., Cassisi S., 2013b, *MNRAS*, 430, 459
- D'Antona F., Caloi V., D'Ercole A., Tailo M., Vesperini E., Ventura P., Di Criscienzo M., 2013, *MNRAS*, 434, 1138
- D'Antona F., Di Criscienzo M., Decressin T., Milone A. P., Vesperini E., Ventura P., 2015, *MNRAS*, 453, 2637
- D'Antona F., Ventura P., Decressin T., Vesperini E., D'Ercole A., 2014, *MNRAS*, 443, 3302
- D'Antona F., Vesperini E., D'Ercole A., Ventura P., Milone A. P., Marino A. F., Tailo M., 2016, *MNRAS*, 458, 2122
- de Boer T. J. L., Fraser M., 2016, *A&A*, 590, A35
- de Mink S., Pols O., Langer N., Izzard R., 2009, *Astron. Astrophys.*, 507, L1
- Decressin T., Meynet G., Charbonnel C., Prantzos N., Ekström S., 2007, *Astron. Astrophys.*, 464, 1029
- Denissenkov P. A., Hartwick F. D. A., 2014, *MNRAS*, 437, L21
- D'Ercole A., D'Antona F., Vesperini E., 2016, *MNRAS*, 461, 4088
- D'Ercole A., Vesperini E., D'Antona F., McMillan S., Recchi S., 2008, *MNRAS*, 391, 825

- Dotter A., 2016, ApJS, 222, 8
- Dotter A., Milone A. P., Conroy C., Marino A. F., Sarajedini A., 2018, ApJL, 865, L10
- Dupree A. K. et al., 2017, ApJL, 846, L1
- Efron B., Tibshirani R., 1993, An Introduction to the Bootstrap. Chapman and Hall, New York, London.
- Fahrion K. et al., 2019, A&A, 628, A92
- Fall S. M., Rees M. J., 1985, ApJ, 298, 18
- Feldmeier A. et al., 2014, A&A, 570, A2
- Ferraro F. R., Montegriffo P., Origlia L., Fusi Pecci F., 2000, AJ, 119, 1282
- Ferraro F. R., Mucciarelli A., Carretta E., Origlia L., 2006, ApJL, 645, L33
- Forbes D. A. et al., 2018, Proceedings of the Royal Society of London Series A, 474, 20170616
- Forbes D. A., Forte J. C., 2001, MNRAS, 322, 257
- Gebhardt K., Kissler-Patig M., 1999, AJ, 118, 1526
- Geisler D., Hodge P., 1980, ApJ, 242, 66
- Georgiev I. Y., Puzia T. H., Goudfrooij P., Hilker M., 2010, MNRAS, 406, 1967
- Georgy C. et al., 2019, A&A, 622, A66
- Gieles M. et al., 2018, MNRAS, 478, 2461
- Gilligan C. K. et al., 2019, arXiv e-prints
- Girardi L. et al., 2008, PASP, 120, 583
- Glatt K. et al., 2008a, AJ, 135, 1106
- Glatt K. et al., 2011, AJ, 142, 36

- Glatt K. et al., 2008b, AJ, 136, 1703
- Gossage S. et al., 2019, ApJ, 887, 199
- Göttgens F. et al., 2019, A&A, 631, A118
- Goudfrooij P. et al., 2014, ApJ, 797, 35
- Goudfrooij P., Puzia T. H., Kozhurina-Platais V., Chandar R., 2009, AJ, 137, 4988
- Goudfrooij P., Puzia T. H., Kozhurina-Platais V., Chandar R., 2011, ApJ, 737, 3
- Graczyk D. et al., 2019, ApJ, 872, 85
- Gratton R., Bragaglia A., Carretta E., D’Orazi V., Lucatello S., Sollima A., 2019, A&AR, 27, 8
- Gratton R., Carretta E., Bragaglia A., 2012, Astron. Astrophys.Rv, 20, 50
- Greco C. et al., 2007, ApJ, 670, 332
- Grocholski A. J., Cole A. A., Sarajedini A., Geisler D., Smith V. V., 2006, AJ, 132, 1630
- Guillard N., Emsellem E., Renaud F., 2016, MNRAS, 461, 3620
- Hardy E., 2002, in IAU Symposium, Vol. 207, Extragalactic Star Clusters, Geisler D. P., Grebel E. K., Minniti D., eds., p. 62
- Harris W. E., 1991, ARA&A, 29, 543
- Harris W. E., 1996, VizieR Online Data Catalog, VII/195
- Harris W. E., van den Bergh S., 1981, AJ, 86, 1627
- Hartigan J. A., Hartigan P. M., 1985, The Annals of Statistics, 13, 70
- Hartmann M., Debattista V. P., Seth A., Cappellari M., Quinn T. R., 2011, MNRAS, 418, 2697
- Hénault-Brunet V., Gieles M., Agertz O., Read J. I., 2015, MNRAS, 450, 1164

- Hendricks B., Boeche C., Johnson C. I., Frank M. J., Koch A., Mateo M., Bailey J. I., 2016, *A&A*, 585, A86
- Hendricks B., Koch A., Walker M., Johnson C. I., Peñarrubia J., Gilmore G., 2014, *A&A*, 572, A82
- Hesser J. E., Bell R. A., 1980, *ApJL*, 238, L149
- Hollyhead K., Bastian N., Adamo A., Silva-Villa E., Dale J., Ryon J. E., Gazak Z., 2015, *MNRAS*, 449, 1106
- Hollyhead K. et al., 2017, *MNRAS*, 465, L39
- Hollyhead K. et al., 2018, *MNRAS*, 476, 114
- Hollyhead K. et al., 2019, *MNRAS*, 484, 4718
- Holtzman J. et al., 1992, *AJ*, 103, 691
- Howard C. S., Pudritz R. E., Harris W. E., Sills A., 2018, arXiv e-prints
- Kacharov N., Neumayer N., Seth A. C., Cappellari M., McDermid R., Walcher C. J., Böker T., 2018, *MNRAS*, 480, 1973
- Kamann S. et al., 2020, *MNRAS*, 492, 2177
- Kamann S. et al., 2018, *MNRAS*, 480, 1689
- Kamann S., Wisotzki L., Roth M. M., 2013, *A&A*, 549, A71
- King I. R., 1966, *AJ*, 71, 64
- Kraft R. P., 1979, *ARA&A*, 17, 309
- Krause M., Charbonnel C., Decressin T., Meynet G., Prantzos N., 2013, *A&A*, 552, A121
- Krause M. G. H., Charbonnel C., Bastian N., Diehl R., 2016, *A&A*, 587, A53
- Kruijssen J., 2015, *MNRAS*, 454, 1658

- Kruijssen J. M. D., Mieske S., 2009, A&A, 500, 785
- Kruijssen J. M. D., Pfeffer J. L., Reina-Campos M., Crain R. A., Bastian N., 2019, MNRAS, 486, 3180
- Kurucz R., 1970, SAO Special Report, 309
- Kurucz R., 2005, Memorie della Societa Astronomica Italiana Supplementi, 8, 14
- Kurucz R., Avrett E., 1981, SAO Special Report, 391
- Kurucz R., Furenlid I., 1979, SAO Special Report, 387
- Lagioia E. P., Milone A. P., Marino A. F., Dotter A., 2019, ApJ, 871, 140
- Lamers H. J. G. L. M., Gieles M., Bastian N., Baumgardt H., Kharchenko N. V., Portegies Zwart S., 2005, A&A, 441, 117
- Lamers H. J. G. L. M., Kruijssen J. M. D., Bastian N., Rejkuba M., Hilker M., Kissler-Patig M., 2017, A&A, 606, A85
- Lardo C., Cabrera-Ziri I., Davies B., Bastian N., 2017, MNRAS, 468, 2482
- Lardo C., Pancino E., Mucciarelli A., Milone A. P., 2012, A&A, 548, A107
- Larsen S., Brodie J., Grundahl F., Strader J., 2014a, ApJ, 797, 15
- Larsen S. S., Brodie J. P., Forbes D. A., Strader J., 2014b, A&A, 565, A98
- Larsen S. S., Richtler T., 2000, A&A, 354, 836
- Larsen S. S., Strader J., Brodie J. P., 2012a, A&A, 544, L14
- Larsen S. S., Strader J., Brodie J. P., 2012b, A&A, 544, L14
- Latour M. et al., 2019, A&A, 631, A14
- Li C., de Grijs R., 2019, arXiv e-prints
- Li C., de Grijs R., Deng L., 2014, Nat., 516, 367

- Li H., Gnedin O. Y., Gnedin N. Y., Meng X., Semenov V. A., Kravtsov A. V., 2017, *ApJ*, 834, 69
- Lyubenova M. et al., 2013, *MNRAS*, 431, 3364
- Mackey A., Broby Nielsen P., 2007, *MNRAS*, 379, 151
- Mackey A. D., Broby Nielsen P., Ferguson A. M. N., Richardson J. C., 2008, *ApJL*, 681, L17
- Mackey A. D., Gilmore G. F., 2003, *MNRAS*, 340, 175
- MacLean B. T., De Silva G. M., Lattanzio J., 2015, *MNRAS*, 446, 3556
- Marino A. et al., 2016, *MNRAS*, 459, 610
- Marino A. F. et al., 2012, *ApJ*, 746, 14
- Marino A. F., Przybilla N., Milone A. P., Da Costa G., D'Antona F., Dotter A., Dupree A., 2018, *AJ*, 156, 116
- Marino A. F., Villanova S., Piotto G., Milone A. P., Momany Y., Bedin L. R., Medling A. M., 2008, *A&A*, 490, 625
- Martell S. L., Smolinski J. P., Beers T. C., Grebel E. K., 2011, *A&A*, 534, A136
- Martocchia S. et al., 2017, *MNRAS*, 468, 3150
- Martocchia S. et al., 2018a, *MNRAS*, 473, 2688
- Martocchia S. et al., 2019, *MNRAS*, 487, 5324
- Martocchia S., Dalessandro E., Salaris M., Larsen S., Rejkuba M., 2020, *MNRAS*, 495, 4518
- Martocchia S. et al., 2018b, *MNRAS*, 477, 4696
- McConnachie A. W., 2012, *AJ*, 144, 4
- McLaughlin D. E., Harris W. E., Hanes D. A., 1994, *ApJ*, 422, 486

- McLaughlin D. E., van der Marel R. P., 2005, ApJS, 161, 304
- Mermilliod J.-C., 1995, The Database for Galactic Open Clusters (BDA), Egret D., Albrecht M. A., eds., Vol. 203, p. 127
- Messa M. et al., 2018, MNRAS, 477, 1683
- Mighell K. J., Sarajedini A., French R. S., 1998, AJ, 116, 2395
- Milone A., Bedin L., Piotto G., Anderson J., 2009, A&A, 497, 755
- Milone A. et al., 2012, A&A, 540, A16
- Milone A. P. et al., 2015, MNRAS, 450, 3750
- Milone A. P. et al., 2018, MNRAS, 477, 2640
- Milone A. P. et al., 2013, ApJ, 767, 120
- Milone A. P. et al., 2017, MNRAS, 464, 3636
- Miocchi P. et al., 2013, ApJ, 774, 151
- Monelli M. et al., 2013, MNRAS, 431, 2126
- Mucciarelli A., Carretta E., Origlia L., Ferraro F. R., 2008, AJ, 136, 375
- Mucciarelli A. et al., 2011, MNRAS, 413, 837
- Mucciarelli A., Dalessandro E., Ferraro F. R., Origlia L., Lanzoni B., 2014, ApJL, 793, L6
- Mucciarelli A., Ferraro F., Origlia L., Fusi Pecci F., 2007, AJ, 133, 2053
- Mucciarelli A., Origlia L., Ferraro F., Pancino E., 2009, ApJ, 695, L134
- Mucciarelli A., Origlia L., Ferraro F. R., Bellazzini M., Lanzoni B., 2012, ApJL, 746, L19
- Muratov A., Gnedin O., 2010, ApJ, 718, 1266

- Nardiello D. et al., 2018, MNRAS, 481, 3382
- Nardiello D. et al., 2015, MNRAS, 451, 312
- Neumayer N., Seth A., Boeker T., 2020, arXiv e-prints, arXiv:2001.03626
- Neumayer N., Walcher C. J., Andersen D., Sánchez S. F., Böker T., Rix H.-W., 2011, MNRAS, 413, 1875
- Niederhofer F. et al., 2017a, MNRAS, 465, 4159
- Niederhofer F. et al., 2017b, MNRAS, 464, 94
- Niederhofer F., Georgy C., Bastian N., Ekström S., 2015, MNRAS, 453, 2070
- Norris J., Cottrell P. L., Freeman K. C., Da Costa G. S., 1981, ApJ, 244, 205
- Pancino E., Rejkuba M., Zoccali M., Carrera R., 2010, A&A, 524, A44
- Parisi M. C., Geisler D., Clariá J. J., Villanova S., Marcionni N., Sarajedini A., Grocholski A. J., 2015, AJ, 149, 154
- Pasquini L. et al., 2002, The Messenger, 110, 1
- Peebles P. J. E., Dicke R. H., 1968, ApJ, 154, 891
- Pfeffer J., Kruijssen J. M. D., Crain R. A., Bastian N., 2018, MNRAS, 475, 4309
- Pietrinferni A., Cassisi S., Salaris M., Castelli F., 2004, ApJ, 612, 168
- Pietrinferni A., Cassisi S., Salaris M., Castelli F., 2006, ApJ, 642, 797
- Pietrzyński G. et al., 2019, Nat, 567, 200
- Piotto G. et al., 2007, ApJL, 661, L53
- Piotto G. et al., 2015, AJ, 149, 91
- Planck Collaboration et al., 2018, arXiv e-prints, arXiv:1807.06205
- Platais I. et al., 2012, ApJL, 751, L8

- Portegies Zwart S. F., McMillan S. L. W., Gieles M., 2010, ARA&A, 48, 431
- Prantzos N., Charbonnel C., Iliadis C., 2017, ArXiv e-prints, 1709.05819
- Renzini A. et al., 2015, MNRAS, 454, 4197
- Rich R. M., Shara M. M., Zurek D., 2001, AJ, 122, 842
- Rusakov V., Monelli M., Gallart C., Fritz T. K., Ruiz-Lara T., Bernard E. J., Cassisi S., 2020, arXiv e-prints, arXiv:2002.09714
- Salaris M., Pietrinferni A., Piersimoni A. M., Cassisi S., 2015, A&A, 583, A87
- Salaris M. et al., 2020, MNRAS, 492, 3459
- Salaris M., Weiss A., Cassarà L. P., Piovan L., Chiosi C., 2014, A&A, 565, A9
- Salaris M., Weiss A., Ferguson J. W., Fusilier D. J., 2006, ApJ, 645, 1131
- Salaris M., Weiss A., Percival S. M., 2004, A&A, 414, 163
- Salinas R., Strader J., 2015, ApJ, 809, 169
- Saracino S. et al., 2018, ApJ, 860, 95
- Saracino S. et al., 2020, arXiv e-prints, arXiv:2003.01780
- Sbordone L., Bonifacio P., Castelli F., Kurucz R. L., 2004, Memorie della Societa Astronomica Italiana Supplementi, 5, 93
- Sbordone L., Salaris M., Weiss A., Cassisi S., 2011, A&A, 534, A9
- Schiavon R. P., Caldwell N., Conroy C., Graves G. J., Strader J., MacArthur L. A., Courteau S., Harding P., 2013, ApJL, 776, L7
- Schiavon R. P. et al., 2017, MNRAS, 465, 501
- Sills A., Dalessandro E., Cadelano M., Alfaro-Cuello M., Kruijssen J. M. D., 2019, MNRAS, 490, L67
- Sills A., Karakas A., Lattanzio J., 2009, ApJ, 692, 1411

- Stanimirović S., Staveley-Smith L., Jones P. A., 2004, *ApJ*, 604, 176
- Stetson P. B., 1987, *PASP*, 99, 191
- Stetson P. B., 1994, *PASP*, 106, 250
- Strader J., Brodie J. P., Forbes D. A., Beasley M. A., Huchra J. P., 2003, *AJ*, 125, 1291
- Tian B., Deng L., Han Z., Zhang X. B., 2006, *A&A*, 455, 247
- Tremaine S. D., Ostriker J. P., Spitzer, L. J., 1975, *ApJ*, 196, 407
- Trenti M., Padoan P., Jimenez R., 2015, *ApJL*, 808, L35
- VandenBerg D. A., Brogaard K., Leaman R., Casagrande L., 2013, *ApJ*, 775, 134
- Vanzella E. et al., 2019, *MNRAS*, 483, 3618
- Vanzella E. et al., 2017, *MNRAS*, 467, 4304
- Villanova S., Geisler D., Carraro G., Moni Bidin C., Munoz C., 2013, *ApJ*, 778, 186
- Walcher C. J., Böker T., Charlot S., Ho L. C., Rix H. W., Rossa J., Shields J. C., van der Marel R. P., 2006, *ApJ*, 649, 692
- Walcher C. J. et al., 2005, *ApJ*, 618, 237
- Walker A. et al., 2011, *MNRAS*, 415, 643
- Wang M. Y. et al., 2019, *ApJL*, 875, L13
- Webbink R. F., 1985, in IAU Symposium, Vol. 113, Dynamics of Star Clusters, Goodman J., Hut P., eds., pp. 541–577
- Westerlund B. E., 1997, Cambridge Astrophysics Series, 29
- Whitmore B. C., Schweizer F., 1995, *AJ*, 109, 960
- Wijnen T. P. G., Pols O. R., Pelupessy F. I., Portegies Zwart S., 2016, *A&A*, 594, A30
- Wu X., Li C., de Grijs R., Deng L., 2016, *ApJL*, 826, L14
- Yong D., Grundahl F., Norris J., 2015, *MNRAS*, 446, 3319